5-1-2012

Parker Winds Revisited: An Extension to Disk Winds

Timothy Waters
University of Nevada, Las Vegas, waterst3@unlv.nevada.edu

PARKER WINDS REVISITED: AN EXTENSION TO DISK WINDS

by

Timothy R. Waters

Bachelor of Arts
Occidental College
May 2006

Master of Science in Applied Mathematics
University of Nevada Las Vegas
May 2009

A dissertation submitted in partial fulfillment of
the requirements for the

Master of Science in Physics

Department of Physics & Astronomy
College of Sciences
The Graduate College

University of Nevada, Las Vegas
May 2012

UNLV
UNIVERSITY OF NEVADA LAS VEGAS

THE GRADUATE COLLEGE

We recommend the thesis prepared under our supervision by

Timothy R. Waters

entitled

Parker Winds Revisited: An Extension to Disk Winds

be accepted in partial fulfillment of the requirements for the degree of

Master of Science in Physics
Department of Physics and Astronomy

Daniel Proga, Committee Chair

Bing Zhang, Committee Member

Stephen Lepp, Committee Member

Balakrishnan Naduvalath, Graduate College Representative

Ronald Smith, Ph. D., Vice President for Research and Graduate Studies
and Dean of the Graduate College

May 2012

ABSTRACT

Parker Winds Revisited: An Extension to Disk Winds

by

Timothy R. Waters

Dr. Daniel Proga, Examination Committe Chair
Associate Professor of Physics & Astronomy
University of Nevada, Las Vegas

A simple 1D dynamical model of thermally driven disk winds is proposed, based on the results of recent, 2.5D axi-symmetric simulations. Our formulation of the disk wind problem is in the spirit of the original Parker (1958) and Bondi (1952) problems, namely we assume an elementary flow configuration consisting of an outflow following pre-defined trajectories in the presence of a central gravitating point mass. Viscosity and heat conduction are neglected. We consider two different streamline geometries, both comprised of straight lines in the (x, z)-plane: (i) streamlines that converge to a geometric point located at $(x, z) = (0, -d)$ and (ii) streamlines that emerge at a constant inclination angle from the disk midplane (the x-axis, as we consider geometrically thin accretion discs). The former geometry is commonly used in kinematic models to compute synthetic spectra, while the latter, which exhibits self-similarity, is likely unused for this purpose, although it easily can be with existing kinematic models. We make the case that it should be, i.e. that geometry (ii) leads to transonic wind solutions with substantially different properties owing to its lack of streamline divergence. Pertinent to understanding our disk wind results, which are applicable to X-ray binaries, active galactic nuclei, and circumstellar discs, is a focused discussion on lesser known properties of Parker wind solutions. Parker winds are of wide applicability and have recently been used to predict photoevaporative mass loss rates from protoplanetary discs, but not without shortcomings, as we address. In addition, the

analytical solutions of Parker winds are ideal for assessing and validating the accuracy of hydrodynamical simulations. Geometry (i) contains the spherically symmetric Parker wind solution as a special case, while one instance of geometry (ii) has been used as a testbed problem for hydrodynamic simulations performed in cylindrical coordinates. We present a parameter survey of our analytical solutions to facilitate their usage for numerical testing purposes, and show that, for a subset of the parameter space, Keplerian rotation allows for two transonic wind solutions for the same set of parameters.

Acknowledgements

I sincerely thank my advisor Daniel Proga, from whom I took my first astrophysics course in the Fall of 2009. Without his guidance, support, and expertise, this thesis would not have been possible. Dr. Proga's mastery of astrophysics still astounds me, which made learning from him an exhilarating experience. My education was greatly aided by the three conferences that he sent to — my first ever conference in Boston, MA; my first international conference in Kraków, Poland; and a third conference in Charleston, SC.

I also thank my advisor and two other faculty members, Professor Bing Zhang and Associate Professor Ken Nagamine, for their exemplary efforts in creating a stimulating astronomy research environment at UNLV.

Last but certainly not least, I am indebted to the two women in my life — my mother Nancy and my wife Jiajia — for their relentless support and willingness to sacrifice over the past couple of years.

Funding support during the academic year in which this thesis was written was provided by the Nevada NASA Space Grant Consortium, through NASA grant NNX10-AJ82H. My advisor acknowledges support provided by the Chandra award TM0-11010X issued by the Chandra X-ray Observatory Center, which is operated by the Smithsonian Astrophysical Observatory for and on behalf of NASA under contract NAS 8-39073. He also acknowledges the UNLV sabbatical assistance and support from Program number HST-AR-12150.01-A that was provided by NASA through a grant from the Space Telescope Science Institute, which is operated by the Association of Universities for Research in Astronomy, Incorporated, under NASA contract NAS5-26555.

TABLE OF CONTENTS

LIST OF TABLES

LIST OF FIGURES

CHAPTER 1

INTRODUCTION

The classic Parker model has served as a paradigm wind solution for over half a century now. First developed for the Sun as a model of the solar wind, it shows the essential features of one-dimensional (1D), steady state wind models, namely that transonic solutions typically involve a transition through a critical point and have an X-type solution topology. The analytic solutions to both the original isothermal (with adiabatic index $\gamma = 1$) Parker wind (Parker, 1958) and its polytropic fluid ($1 < \gamma < 5/3$) extension (Parker, 1960) serve a dual purpose. On the one hand, they are beneficial for obtaining insight into the theory of outflows in general, as well as for gaining intuition into the subtleties that arise when solving wind equations analytically (for an in depth perspective see Königl & Salmeron 2011 and references therein). On the other hand, Parker wind solutions have proven useful for assessing the accuracy of numerical simulations (e.g., Keppens & Goedbloed 1999; Font et al. 2004; Stone & Proga 2009). To that end, one goal of this paper is to present a simplified dimensionless formulation of Parker winds and to provide formulae commonly used for numerical testing purposes. At the same time, we address certain aspects of the polytropic Parker problem that have been a source of confusion in the literature. Specifically, we clarify the properties of spherically symmetric Parker winds in the range $3/2 < \gamma < 5/3$ and the corresponding range of γ when angular momentum is added to the problem.

The primary focus of this paper is to present solutions to Parker-like winds emanating as a biconical flow, the geometry commonly used to model accretion disk winds. As we discuss in §3.2, Parker winds have been instrumental in uncovering other physical processes that can drive winds in stars, and led to the development of both line-driven (Castor et al. 1975, hereafter CAK) and magneto-centrifugally driven (beginning with the solution of Weber &

Davis 1967) wind theory. The current state of the art in stellar wind theory owes much of its development to the systematic assessment of how the inclusion of various physical terms and geometrical effects in the hydrodynamic equations alters the solutions of Parker winds. Studies of disk winds stand to benefit from rigorously repeating this procedure using counterpart, 1D analytical disk wind models.

Developing concrete baseline models analogous to Parker winds has proven to be a difficult task. A major roadblock has been the uncertainty in the streamline geometry, i.e. the actual trajectory traversed by material flowing out from the disk, as well as in the gravitational potential along these streamlines. Another obvious and related difficulty is posed by the fact that accretion disks span many more orders of magnitude in physical size than do stars, and they can host radically different, spatially and temporally variable, thermodynamic environments. Indeed, the outer radius of an accretion disk ranges from parsec scales for active galactic nuclei down (AGN) to within 1 AU for some circumstellar disks and the diverse physical conditions permit anything from infrequent outbursts to highly relativistic, steady jets. It should come as no surprise then, that despite clear observational evidence of outflows from many systems, identifying the actual driving mechanisms, as well as determining the wind geometry, remains a challenge.

Studies of disk winds therefore rely heavily on kinematic models in order to quickly explore the parameter space without assuming a particular driving mechanism. For example, kinematic models have been employed to produce synthetic spectra for cataclysmic variables (CVs), systems in which even key properties such as the geometry, ionization structure, and mass-loss rates remain difficult to constrain (e.g., Noebauer et al. 2010 and references therein). Early kinematic models assumed spherically symmetric outflows for simplicity (Drew & Verbunt 1985; Mauche & Raymond 1987). The consensus picture of a

Figure 1.1. Pictorial representation of the streamline geometry addressed in this paper. Neighboring streamlines diverge from each other in the (a) Parker and (b) Converging models, whereas in (c), the Constant Inclination Angle (CIA) model, there is no adjacent streamline divergence.

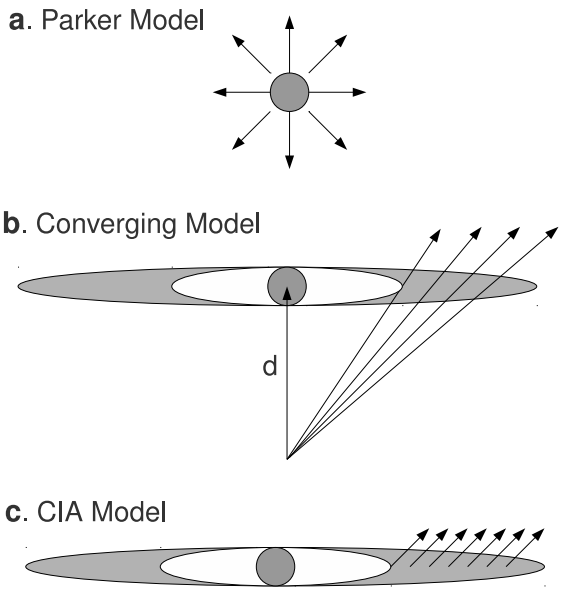

biconical mass outflow originating from the inner disk was born out of the observed characteristics of resonance lines in CVs (Córdova & Mason 1985, Drew 1987). This geometry was developed into a robust kinematic model by Shlosman & Vitello (1993), who calculated the ionization structure of CV disk winds and solved a radiative transfer problem in lines using the Sobolev approximation. Their kinematic model allowed for an arbitrary amount of streamline divergence.

Knigge et al. (1995) developed a different (Monte Carlo) code to solve the radiative transfer exactly. Their choice of wind geometry is one instance of what we refer to as the Converging model, in that the streamline divergence is just such that all streamlines converge to a geometric point located a distance d below the disk, as illustrated in Figure 1.1b. The Converging model, which has been called the "displaced-dipole" model by others, has been used in conjunction with sophisticated radiative transfer simulations to model accre-

tion disk spectra from massive young stellar objects (Sim et al. 2005), active galactic nuclei (Sim et al. 2008), CV disk winds (Noebauer et. al 2010), classical T Tauri stars (Kurosawa et al. 2011), and young intermediate-mass Herbig Ae stars (Grinin & Tambovtseva 2011). Typically, these simulations use Monte Carlo procedures that can account for nearly all of the prominent resonance lines and thereby accurately calculate the ionization balance of the wind. The Converging model has even been employed to calculate the neutron structure of neutrino-heated MHD disk winds associated with gamma-ray bursts (Metzger et al. 2008).

In this paper we develop a simple *dynamical* disk wind model that amounts to a generalization of the Parker model. Rather than positing a velocity law as is done for kinematic models, the purpose of a dynamical model is to impose the physical conditions and solve for the wind velocity as a function of distance along a streamline. This necessarily requires identifying a driving mechanism, i.e. a heating source in the case of thermally driven winds. Much of the groundwork theory for the source of heating was laid down by Begelman et al. (1983, hereafter BMS83), who showed that Compton-heated coronae are qualitatively the same for both quasars and X-ray binaries. This is because both galactic X-ray sources and the inner regions of AGN are expected to be heated via irradiation from a central X-ray source to high enough temperatures that thermal expansion alone gives rise to a disk wind.

As discussed by BMS83, very similar physics underlies photoionization heating, albeit the cooling mechanism is significantly more complicated (line-cooling and recombination vs. inverse Compton). A decade passed before it was realized that photoionization heating resolved a paradox involving the ultracompact HII regions observed around $\sim 10\%$ of O stars, as what were thought to be numerous, nearly static HII regions confined by some unknown source of back-pressure turned out be the continuous replenishment of hot ionized gas from the surface of photoevaporating protoplanetary disks (Hollenbach et al. 1993).

Subsequent studies revealed that the latter process is ubiquitous and can be a dominant disk dispersal mechanism (see the review by Armitage 2011). Adams et al. (2004) used isothermal Parker wind solutions to estimate the mass-loss rates from the edges of photoevaporating protoplanetary disks around low mass stars, and the relationships they derived were utilized recently by Gorti & Hollenbach (2009 hereafter GH09) to treat the hydrodynamics aspect of their coupled radiative transfer and hydrodynamic approach to modeling the global disk dispersal process for a range of stellar masses (we discuss this application further in §3.3 and §6.1).

Even though the underlying physics is very similar for Compton vs. photoionization heating, it might come as a surprise that the functional form for how the mass flux density scales with radius r_o along the disk plane is identical in both the works of BMS83 and Adams et al. (2004), especially given the fact that utilizing isothermal Parker winds in the context of Compton heating amounts to a significant simplification of the theory developed by BMS83. We can account for the agreement by contrasting the two approaches used to treat the thermodynamics. The simplicity of invoking Parker winds resides in the use of a polytrope ($P \propto \rho^{\gamma}$, where P is pressure and ρ is density), the conventional means for bypassing the heat equation when the source of heating is very complicated or poorly understood — not the case with Compton-heated coronae, in which the thermodynamics can be conveniently handled via an entropy equation. If it is assumed that no heat is transferred via conduction or viscous dissipation to or from outflowing gas, conservation of energy dictates that the entropy production is proportional to the heating rate, Γ. For optically thin gas heated to temperatures $T \gtrsim 10^6$ K, the net heating and cooling rate is proportional to the difference $T - T_{IC}$ (e.g., Krolik et al. 1981), where T_{IC} is the inverse

Compton temperature, defined by

$$kT_{IC} = \frac{1}{4} \langle h\nu \rangle \,. \tag{1.1}$$

Here, k is Boltzmann's constant and $\langle h\nu \rangle$ is the average photon energy from an isotropic radiation source of luminosity $\mathcal{L}$, namely

$$\langle h\nu \rangle = \frac{1}{\mathcal{L}} \int_0^\infty h\nu \mathcal{L}_\nu \, d\nu. \tag{1.2}$$

We therefore see that when the heating rate is high throughout the entire subsonic wind region, so that there is a near balance of heating and cooling, then an isothermal ($\gamma = 1$) Parker wind with $T = T_{IC}$ will be a good approximation to the strong gravity, nearly isothermal regime identified by BMS83 (see their solution regime E).

The scaling relationships for the mass flux density also agree in the opposite regime of adiabatic flow. A $\gamma = 5/3$ polytrope results when the entropy production is zero — when the flow is isentropic. In the framework of BMS83, this can effectively occur when the heat-transport can altogether be ignored ($\Gamma \approx 0$), meaning that the heating time-scales are long compared to the flow time-scales. More specifically, $\gamma = 5/3$ applies to gas with no internal degrees of freedom that is heated to a high temperature $T \lesssim T_{IC}$ in, say, a thin layer of the optically thick disk, that from there expands outward, loses additional pressure support upon being slowed by gravity, and thereby adiabatically cools. In §6.1, we explicitly show that the functional form of the mass flux density for a $\gamma = 5/3$ Parker wind is identical to the prediction given by BMS83 for their solution regime C.

Such agreement constitutes an encouraging basis for the present study, as the hydrodynamic formulation of BMS83 established that it suffices to estimate 2D global wind properties with a 1D model that captures the essential physics. Indeed, many predictions given by BMS83 were later confirmed by followup works that focused on the inherently two-

dimensional radiative transfer problem (e.g., Ostriker et al. 1991, Woods et al. 1996, Proga & Kallman 2002). Of special interest here is the work by Woods et al. (1996), who added to the basic theory of BMS83 based on the outcome of their time-dependent, 2.5D simulations of thermally driven winds from AGN heated by Compton as well as non-Compton processes such as photoionization and line-cooling. They provided an improved formula for the mass flux density as a function of disk radius and presented a detailed study of the flow topology and sonic surfaces for various spectral energy distributions.

Both the results of Woods et al. (1996) and those of the more recent 2.5D time-dependent simulations of a thermally driven wind carried out by Luketic et al. (2010, see Figure 1.2 here) indicate that the streamline geometry is rather simple, displaying two distinct flow patterns. Moreover, their results suggest that the Converging model may not be well-suited for sampling the entire wind, but rather only the inner portions of it. The outer portion is better approximated by a model in which streamlines emerge at a constant inclination angle to the midplane (hence the name, the CIA Model — see Figure 1.1c).[1] It is our intention to study how this difference in geometry affects the hydrodynamics independent of the explicit heating mechanism taking place; we merely assume that the boundary of the flow (the disk midplane) has been heated to a high enough temperature to drive a Parker-like disk wind.

This paper is organized as follows. In §2, we define and quantify the notion of rapid hydrodynamical escape and discuss the hydrodynamic foundations of wind theory. We then review the most common applications of Parker winds and summarize the background work on disk winds that this thesis builds upon. In §4, we present the streamline geometry used in this work and compare our choice to previous works in §4. Our formulation for solving both

[1]The kinematic model used by Shlosman & Vitello (1993) can accommodate CIA streamlines by setting $\theta_{min} = \theta_{max}$.

Figure 1.2. Flow streamlines that resulted from the time-dependent, hydrodynamical simulation of a thermally driven wind (Luketic et al. 2010). The z-axis is the rotation axis, while the x-axis is the disk midplane. Streamlines at $x \gtrsim 5R_{IC}$, where R_{IC} is the Compton radius, are self-similar. This figure gave motivation for the CIA model.

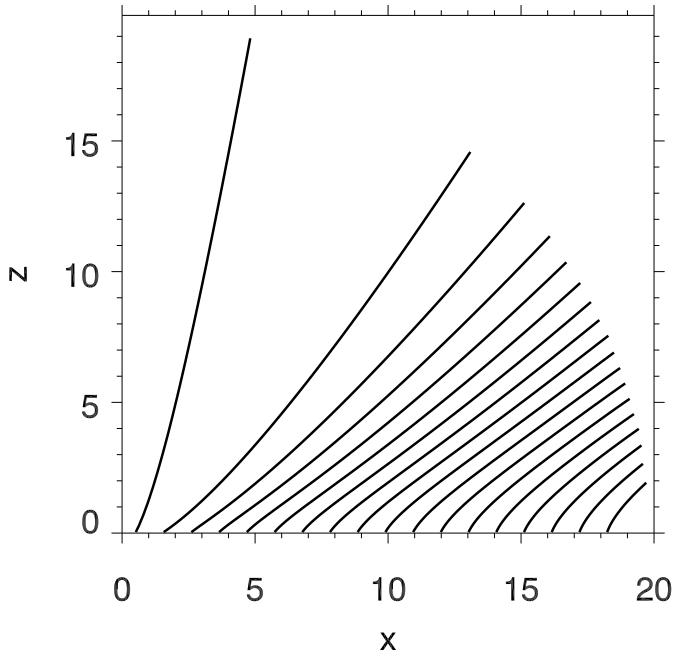

isothermal and polytropic thermally driven wind equations assuming an arbitrary amount of streamline divergence is given in §5. We adhere to the CAK approach of analyzing the momentum equation in terms of the singularity and regularity conditions. We also compactly solve the isothermal equations in terms of the Lambert W function. In §6, we present our results, beginning with an assessment and generalization of the scaling relationships derived by Adams et al. (2004). A parameter survey of our disk wind solutions for $1 < \gamma \leq 5/3$ is given in §6.2, where we also compare specific transonic wind solutions for the CIA and Converging models. In §7 we discuss subtle aspects of the classic Parker problem that are relevant to disk winds and reveal the effects of adding rotation. We conclude by summarizing our results and discussing the implications of our findings for kinematic models in §7.5.

CHAPTER 2

STATIC ATMOSPHERES VS. PARKER WINDS

Parker winds describe a highly idealized fluid phenomenon: the steady state, spherically symmetric, hydrodynamic escape of an ideal gas with zero viscosity. With these simplifications, and further supposing a fluid composed of only one species of gas, the Eulerian equations become analytically tractable. A complete isothermal Parker wind solution consists of the density ρ and velocity v as a function of radius r. Polytropic Parker wind solutions also include a temperature profile $T(r)$. The solution topology is almost the same as that of the classic Bondi problem. Namely, for every value of the mass loss rate less than some maximum rate, there are four solution branches, consisting of an everywhere subsonic velocity profile, an everywhere supersonic velocity profile, and two (unphysical) double-valued solutions for $v(r)$, one confined to radii within the sonic point r_c and one with $r > r_c$ everywhere. The maximum mass loss rate is obtained by the two transonic solutions, formed when any pair of the aforementioned solution branches continuously join at the sonic point. Of these two solutions, the transonic Parker wind solution is the one which is subsonic at small radii and supersonic at large radii. The family of isothermal ($\gamma = 1$) transonic Parker wind solutions depends solely on one parameter, which is often called the hydrodynamic energy parameter (HEP) and is defined as

$$\lambda_o = \frac{GM_* m_p \mu}{\gamma k T_o r_o}. \tag{2.1}$$

Here, G is the gravitational constant, M_* is the central body's mass, m_p the proton mass, μ is the mean molecular weight, and T_o is the temperature at the base of a streamline, i.e. at the boundary radius r_o. A polytropic equation of state (EoS) introduces a second dependence on the adiabatic index γ. The choice to incorporate γ into the HEP was not

made in the early papers on the solar wind, but it makes the dimensionless equations less cluttered.

It has not been emphasized in the literature that the Parker problem differs from the Bondi problem in one important respect that pertains to the boundary conditions. In the Bondi problem, the boundary is at infinity and as a consequence, the density boundary condition $\rho(r \to \infty) = \rho_\infty$ is automatically satisfied. On the contrary, the Parker problem has an inner boundary condition, which causes there to be *two sets* of critical point solutions to choose from for every value of the adiabatic index in the range $1 < \gamma < 5/3$ (except for $\gamma = 3/2$). More specifically, the equation governing the location of the sonic point has two roots and each one yields a family of solutions with the topology described above. Ultimately, therefore, there are two transonic Parker wind solutions to choose from; only one of them satisfies the density boundary condition $\rho(r \to r_o) = \rho_o$. This occurrence is accounted for mathematically in Appendix D.

Physically, Parker wind solutions model atmospheric coronae in hydro*dynamic* equilibrium just as a familiar barometric law, which yields the variation of density with radius, models an atmosphere in hydro*static* equilibrium. Indeed, an isothermal barometric law (albeit one that accounts for a varying gravitational potential) can be considered the trivial Parker wind solution with $v(r) = 0$, $T(r) = T_o = constant$, and

$$\rho(r) = \rho_o \exp\left[\lambda_o(r_o/r) - \lambda_o\right], \tag{2.2}$$

where ρ_o is taken to be the known density at a reference radius r_o. Equation (2.2) is most commonly recognized as the solution to the equation of hydrostatic equilibrium,

$$\frac{dP}{dr} = -\frac{GM_*\rho}{r^2} \tag{2.3}$$

for the special case of an ideal gas with a pressure $P = \rho k T_o / m_p \mu$. However, equation (2.2) is readily seen to be the density profile found by taking the limit of a Parker wind solution with a slowly expanding atmosphere ($v \to 0$) and a small mass-loss rate (corresponding to an everywhere subsonic solution—see §5.7 for more discussion). Recovering a static atmosphere from a slowly expanding one hints at a correspondence between thermal escape processes in kinetic theory and fluid dynamics.

2.1 Rapid Hydrodynamical Escape

Parker winds capture the simplest example of a more general thermal escape process characterized by hydrodynamical escape. We will use the term *rapid hydrodynamical escape* when we are explicitly referring to flows that are transonic. Modern, more realistic models can account for additional physical processes and non-spherical geometries, but the underlying hydrodynamic, thermal escape mechanism is effectively isolated by Parker winds.

The relevant thermal escape process in a static atmosphere is sometimes referred to as hydrostatic escape to distinguish (and emphasize) its relation to what we are calling hydrodynamic escape (e.g., Seager 2010). Hydrostatic escape is more commonly called evaporation or Jeans escape, which is the slow escape of particles in the high energy tail of a Maxwellian distribution, as described by kinetic theory. A parameter common to both the kinetic theory and fluid dynamics approaches to deriving a barometric law for a static (i.e. slowly evaporating) atmosphere is what we call the thermal energy parameter (TEP),

$$\tau \equiv \frac{|\Phi|}{c_s^2} = \lambda_o \frac{r_o/r}{T(r)/T_o}, \tag{2.4}$$

where $c_s = \sqrt{\gamma k T / \mu m_p}$ is the speed of sound. The TEP is by definition a measure of the thermal energy of gas at every location in a central gravitational field, and the second equality permits us to interpret the HEP as just the TEP evaluated at some reference level r_o, at which the temperature is $T_o \equiv T(r_o)$. The magnitude of the HEP at this level governs

which approach, fluid or kinetic, better models the escape process. As a concrete example, consider a planetary atmosphere having a Maxwellian temperature profile $T(r)$ and let r_o represent the radius of the exobase, beyond which particle collisions are negligible. Then $v_{th} = \sqrt{2kT_o/m_p\mu}$ is the most probable velocity of thermalized particles at the bottom of the exosphere. From equation (2.1), the HEP can be written as $\lambda_o = v_{esc}^2/v_{th}^2$, where $v_{esc} = \sqrt{2GM_*/r_o}$ is the escape velocity at the exobase. Evaporation is the dominant process when $v_{th} << v_{esc}$, i.e. when $\lambda_o >> 1$, so that only the highest energy particles can escape. If, for example, the atmosphere is both opaque to and subjected to a high flux of extreme ultraviolet (EUV) radiation, allowing $v_{th} \sim v_{esc}$ ($\lambda_o \sim 1$), then rapid hydrodynamical escape is expected to dominate. In that case, the overall escape process is more appropriately governed by the equations of hydrodynamics.

We should stress that rapid hydrodynamical escape implies a vanishing pressure at infinity (Parker 1958, 1960, 1965). In contrast, a static atmosphere can only be held static if there is a finite inward pressure exerted on it at large radii. In other words, the isothermal barometric law of equation (2.2) must break down at large radii because it tends to a finite pressure at infinity, irrespective of the presence of any outside medium that can balance this pressure.[2] The absence of this medium in essence provided the physical basis for Parker's original transonic solar wind solution, as the hydrostatic conduction model of Chapman (1957), the model of the extended solar corona that Parker's model superseded, implicitly featured a non-vanishing pressure at infinity. Parker pointed out that the vacuum-like conditions of the interstellar medium cannot possibly provide the necessary back pressure to keep the Sun's atmosphere in hydrostatic equilibrium.

[2]The density in equation (2.2) at $r = \infty$ is $\rho_o \exp(-\lambda_o)$ and for baratropic flow, the pressure is a function only of density. See Chamberlain (1963) for a detailed discussion of the breakdown of a barometric law using a kinetic theory approach.

More rigorously, we can exploit the TEP to identify a threshold temperature decline that determines whether or not an atmosphere can be held static. Integration of equation equation (2.3) over a non-isothermal atmosphere that extends from r_o (where $\rho = \rho_o$ and $T = T_o$) to some radius r can be written (c.f. Parker 1965),

$$\rho(r)T(r) = \rho_o T_o \exp\left[-\int_{r_o}^{r} \frac{\tau(r')}{r'}\, dr'\right], \tag{2.5}$$

where we have taken the pressure as $P(r) = c_s(r)^2\rho(r)$. In order for equation (2.5) to describe an atmosphere in hydrostatic equilibrium, the density must vanish at infinity, implying that the integral inside the exponent must be divergent at large r. Conversely, a Parker wind is the steady equilibrium state of an atmosphere if the integral is convergent. In terms of the TEP, ρ vanishes at infinity if τ is an increasing function of r, while the density tends to a finite value if $\tau(r)$ is decreasing. Physically, therefore, a static atmosphere is possible only if the gravitational potential energy of the gas outweighs its thermal energy at large radii. For the critical case in which these energies are in balance, i.e. when $\tau(r)$ is constant, we see from equation (2.4) that the temperature profile satisfies $T(r)/T_o = r_o/r$ and from equation (2.5) that the integral diverges logarithmically. Incidentally, a lively historical controversy concerning the transonic nature of the solar wind involved a competing hydrodynamical model due to Chamberlain (1961) with just this temperature dependence. Chamberlain's everywhere subsonic solution has been called the solar 'breeze'.[3] In §7.2, we show that there are no transonic Parker wind solutions with a $1/r$ temperature dependence, which occurs when $\gamma = 3/2$.

Importantly, $\gamma = 3/2$ is the critical adiabatic index that divides the solution space of transonic polytropic Parker winds and corresponds to the constant velocity solution

[3]Debate of its credibility persisted until 1962 when the Mariner 2 probe definitively established the existence of a continuous solar wind with an average supersonic solar wind speed of 500 km s^{-1} at Earth (Brandt 1970).

Table 2.1. Parameter Space of Spherically Symmetric Parker Wind Solutions:

Polytropic Index	Permitted HEP Range	TEP Behavior	Hydrostatic solutions?	Transonic solutions?
$\gamma = 1$	$[2, \infty]$	$d\tau/dr < 0$	No	Yes
$1 < \gamma < 3/2$	$[2, 1/(\gamma - 1)]$	$d\tau/dr < 0$	No	Yes
$\gamma = 3/2$	$\lambda_o = 2$	$d\tau/dr = 0$	No (Breeze)	No
$3/2 < \gamma < 5/3$	$[1/(\gamma - 1), 2]$	$d\tau/dr > 0$	Yes	Yes
$\gamma = 5/3$	$[1.5, 2]$	$d\tau/dr > 0$	Yes	No

$v(r) = c_o$, where $c_o = \sqrt{\gamma k T_o/\mu m_p}$ is the adiabatic sound speed at the base of the flow. For a given set of physical parameters it must be checked that there are viable solutions in the parameter space (λ_o, γ), which is coupled in a simple way. Namely, spherically symmetric transonic Parker wind solutions only exist when λ_o lies within the range $[2, 1/(\gamma - 1)]$ if $\gamma < 3/2$ and within $[1/(\gamma - 1), 2]$ if $\gamma > 3/2$. These HEP bounds are derived in §7.2. We relate this parameter space to the properties of the TEP in Table 1. Furthermore, in Table 1 we compare parameter regimes giving rise to valid hydrostatic solutions (which have $d\tau/dr > 0$ according to equation (2.5)) vs. transonic Parker wind solutions.

We mention here that the critical HEP bound analogous to $\lambda_o = 1/(\gamma - 1)$ for the parameter space of our transonic disk wind solutions (which assume Keplerian rotational velocities) is given by $\lambda_o = 2/(\gamma - 1)$. That this value is doubled for disk winds is a manifestation of the fact that the gravitational binding energy is halved for gas in a Keplerian disk. It should be noted that it is merely coincidental that in kinetic theory, the expression $2/(\gamma - 1)$ corresponds to the number of degrees of freedom n for a gas with polytropic index $\gamma = 1 + 2/n$ (see e.g., Chakrabarti 1990).

CHAPTER 3

APPLICATIONS OF PARKER WINDS

3.1 Planetary Winds

Despite their applicability to planetary studies, Parker winds were not immediately utilized to model planetary atmospheres. Hunten (1973) was among the first to directly address the thermal, non-evaporative loss of hot neutral gases from the terrestrial planets of our solar system, showing that the escape process is analogous to the transonic hydrodynamical escape of (ionized) solar wind particles. Gross (1974) adapted the Parker wind solution for a polytropic fluid to study the loss of hydrogen from Jupiter. When hydrogen is undergoing rapid hydrodynamical escape, it can drag heavier species of gas along with it; the term 'blowoff' has been used to denote the net outflow (e.g., Hunten 1982, 1990).

Achieving conditions to make rapid hydrodynamical escape more efficient than non-thermal escape processes for our solar system's planets requires a very high energy input from the Sun. The opacity to EUV radiation is too small to sufficiently heat the innermost planets, while the flux of radiation is too low to meet the energy input demands of the outer planets. Losses via non-thermal processes were eventually shown to dominate in the atmospheres of the terrestrial planets, the gas giants, and various satellites (e.g., Hunten 1982, 1990). While planetary Parker-like winds are probably only relevant for modeling the dense, primitive atmospheres of our solar system's planets, rapid hydrodynamical escape is believed to be efficient in the atmospheres of many close-in exoplanets.

For planetary applications, a major limitation of the polytropic EoS employed by Parker winds is that its use ultimately results in a temperature profile being assigned to the flow. Consequently, a specific spatial dependence is imposed on the energy input, one which need not even closely approximate the heating from *in situ* absorption throughout the

atmosphere. The usefulness of Parker winds to model the rapid hydrodynamical escape of gas from planets is therefore mainly qualitative. A more realistic time-independent solution for the rapid hydrodynamic escape problem was worked out by Watson et al. (1981). They developed a method that employs the hydrodynamic energy equation, which differs from a polytropic relation by a nonzero net volume heating rate. Compared to obtaining Parker wind solutions, obtaining transonic solutions with this method is a difficult numerical problem (Kasting & Pollack 1983, Tian et al. 2005). This method is better suited for studying *subsonic* hydrodynamic escape, as carried out by Kasting & Pollack (1983), due to the high sensitivity of the location of the critical (sonic) point to the boundary conditions.

Judging by the work done to explain the observations of the transiting 'hot-Jupiter' HD 209458b, it is clear that time-dependent simulation is the preferable tool for developing multi-dimensional models that move beyond a simple EoS (Tian et al. 2005, Munoz 2007, Murray-Clay et al. 2008, Stone & Proga 2009). Here again, Parker winds play a pivotal role. As we mentioned in the introduction, the analytic solutions to Parker winds are ideally suited for assessing the accuracy of the numerical schemes used in hydrodynamic simulations. For instance, Stone & Proga (2009) tested their methods by showing that their spherically symmetric computational models of escaping atmospheres from hot-Jupiters agreed with Parker wind solutions to better than 1%.

For reference, we provide a numerical value of λ_o appropriate for exoplanets (using parameters for Jupiter)

$$\lambda_o \simeq \frac{22\mu}{\gamma} \left(\frac{T_o}{10^4 K}\right)^{-1} \left(\frac{r_o}{R_J}\right)^{-1} \left(\frac{M_*}{M_J}\right). \tag{3.1}$$

We have assumed a relatively high effective temperature of $T = 10^4$ K for exoplanets, as might be met for hot-Jupiters subjected to intense, EUV radiation from its parent star (e.g., Yelle 2004). Notice, in particular, that for there to be transonic Parker wind solutions for

exoplanet applications (within the parameter space $[2, 1/(\gamma - 1)]$), γ must be very nearly 1 unless the gas is sufficiently ionized so that μ is reduced significantly below 1. Furthermore, for $3/2 < \gamma < 5/3$, the bound $1/(\gamma - 1) < \lambda_o < 2$ implies an exospheric temperature in the range $[11\mu/\gamma, 22\mu(\gamma - 1)/\gamma] \times 10^4$ K for Jovian parameters. The temperature ranges are reversed for $1 < \gamma < 3/2$.

3.2 Stellar Winds

Stellar wind theory has undergone many advances by way of making detailed observational and theoretical comparisons with Parker winds, as substantial departures from its predictions indicate that other forces or processes are at work. For example, simply scaling up the parameters of Parker winds cannot explain the observed mass-loss rates and terminal velocities of O stars, which ruled out thermal driving for these stars and eventually led to the highly successful theory of radiatively driven mass loss (CAK). As another example, the observations of Kraft (1967) showing that late type stars in young clusters have faster rotation rates than our sun led investigators to find other wind-launching mechanisms, as the mass-loss rate from Parker winds (even accounting for rotation) is insufficient to shed significant angular momentum over the sun's lifetime. Weber & Davis (1967) discovered the effect of magnetic braking and explained the slow rotation of the sun as due to the 'effective co-rotation' of the solar wind within the Alvén radius. In so doing, their analysis revealed the essential features of magneto-centrifugally driven wind models.

The solar wind, defined by Parker himself as "simply the outward extension of the quasi-static corona of the sun" (Ch. 1 of Jokipii et al. 1997), is observed to be a very dynamic phenomena governed by turbulent magnetohydrodynamics throughout (e.g., Biskamp 2003). The details of the actual heating processes leading to the formation of the corona constitute

the still debated 'coronal heating problem'. Despite the Sun's magnetic nature, if the dynamo process were to suddenly come to a halt, leaving only the residual heat, a Parker wind would persist until the heat had dissipated. Magnetic fields mainly divert or confine the flow, shaping the wind into a 'Parker spiral' on scales of ~ 1 AU, while creating both a fast wind and a slow wind (depending on whether the flow originates from regions with open or closed magnetic field lines) on similar scales.

The fact that magnetic fields are not the dominant influence over the solar wind beyond $\sim 10R_{\odot}$ provides theoretical support for the transonic nature of the solar wind (Brandt, 1970). In the coronal regions, the plasma beta (the ratio of thermal to magnetic pressure) is small and the magnetic field structure controls the wind dynamics, as it would at larger radii if the wind remained subsonic (e.g., Cravens 1997). The point being, the flow is driven primarily by thermal pressure gradients, so the solar wind is described by a Parker wind as a first approximation that can capture the essence of the dynamics and provide order of magnitude estimates of the wind velocity and mass-loss rate.

The solar wind occupies a radial distance of ~ 100 AU, while the sonic point is located within a few $R_{\odot}$, meaning that the heating takes place in a relatively tiny layer in the subsonic regions of the expanding corona. As a consequence, the temperature profiles resulting from the use of a polytropic EoS pose fewer limitations and actually have predictive power. For instance, Leer and Holzer (1979) exploited the temperature profile of a $\gamma = 1.1$ wind solution to place strong constraints on the coronal temperatures of our Sun in the subsonic flow regions, within the confines of the polytropic Parker model. Without any knowledge of solar wind properties at 1 AU, we can illustrate the constraints imposed by the Parker model just by considering the parameter space of valid transonic wind solutions.

The numerical value of λ_o appropriate for stars is

$$\lambda_o \simeq \frac{14}{\gamma}\left(\frac{\mu}{0.6}\right)\left(\frac{T_o}{10^6 K}\right)^{-1}\left(\frac{r_o}{R_\odot}\right)^{-1}\left(\frac{M_*}{M_\odot}\right). \tag{3.2}$$

For $1 < \gamma < 3/2$, the bound $2 < \lambda_o < 1/(\gamma - 1)$ implies a coronal temperature in the range $[14(\gamma - 1)/\gamma, 7/\gamma] \times 10^6$ K for solar parameters, so for $\gamma = 1.1$ the coronal temperature should lie in the range $1.4 - 6.4 \times 10^6$ K.

It has long been known, however, that any constant γ fails to reproduce both the measured solar wind flux at 1 AU and the correct solar wind parameters close to the sun (Weber & Davis 1967). The observations can be reconciled with multidimensional MHD models that allow for a radially varying polytropic index, $\gamma = \gamma(r)$ (Tsinganos 1996). State of the art, 3D MHD global solar wind models implement such a prescription (e.g., Roussev et al. 2003, Cohen et al. 2007; see Ofman 2010 for a recent review of solar wind modeling).

3.3 Disk Winds

Magneto-centrifugally driven winds are often invoked as candidate mechanisms for explaining outflows from accretion disks. In systems or regions of systems where magnetic forces might be dynamically unimportant, thermal driving is a likely contender (e.g., Proga 2007 & references therein). Just as Parker winds are useful for modeling outflows from any spherical astrophysical body thought to be hot enough to exhibit a non-explosive, thermal expansion of gas, the Parker-like disk winds addressed in this paper can be expected to approximate thermally driven winds from the coronae of accretion disks associated with AGN, CVs, X-ray binaries, and protoplanetary disks. Our models can also be applied to unmagnetized protostellar disks, as their disk winds are typically modeled assuming a bipolar outflow.

Due to the diversity of physical scales spanned by accretion disks, a preliminary step

is to identify a characteristic radius for invoking thermal driving, in order to calculate the HEP. First, it is worth emphasizing that the escape velocity for disks varies with distance r_o along the disk midplane, so the HEP must be considered a function of r_o. The distance r_o is therefore utilized to measure the height of the exobase for planets, the coronal radius for stars, and the distance to the 'footprint' of a given streamline for disks. In interpreting the parameter space of our solutions, it should be noted that there is an intrinsic difference between 1D disk wind models and 1D spherical wind models. Namely, the boundary of a spherically symmetric wind model spans no dimensions and is simply a point located at r_o, whereas the boundary of an infinitely thin disk, assuming axial symmetry, spans one dimension, viz. the x-axis—see Figure 4.1. Consequently, for a given mass M_* and characteristic launching radius r_o for a star or planet, varying the HEP samples different temperatures of the stellar corona or exosphere. Meanwhile, varying the HEP for a given central object mass for disk winds corresponds to altering either the temperature at a fixed distance along the midplane or the distance at a fixed temperature—or both.

As we mentioned in the introduction, isothermal Parker winds have already been utilized to study the dispersal of protoplanetary disks via photoevaporative winds, so it is worth discussing this application in more detail. The characteristic length scale for protoplanetary disks is 'the gravitational radius', $r_g = GM_*/c_o^2$, the distance where the gas becomes unbound because the escape velocity from the disk is equal to the thermal velocity of the gas (i.e. $\lambda_o \approx 1$). Early semi-analytic work concentrated on the radiative transfer problem of heating regions of protoplanetary disks beyond r_g; these studies established that photoevaporative heating creates physical conditions resembling HII regions, i.e. high energy (EUV) photons produce a hot and nearly isothermal ($T \sim 10^4$ K) ionized layer of hydrogen. The process can be subclassified as either internal or external photoevaporation (see Armitage

2011), depending on whether the ionizing source of radiation is primarily a central massive star (Shu et al. 1993, Hollenbach et al. 1994) or nearby massive stars (e.g., Johnstone et al. 1998), respectively. Since photoevaporation was considered to be significant at radii $r_o \gtrsim r_g$ in these early works, the gas was not subjected to any gravitational forces. The dominant disk dispersal mechanism in the inner disk region $r_o << r_g$, where the gravity of the central star cannot be neglected, is commonly referred to as viscous evolution and is believed to be a combination of dissipative and magnetic processes (leading to accretion onto the central star) and protostellar outflows (Hollenbach et al. 2000).

Subsequent studies indicated that photoevaporation can compete with viscous evolution to disperse the inner disk well within r_g. Isothermal Parker wind solutions played a central role in the work by Adams et al. (2004), who derived scaling relationships for the mass flux density of so-called 'subcritical' disks, those with outer disk radii $r_d << r_g$, based upon the functional dependence of the isothermal 'Keplerian' Parker wind solution (a radial Parker wind with a Keplerian azimuthal velocity component). Adams et al. (2004) took the outflow boundary to be a spherical surface subtending some solid angle $\delta\Omega$ at a radius r_o, i.e. they envisioned a flared disk and showed that an outflow emanating radially outward from the extended edge of the disk can dominate the 'vertical' wind from the disk surface. Using time-dependent hydrodynamic simulations, Font et al. (2004) confirmed that photoevaporation can lead to rapid hydrodynamical escape both within and beyond r_g, albeit for an un-flared disk. Our models therefore make it possible to move beyond a spherical wind boundary and analytically investigate Parker-like winds from the surface of the disk rather than from the disk edge.

The appropriate length scale used to calculate the HEP for AGN and X-ray binary disk winds is the Compton radius, the radius where the gravitational and thermal pressures are

equal:

$$R_{IC} \equiv \frac{GM_*}{c_{IC}^2} = \frac{GM_* m_p \mu}{kT_{IC}}. \tag{3.3}$$

Here, c_{IC} is the isothermal sound speed for gas heated to the inverse Compton temperature, which can be $\sim 10^8$ K depending on the spectrum of radiation. As discussed by BMS83, regardless of magnitude of the luminosity, at radii beyond R_{IC} the gas cannot remain quasi-static; the corona is itself unbound and better described as a vigorous wind region. Weak outflows are possible at smaller radii, down to $\xi \equiv r_o/R_{IC} \sim 0.1$ (Woods et al. 1996; see also Proga & Kallman 2002). In terms of ξ, the HEP is

$$\lambda_o = \frac{1}{\gamma \xi} \left(\frac{T_{IC}}{T_o(\xi)} \right). \tag{3.4}$$

Depending on the luminosity, the wind regions to either side are R_{IC} are further divided; BMS83 identified five solution regimes in all (see also Woods et al. 1996). Each has an associated mass flux density, determined by ξ and $\mathcal{L}/\mathcal{L}_{cr}$, where $\mathcal{L}_{cr}$ is a critical luminosity defined by

$$\mathcal{L}_{cr} = \frac{1}{8\mu} \left(\frac{c}{c_{IC}} \right) \left(\frac{m_e}{m_p} \right) \mathcal{L}_E. \tag{3.5}$$

Here, $\mathcal{L}_E$ is the Eddington luminosity, c the speed of light, and m_e the electron mass; $\mathcal{L}_{cr}/\mathcal{L}_E < 0.1$ for $T_{IC} \gtrsim 10^7$ K, so that thermal pressure dominates radiation pressure. Parker-like disk winds are most applicable in the regions affected by gravity, which includes the two weak wind regions with $\xi < 1$, labelled D and E by BMS83 with $\mathcal{L}/\mathcal{L}_{cr} < 1$ and $\mathcal{L}/\mathcal{L}_{cr} > 1$, respectively, as well as the 'gravity inhibited' strong wind region (labelled C) with $\xi > 1$ and $\mathcal{L}/\mathcal{L}_{cr} << 1$. The remaining two regions A & B have high enough luminosities that gravity is dynamically unimportant and adiabatic losses insignificant in the subsonic flow regime. The scaling relationships of isothermal Parker-like disk winds can capture the mass flux density to an order of magnitude in regions A & B, but the results

derived by Adams et al. (2004) apply to the isothermal region E.

We can now make an explicit comparison between equation (3.4) and the HEP for protoplanetary disks, which is simply

$$\lambda_o = \frac{r_g}{r_o}. \tag{3.6}$$

For a constant temperature on the disk midplane (appropriate for a disk surface heated by EUV radiation to $\sim 10^4$ K or Compton heated to $T_o(\xi) \sim 10^7$ K), r_g is constant, and we see that photoevaporative winds are qualitatively similar to Compton heated winds in the sense that r_g plays the role of R_{IC}. In either case, λ_o decreases as r_o^{-1} due to the reduced escape speed. However, a quantitative difference arises when r_g is constant because a vigorous wind region is expected to lie beyond r_g, where $\lambda_o < 1$. The parameter space for a Keplerian Parker wind only permits transonic solutions for $\lambda_o \gtrsim 10$, for at smaller HEP, the flow would no longer be launched subsonically. In other words, if the subcritical disks modeled by Adams et al. (2004) had a constant r_g, the bound $\lambda_o \gtrsim 10$ would necessarily lead one to predict the launching of initially *supersonic* flows at radii $r_o > r_g/10$. For Keplerian rotation more generally, the HEP parameter space of polytropic solutions is $(\lambda_o)_{min} < \lambda_o < 2/(\gamma - 1)$, where $(\lambda_o)_{min}$ is the model-dependent minimum HEP value that yields a transonic solution; for constant r_g, supersonic winds are expected at radii $r_o > r_g/(\lambda_o)_{min}$. Detailed hydrodynamic simulations indicate that flows within and beyond r_g are more likely to have subsonic initial velocities around $v_o = 0.4c_o$ (e.g., Font et al. 2004), although substantially higher launching velocities, even supersonic ones, are not unprecedented (see, e.g., Alexander et al. 2006). In general, therefore, the disk must be assigned a temperature profile $T_o = T_o(r_o)$, and with $r_g \propto T_o^{-1}$ not being constant, the parameter space of transonic solutions can be applied to a larger range of protoplanetary disk radii.

GH09 utilized the scaling relationships derived by Adams et al. (2004) to derive mass loss rates (and accompanying disk dispersal time-scales) along the entire protoplanetary disk surface. Using the thermo-chemical disk model presented in Gorti & Hollenbach (2008), they self-consistently calculated the decline of the gas temperature along the disk, which was subjected to EUV as well as far-ultraviolet (FUV) and X-ray irradiation. Upon applying Parker wind solutions to treat the hydrodynamics, they encountered temperatures corresponding to HEP values outside of the permitted parameter space for a Keplerian Parker wind. We can quantify this difficulty, as the bound $\lambda_o > (\lambda_o)_{min}$ translates into the following requirement on the temperature at the base of the flow:

$$T_o < \frac{5.4 \times 10^4 \text{ K}}{(\lambda_o)_{min}} \left(\frac{r_o}{1 \text{ AU}}\right)^{-1} \left(\frac{M_*}{M_\odot}\right) \left(\frac{\mu}{.5}\right). \tag{3.7}$$

GH09 quoted a gas temperature of $\sim$ 1000 K at 10 AU for a solar mass star. Since the Keplerian Parker wind solution has $(\lambda_o)_{min} \approx 10$, the temperature bound implies that transonic solutions only exist for $T_o < 540$ K at this radius. To circumvent this difficulty and calculate mass-loss rates for all radii intermediate to the radius where they assumed the flow is launched with $v_o = c_o$, GH09 extrapolated between the critical point equation of a Keplerian Parker wind and that of a spherically symmetric Parker wind, which has $(\lambda_o)_{min} = 2$ (and thus a less stringent temperature requirement). Ercolano et al. (2009) caution against the procedure of extracting 'global' mass loss rates from an admixture of 1D Parker wind solutions, advocating instead a coupled hydrodynamic and radiative transfer approach that entails finding sonic point distances according to a self-consistently determined streamline geometry. We share this sentiment, but it is certainly hopeful that a simplified hydrodynamics approach can provide adequate mass-loss rate estimates. We return to this topic in §6.1, where we show that GH09's specific extrapolation procedure leads to reasonable values of the magnitude of the initial Mach number, which is the relevant

quantity for incorporating the hydrodynamics.

GH09 point to a need for an alternative approach, suggesting the use of non-isothermal solutions such as those presented in the present work. Indeed, use of the CIA model, which has $(\lambda_o)_{min} \approx 2.5$ for all $1 < \gamma < 5/3$, would permit an extrapolation procedure to be avoided. To facilitate such an application of our disk wind models, in §6.1 we present polytropic scaling relationships for the mass-flux density, analogous to those derived for $\gamma = 1$ by Adams et al. (2004). We emphasize, however, that our solutions were developed for flows emerging from the midplane of geometrically thin disks. The photoevaporative flow surface of protoplanetary disks can extend to significant heights above the midplane. For example, GH09 find this surface to reside at a height of $\sim r_o/3$ above their fiducial disk. Since this height is within the scale height $H = \sqrt{2/\lambda_o} r_o$ of an isothermal corona when $\lambda_o < 18$, we expect our models to be approximately valid.

CHAPTER 4

STREAMLINE GEOMETRY

As discussed in BMS83, there are two routes to take in regards to specifying a geometry when finding solutions to wind equations: (i) assign some trajectory to the flow emanating from the disk or (ii) self-consistently solve for that trajectory. The first entails that an expression be provided for the flow tube area A that enters the steady state continuity equation $\rho v A = constant$. By adopting the geometry of the models discussed in the introduction, we necessarily take route (i). As shown in Figure 4.1, our geometry is comprised of streamlines that are straight lines in the (x, z)-plane. By rotating these straight streamlines around the z-axis, the actual trajectory traversed by the gas as it rises above the disk can be visualized; it spirals about a cone that widens according to the inclination angle i. Besides being observationally motivated, a biconical flow area is the simplest possible choice, for the distance along a streamline $l = l(x, z)$ can be used as the sole variable instead of seeking some relationship between the cylindrical coordinates x and z. Our coordinates are related by $x = r_o + l\cos i$, $z = l\sin i$, and $r = \sqrt{r_o^2 + l^2 + 2lr_o\cos i}$. CIA streamlines are self-similar, while Converging streamlines are not. We find $A(l)$ for each configuration in §5.1.

BMS83 and Fukue (1989) also took route (i) by assuming a flow configuration. Fukue (1989) adopted an area function similar to that used by BMS83, but he did not self-consistently implement the polytropic EoS when he followed BMS83 in requiring that the wind be launched from rest from the disk midplane. (No restriction is imposed on v_o for the entropy equation used by BMS83.) In our notation, BMS83 chose a generic area function aimed at parametrizing the streamline divergence: $A(l) = (1 + l/r_o)^q$. The parameter q is constrained to lie between 0 (vertical flow) and 2 (spherical flow). In §5.1, we show that the Parker and Converging models have $q = 2$, while the CIA model has $q = 1$.

Figure 4.1. The biconical outflow of our 'global' disk wind model is shown schematically on the left. On the right, we depict our coordinate system and the streamline geometry of the CIA and Converging models. In the fourth quadrant, we illustrate the geometry used to arrive at an expression for $A(l)$, which can be visualized as the area swept out around the z-axis by any two neighboring streamlines at a fixed distance l. This notion becomes exact in the differential limit of closely spaced streamlines.

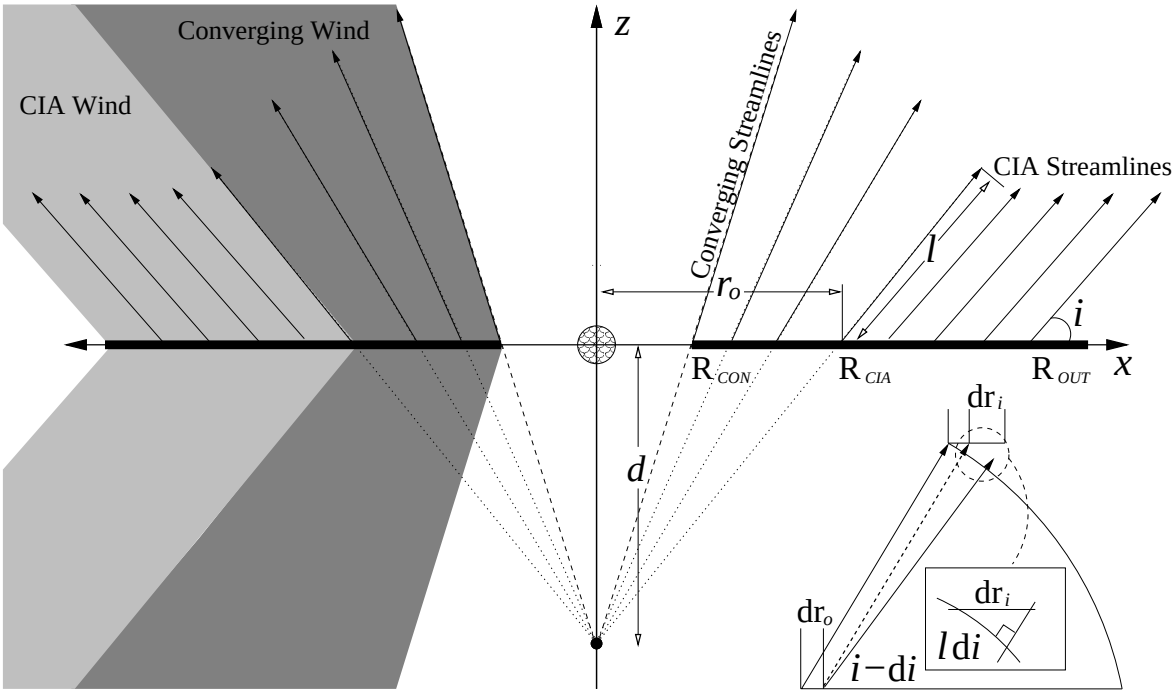

Alternatively, route (ii) can be followed, in which an attempt can be made to calculate $A(l)$ as part of the solution. This involves either solving the fully 2D, 2.5D, or 3D problem using numerical techniques or it requires making an extra assumption, such as self-similarity or force balancing. The latter route was taken by Takahara et al. (1989), who arrived at an expression for $A(l)$ by assuming that the centrifugal force balances the component of the gravitational force perpendicular to the flow velocity at every distance l along the streamline.[4] As discussed by BMS83, this is a valid approximation regardless of the streamline trajectory *close do the disk midplane* if angular momentum is conserved. It was soon pointed out by Fukue & Okada (1990) that Takahara et al. (1989) misrepresented the gravitational force in calculating this force balance.[5] The correct expression for $A(x, z)$, obtained by Fukue & Okada (1990), is significantly more complicated; it suffices to consider the shape of their streamlines in the (x, z)-plane. At every footprint distance r_o, the local streamline is found from

$$r = \frac{r_o + cz}{2} \left[1 + \sqrt{1 - \left(\frac{2z}{r_o + cz} \right)^2} \right], \tag{4.1}$$

where $r = \sqrt{x^2 + z^2}$ is the spherical position coordinate. The parameter c is an integration constant that resulted from the correct treatment of the force balance, which entailed solving an ordinary differential equation for dx/dz. Hence, c is related to the slope—the opening angle of the streamline—and defines a family of streamlines at every footprint radius r_o. See Figure 1 in Fukue & Okada (1990) for a plot comparing their streamlines for various values of c with the self-similar streamlines found by Takahara et al. (1989). By observing that the concavity or convexity of the streamlines in Figure 1.2 is pronounced only near the

[4] In the MHD literature, balancing forces perpendicular to the streamlines leads to the Grad-Shafranov (or transfield) equation.

[5] Takahara et al. (1989) used the x-component of the gravitational force rather than the component perpendicular to the streamline, to arrive at a self-similar streamline trajectory given by $z = x\sqrt{(x/r_o)^{2/3} - 1}$.

midplane, we can conclude that using equation (4.1) would not be an improvement over our choice of geometry, as equation (4.1) does not capture this feature.

Nevertheless, the findings of Fukue & Okada (1990) provide a physical argument supporting our choice of geometry. Examination of equation (4.1) reveals that close to the disk midplane, their streamline function is indeed just a straight line.[6] In other words, balancing the gravitational and centrifugal forces perpendicular to the flow *implies* straight streamlines close to the x-axis. Equivalently, conical streamlines define the path of minimum effective potential near the disk midplane. Moreover, Fukue & Okada showed that streamlines curve back on themselves (and intersect the z-axis) if $c < 2$. For streamlines to extend to infinity, it is required that $c \geq 2$. This is the requirement that the inclination angle $i \lesssim 27^\circ$ (see footnote 6), which is approximately the opening angle of the self-similar streamlines obtained by Luketic et al. (2010) and shown in Figure 1.2. Note, however, that the square root in equation (4.1) spoils the self-similarity that the streamlines would possess if the radical were zero.

One would expect that a model featuring streamline curvature in the (x, z)-plane would lead to significantly different wind solutions if the area function $A(l)$ directly determined the critical point location. This is not the case, however, as the well known rocket-nozzle analogy in stellar wind theory revealed that (the effective) gravity, more so than the flow tube area, plays the role of the converging-diverging nozzle to facilitate a transition from subsonic to supersonic flow (e.g., Lamers & Cassinelli 1999; we define the equivalent nozzle function in §6.1). To stress this point, consider how the area term enters the equation of motion per elimination of the density gradient (by taking a logarithmic derivative of the

[6] To see this, note that to first order in z, when $z << r_o$, $r \approx x$ and the right hand side of equation (4.1) is $\approx r_o + cz$. Hence, $x = r_o + cz$, which is just our x-coordinate, provided we identify the constant as $c = 1/\tan i$. Thus, $c \geq 2$ implies $i \leq \tan^{-1}(.5) = 26.57^\circ$.

continuity equation),

$$\frac{1}{\rho}\frac{d\rho}{dl} = -\frac{1}{v}\frac{dv}{dl} - \frac{1}{A}\frac{dA}{dl}. \tag{4.2}$$

The first term on the right hand side exemplifies the outcome of adopting a fluid treatment: the density gradient (and hence the pressure gradient for a polytropic EoS) itself depends on the flow acceleration. It is this term that gives rise to a singularity upon solving the equation of motion for dv/dl. In turn, the second term, $d\ln A/dl$, which is more a measure of streamline divergence than of the area between streamlines, influences the position of this singularity—the location of the critical point. This location would not change by much had we analytically modeled the exact area in Figure 1.2, as azimuthal streamline divergence is well accounted for using straight streamlines.

Despite the location of the critical point being reasonably well determined, our neglect of the initially vertical trajectories of the streamlines as well as any 'compression' of streamlines upon bending radially, features that are more prominent in the streamline plots of Woods et al. (1996) than in Figure 1.2, may have important ramifications for the behavior of the bulk flow velocity and Mach number profiles near the midplane. Namely, these features may contribute to making the profiles monotonic, so that the gas continually accelerates upon rising off the disk. As it is, gas on Keplerian orbits will, in the steady state, momentarily *decelerate* upon leaving the midplane for each of our geometries. In order for the flow to accelerate, it is required that $d\ln A/dl < 0$, which cannot be accomplished using straight streamlines (for they would have to intersect). This situation results from the balance between centrifugal and gravitational forces on the disk midplane, leaving only the area term $d\ln A/dl$ to determine whether or not the equivalent nozzle function is initially converging (if $q < 0$) or diverging (if $q > 0$), the latter implying that the bulk velocity and Mach number profiles will exhibit minima. The extent of the deceleration is sensitive to γ — we

plot representative disk wind solutions in §6.1, and in §7.3, we treat the rotating Parker problem to uncover just what rotation rates lead to a loss of monotonicity.

CHAPTER 5

HYDRODYNAMIC FORMULATION

In this section we present a general formalism for solving 1D thermally driven wind equations under either spherical or axial symmetry. We adopt all of the simplifications of the classic Bondi and Parker problems, namely we consider the hydrodynamic limit, assuming a single-fluid treatment and inviscid, barotropic flow. Imposing these restrictions allows the vector Eulerian momentum equation to be integrated and the problem solved using a simple Bernoulli function, constant along a given streamline. The forces acting on a fluid element are: the force of gravity from a central source, gas pressure, and the centrifugal force when there is nonzero rotation. We use the conventional polytropic EoS in lieu of the energy equation. We only relax the assumption of spherical symmetry by adding an azimuthal velocity component, conserving the specific angular momentum of the fluid, and we allow for arbitrary amounts of streamline divergence.

Our formulation is an extension of the classic isothermal and polytropic Parker problems into cylindrical symmetry. Because of the equivalence of wind and accretion equations, our problem is also a generalization of the classic Bondi problem (Bondi 1952). Bondi's analysis entailed applying boundary conditions at infinity, where both the velocity and gravitational potential vanish. Our solution allows boundary conditions to be applied at any finite distance away from the central gravitating object. Although we do not address the generalized Bondi problem because our focus is on winds, it should be kept in mind that any explicit reference to boundary conditions taken at 'the base' — be it the disk midplane or the surface of the central object — can equally well denote 'outer' boundary conditions appropriate to accretion problems.

5.1 The Continuity Equation

In Appendix C, we show that for the geometry of Figure 4.1, the steady-state continuity equation can be written as

$$d\dot{M} = \rho(l)v(l)A(l), \tag{5.1}$$

where $d\dot{M}$ is the differential mass-loss rate at the location r_o. The area between streamlines, $A(l)$, can be determined from equation (C.10), after specifying di/dr_o, the adjacent streamline divergence. The CIA model has no streamline divergence ($di/dr_o = 0$), giving

$$A(l) = 2\pi dr_o(r_o + l\cos i)\sin i. \tag{5.2}$$

We see by Figure 4.1 that the total midplane area occupied by the CIA model, obtained by letting $l = 0$, $\sin i = 1$, and integrating over dr_o from R_{CIA} to R_{OUT} is correctly given as $A_{CIA} = \pi(R_{OUT}^2 - R_{CIA}^2)$.

The Converging model, with geometry obeying $\tan i = d/r_o$, has streamline divergence $di/dr_o = -\cos i \sin i/r_o$, so

$$A(l) = \frac{2\pi dr_o(r_o + l\cos i)^2 \sin i}{r_o}. \tag{5.3}$$

Notice that for the same r_o, both the CIA and Converging models have a differential base area given by $A_o \equiv A(l = 0) = 2\pi r_o dr_o \sin i$. The total midplane area hosting a Converging wind is $A_{Con} = \pi(R_{CIA}^2 - R_{Con}^2)$.

The Parker Model from the Converging Model with $i = 0^\circ$

Only ratios of the area appear in the equations governing the flow, as in

$$\frac{1}{A(l)}\frac{dA(l)}{dl} = \left(\frac{q\cos i}{r_o + l\cos i}\right), \tag{5.4}$$

where $q = 1$ for the CIA model and $q = 2$ for the Converging model. The flow quenching factor $\sin i$ does not enter the disk wind problem except when calculating $\dot{M}$. We see,

therefore, that the Converging model contains the Parker model as a special case, for when $i = 0^\circ$, $d = 0$, bringing the converging point to the source of gravity. Then $r_o + l$ is just the spherical coordinate r, r_o representing the coronal radius rather than the footprint distance. The only distinction that needs to be made is that equation (5.3) formally does not apply in that case since $A(l) = 0$ — in cylindrical symmetry, there is no width between streamlines because they all overlap on the x-axis. This can be thought of as a collapse to spherical symmetry, so the Parker model results, albeit with the adjustment that the differential base area becomes $A_o = 2\pi r_o^2 \sin\theta d\theta$, where θ is the spherical polar coordinate, instead of $A_o = 2\pi r_o dr_o \sin i$.

Cylindrical Parker Winds: The CIA model with $i = 0^\circ$

Since the (rotating) Parker wind solution is recovered from the Converging model at $i = 0^\circ$, it is reasonable to ask if the solution to the CIA model at $i = 0^\circ$ bears any significance. It turns out that this solution was obtained by Skinner & Ostriker (2010) and included as a testbed problem in their extension of the MHD code *Athena* into cylindrical coordinates. This 'cylindrical version' of a rotating Parker wind, as they referred to it, can be viewed as a wind flowing perpendicular to the symmetry axis of evenly spaced concentric cylinders (with $A_o = 2\pi r_o dz$). Skinner & Ostriker's (2010) rotating wind test demonstrated cylindrical Athena's ability to maintain steady state, transonic flows and conserve angular momentum in cylindrical symmetry. Our solutions for both the Converging and CIA models with $i > 0^\circ$ open up the possibility of allowing this test to incorporate the z-dimension.

As we demonstrate, the proper procedure for wind equations is to take reference quantities at the footprint of a given streamline. The equations obtained for the CIA model at $i = 0^\circ$ by Skinner & Ostriker (2010) are seemingly the same as ours, yet the problem as they pose it is poorly formulated because they used reference quantities defined at infinity,

where the pressure (and hence sound speed for a polytropic EoS) vanishes. Specifically, they normalized the Bernoulli function to $c_\infty^2/(\gamma-1)$, which should equal 0. Their solutions do not suffer from this choice due to their assigning a value to the Bernoulli constant (thereby setting the location of the sonic point) a priori. These considerations reflect the notion that 'the boundary' where the Bernoulli function is evaluated should be located in the subsonic (causally connected) flow region and therefore can only lie at infinity for accretion problems or for everywhere subsonic flows.

5.2 The Bernoulli Function

By Bernoulli's theorem, the Bernoulli function is a constant on a streamline:

$$\frac{1}{2}v^2 + \Phi + h = constant, \tag{5.5}$$

for enthalpy $h = \int dP/\rho$ and bulk flow velocity $v = \sqrt{v_x^2 + v_\phi^2 + v_z^2} = \sqrt{v(l)^2 + v_\phi^2}$. We denote the Bernoulli constant as B_o and emphasize that, while it is to be evaluated at the boundary,

$$B_o \equiv \left(\frac{1}{2}v^2 + \Phi + h\right)\Big|_{BDY}, \tag{5.6}$$

it is a priori unknown because $v(l=0)$ is unknown.

To define B_o, both the temperature T and density ρ at the base of every streamline must be specified. We take these quantities to be T_o and ρ_o, respectively. For an ideal gas EoS, this is equivalent to specifying the pressure at at every footprint location r_o. The baratropic assumption, $dP = (\partial P/\partial\rho)d\rho$, is satisfied by an ideal gas EoS combined with the polytropic fluid relation, $T = T_o(\rho/\rho_o)^{\gamma-1}$. Explicitly we have $P = \rho_o k T_o(\rho/\rho_o)^\gamma/\mu m_p$, which gives

$$h = \int \frac{1}{\rho}\frac{dP}{d\rho}d\rho = \frac{c_o^2}{\rho_0^{\gamma-1}}\int \rho^{\gamma-2}\,d\rho = \begin{cases} c_s^2\ln(\rho/\rho_c) & \text{if } \gamma = 1 \\ c_s^2/(\gamma-1) & \text{if } \gamma > 1, \end{cases} \tag{5.7}$$

provided that we absorb into B_o the constant term $c_s^2 \ln(\rho_c)$ for $\gamma = 1$, as well as the constants of integration.

For rotational motion in a plane under a central force, the specific angular momentum L is a constant of the motion: $L = x v_\phi$, where $x = r_o + l\cos i$. We will present our disk wind results for a disk rotating at Keplerian velocities, in which the disk angular velocity at any location r_o is $\Omega_K = \sqrt{GM_* r_o}/r_o^2$. However, for treating Parker winds we follow Keppens & Goedbloed (1999) in allowing for arbitrary rotation rates Ω, parametrizing v_ϕ on the equatorial plane by some factor ζ of the adiabatic sound speed at the base, i.e. $v_\phi(l=0) = \Omega r_o = \zeta c_o$, giving

$$v_\phi = \Omega r_o \left(\frac{r_o}{x}\right) = \zeta c_o \left(\frac{r_o}{r_o + l\cos i}\right). \tag{5.8}$$

Keplerian rotation corresponds to $\zeta = \sqrt{GM_*/r_o c_o^2} = \sqrt{\lambda_o}$. Rotation therefore enters the problem as an effective potential,

$$\begin{aligned} \Phi \rightarrow \Phi_{eff} &= -\frac{GM_*}{r} + \frac{v_\phi^2}{2} \\ &= -\frac{GM_*}{\sqrt{r_o^2 + l^2 + 2lr_o\cos i}} + \frac{\zeta^2 c_o^2}{2}\left(\frac{r_o}{r_o + l\cos i}\right)^2. \end{aligned} \tag{5.9}$$

For $\gamma > 1$ then, the Bernoulli function reads

$$B_o = \frac{1}{2}v(l)^2 + \Phi_{eff}(l) + \frac{c_s(l)^2}{\gamma - 1}. \tag{5.10}$$

We treat the isothermal ($\gamma = 1$) case in §5.7.

5.3 The Equation of Motion

The equation of motion, which we will sometimes refer to as $F(l, v, dv/dl) = 0$, contains the velocity gradient. Critical points arise whenever the velocity gradient becomes undefined, i.e. when $dv/dl = 0/0$. Hence, the Bernoulli function must be accompanied

by $F(l, v, dv/dl) = 0$ to seek out these critical points. $F(l, v, dv/dl) = 0$ is found by first differentiating equation (5.10) to give

$$\frac{dB_o}{dl} = v\frac{dv}{dl} + \frac{d\Phi_{eff}}{dl} + \frac{c_s^2}{\rho}\frac{d\rho}{dl} = 0, \tag{5.11}$$

and then by eliminating the density gradient using the continuity equation. The relevant derivative is given in equation (4.2). Further dividing by c_s^2 gives

$$F(l, v, dv/dl) \equiv \left(1 - \frac{c_s^2}{v^2}\right)\frac{v}{c_s^2}\frac{dv}{dl} + \frac{1}{c_s^2}\frac{d\Phi_{eff}}{dl} - \frac{1}{A}\frac{dA}{dl} = 0. \tag{5.12}$$

5.4 Dimensionless Formulation

Our disk wind problem depends on a total of three parameters, namely, λ_o, γ, and i. We find it natural to normalize distances to the gravitational radius,

$$r_g = \lambda_o r_o = \frac{GM_*}{c_o^2}. \tag{5.13}$$

Justification for this choice is obtained by shifting one's viewpoint to consider all subscripts 'o' as standing for 'outer' rather than midplane boundary conditions. Then in the limit $c_o \to c_\infty$, r_g is the so-called Bondi length. Since we will discuss results for both spherical winds and disk winds, we will differentiate disk wind bulk velocities by normalizing to $V_{esc} = \sqrt{GM_*/r_o}$, the escape velocity from a thin Keplerian disk at a distance r_o along the disk, instead of $v_{esc} = \sqrt{2}V_{esc}$. Recall that the HEP has several different guises in terms of these characteristic quantities, namely

$$\lambda_o = \frac{V_{esc}^2}{c_o^2} = \frac{v_{esc}^2}{2c_o^2} = \frac{r_g}{r_o}. \tag{5.14}$$

Unknown Critical Point Quantities

We introduce a quantity analogous to λ_o, defined by

$$\lambda_c \equiv \frac{V_{esc}^2}{c_s(l_c)^2}, \tag{5.15}$$

where $c_s(l_c)$ is the sound speed at the critical point. Since $c_s(l_c)$ is in a one-to-one relationship with the critical point distance l_c, λ_c is a central unknown. In general, λ_c can only be solved for numerically. Many quantities of interest such as the mass loss rate, the initial velocity, and the terminal velocity can be simply expressed in terms of the ratio $\lambda_c/\lambda_o = T_o/T_c$, where T_c is the temperature at the critical point. Note that $\lambda_c = \lambda_o$ in the isothermal case. For $1 < \gamma < 5/3$, the ratio λ_c/λ_o is equal (by construction) to the fundamental constants of the problem,

$$\frac{\lambda_o}{\lambda_c} = \frac{(B_o/c_o^2)}{e_c}, \tag{5.16}$$

where $e_c = e_c(\lambda_c, \chi_c)$ is the critical point constant, defined as

$$e_c = \left.\frac{B_o}{c_s^2}\right|_{\chi=\chi_c}. \tag{5.17}$$

Evaluated at the critical point (see §5.5), e_c is a constant independent of B_o, which is evaluated at the boundary. Therefore, e_c and B_o together determine $c_s(\chi_c)^2 = B_o/e_c$ as well as λ_c. It will be seen in fact that equation (5.16) combined with the singularity condition (discussed in §5.5) determines the location of the critical point (see §5.5).

Dimensionless Equations

We now rewrite the governing equations into a form suitable for numerical implementation. We begin by introducing the following dimensionless variables:

$$\begin{aligned}
\text{distance along a streamline:} \quad \chi &= \frac{l}{r_g}, \\
\text{specific kinetic energy:} \quad y &= \frac{1}{2}\frac{v^2}{c_s(\chi_c)^2}, \\
\text{Mach number:} \quad \mathcal{M} &= \frac{v}{c_s}, \\
\text{Mach number squared:} \quad w &= \mathcal{M}^2, \\
\text{sound speed squared:} \quad s &= \frac{c_s^2}{c_s(\chi_c)^2}.
\end{aligned}$$

Here, $\chi_c = l_c/r_g$ is the dimensionless critical point distance. The variables y, w, and s are related by

$$y = \frac{sw}{2}. \tag{5.18}$$

We prefer simply keep ρ/ρ_o and A/A_o instead of renaming the density and flow tube area. Then the continuity equation becomes

$$\frac{\dot{m}}{\rho_o c_s(\chi_c)} = \sqrt{2y}\frac{\mathrm{A}}{\mathrm{A}_o}\frac{\rho}{\rho_o}, \tag{5.19}$$

where the mass flux density, $\dot{m}$, is defined as

$$\dot{m} \equiv \frac{d\dot{M}}{A_o}. \tag{5.20}$$

Note that $\dot{m} = \rho_o v_o = \rho_o c_o \mathcal{M}_o$, where $\mathcal{M}_o$ is the initial Mach number. The polytropic relation is now

$$s = s_o \left(\frac{\rho}{\rho_o}\right)^{\gamma-1} = \frac{\lambda_c}{\lambda_o}\left(\frac{\rho}{\rho_o}\right)^{\gamma-1}, \tag{5.21}$$

where by construction $s_o \equiv s(\chi = 0) = \lambda_c/\lambda_o$.

Dividing equation (5.10) by the unknown quantity $c_s(\chi_c)^2$ gives the dimensionless Bernoulli function,

$$e_c = y + \frac{\lambda_c}{\lambda_o}U_{eff} + \frac{1}{\gamma-1}s, \tag{5.22}$$

where

$$\begin{aligned} U_{eff} &= U + U_{centrif} \\ &= -\frac{1}{\sqrt{\chi^2 + 2\chi f\cos i + f^2}} + \frac{1}{2}\left(\frac{\zeta f}{f + \chi\cos i}\right)^2, \end{aligned} \tag{5.23}$$

and we have introduced the following quantities:

$$\text{gravitational potential:} \quad U = \frac{\Phi}{c_o^2}, \tag{5.24}$$

$$\text{centrifugal potential:} \quad U_{centrif} = \frac{v_\phi^2}{c_o^2}, \tag{5.25}$$

$$\text{inverse HEP:} \quad f = \frac{1}{\lambda_o}. \tag{5.26}$$

The above equations take their simplest form by eliminating any reference to ρ_o and A_o. Expressed this way, the equations depend only on the ratio λ_c/λ_o and values taken at the critical point, making it clear that the accretion equations (with outer boundary condition $\lambda_o \to 0$ at $A_o \to \infty$ but with finite λ_c/λ_o and A_c) are identical to the wind equations. First we square equation (5.19) and express it in terms of w: $\dot{m}^2 = sw(\rho_o c_o)^2(\lambda_c/\lambda_o)(\mathrm{A}/\mathrm{A}_o)^2(\rho/\rho_o)^2$. The polytropic EoS, equation (5.21), permits substitution for ρ/ρ_o. Further evaluating $\dot{m}^2$ at the critical point where $s_c = w_c = 1$ yields the combined continuity equation/polytropic EoS in terms of $\dot{m}_c^2$,

$$\dot{m}^2 = \dot{m}_c^2 \frac{\mathrm{A}^2}{\mathrm{A}_c^2} w s^{\frac{\gamma+1}{\gamma-1}}. \tag{5.27}$$

Defining

$$\Lambda \equiv \frac{\dot{m}}{\dot{m}_c}, \tag{5.28}$$

equation (5.27) becomes

$$\Lambda^2 = \frac{\mathrm{A}^2}{\mathrm{A}_c^2} w s^{\frac{\gamma+1}{\gamma-1}}. \tag{5.29}$$

Rewriting the dimensionless Bernoulli function written in terms of s and w gives

$$e_c = \frac{sw}{2} + \frac{\lambda_c}{\lambda_o} U_{eff} + \frac{1}{\gamma - 1} s, \tag{5.30}$$

and equations (5.29) and (5.30) together comprise an algebraic system of two equations for the two unknowns s and w. Once e_c is evaluated, an explicit solution for w can be found.

The equation of motion, equation (5.12), becomes

$$F \equiv \left(1 - \frac{s}{2y}\right) \frac{1}{s} \frac{dy}{d\chi} + \frac{1}{s} \frac{\lambda_c}{\lambda_o} \frac{dU_{eff}}{d\chi} - \frac{1}{\mathrm{A}} \frac{d\mathrm{A}}{d\chi} = 0. \tag{5.31}$$

This can be further simplified by letting $y' = dy/d\chi$, $\mathrm{A}' = d\mathrm{A}/d\chi$, and by defining the (minus of the) effective gravitational force as

$$g = \frac{dU_{eff}}{d\chi} = \frac{\chi + f\cos i}{(\chi^2 + 2\chi f \cos i + f^2)^{\frac{3}{2}}} - \frac{(\zeta f)^2 \cos i}{(f + \chi \cos i)^3}. \tag{5.32}$$

$F(\chi, y, y') = 0$ now reads

$$F \equiv (1 - \frac{s}{2y})\frac{y'}{s} + \frac{g}{s}\frac{\lambda_c}{\lambda_o} - \frac{\mathrm{A}'}{\mathrm{A}} = 0. \tag{5.33}$$

5.5 Critical Point Conditions

The Critical Point Constant

The value of the critical point constant e_c is found from equation (5.30) evaluated at the critical point,

$$e_c \equiv \frac{sw}{2} + \frac{\lambda_c}{\lambda_o}U_{eff} + \frac{1}{\gamma - 1}s\Bigg|_{\chi=\chi_c}. \tag{5.34}$$

Again since $s_c = w_c = 1$, we have that

$$e_c = \frac{1}{2}\left(\frac{\gamma + 1}{\gamma - 1}\right) + \frac{\lambda_c}{\lambda_o}U_{eff}(\chi_c). \tag{5.35}$$

In general, therefore, e_c depends on the critical point distance χ_c. It is easily seen that despite the fact that the classic Bondi and Parker problems can have very different Bernoulli constants B_o, they both have the same value of $e_c = B_o/c_s(\chi_c)^2$. The singular nature of their equations at the critical point are identical. In that spherically symmetric case, e_c is independent of χ_c and λ_c:

$$e_c = \frac{1}{2}\left(\frac{5 - 3\gamma}{\gamma - 1}\right) \text{ (for spherical symmetry only).} \tag{5.36}$$

Rotation breaks this equivalence because then $e_c = e_c(\chi_c)$, and χ_c depends on the boundary conditions.

The Singularity and Regularity Conditions

The singularity condition identifies all points at which the flow acceleration is undefined, i.e. all values of χ for which $F(\chi, y, y') = 0$ is independent of y':

$$\frac{\partial F}{\partial y'} = 0. \tag{5.37}$$

From equation (5.33), the set of possible points picked out by equation (5.37) are those that satisfy $y = s/2$ (or in physical units, $v = c_s$) at χ_c. The regularity condition, in turn, defines the acceleration at this point as the slope of F in the (χ, y)-plane: $y' = -(\partial F/\partial\chi)/(\partial F/\partial y)$, or as it is more commonly stated,

$$\frac{\partial F}{\partial \chi} + y' \frac{\partial F}{\partial y} = 0. \tag{5.38}$$

Equation 5.38 is formally derived by ensuring that $dF(\chi, y, y')/d\chi = 0$ all along the solution curve, which is equivalent to requiring a finite jerk, i.e. that y'' is bounded at χ_c (Lamers & Cassinelli 1999, §8.7). The role of the regularity condition is to ensure the continuity of the solution at the critical point. Since this point coincides with the sonic point for our problem, it marks the region where the flow loses communication with what is happening downstream. In the neighborhood of this point then, there could potentially be thermodynamically different situations, which would result in a shock— a discontinuity in y'. Physically, therefore, the regularity condition prevents shocks, i.e. it demands that nothing special happens with the flow at the critical point. For more complicated equations of motion, e.g. with line-driving included, explicit use of the regularity condition is required to determine the location of the critical point (CAK). For thermally driven winds, it is not needed, but we will make use of it in §7.3 to interpret the negative root of the isothermal critical point equation.

The Relation Between λ_c and χ_c

The singularity condition combined with the equation of motion yields a relationship between χ_c and λ_c; it does not directly determine the location of χ_c (except for the isothermal case when $\lambda_c = \lambda_o$). With $y = s/2$ at the critical point, equation (5.33) gives,

$$\frac{\lambda_o}{\lambda_c} = g_c \frac{\mathrm{A}_c}{\mathrm{A}'_c}. \tag{5.39}$$

Here, $g_c = g(\chi_c)$ and $\mathrm{A}_c/\mathrm{A}'_c = (f + \chi_c \cos i)^q/(q \cos i)$, where $q = 1$ for the CIA model and $q = 2$ for the Parker ($i = 0^\circ$) and Converging models.

The Location of the Critical Point(s)

It was mentioned in §5.4 that the innocuous looking equation $e_c = (\lambda_c/\lambda_o)B_o/c_o^2$ combined with equation (5.39) determines the location of the critical point. Equivalently, we can evaluate equation (5.30) at the lower boundary,

$$e_c = \frac{\lambda_c}{\lambda_o}\left[\frac{w_o}{2} + U_{eff,o} + \frac{1}{\gamma - 1}\right], \tag{5.40}$$

where, using the definitions of y and s, we have factored out $s_o = \lambda_c/\lambda_o$. A relation between w_o and λ_c follows from equation (5.29):

$$w_o = \left(\Lambda \frac{\mathrm{A}_c}{\mathrm{A}_o}\right)^2 \left(\frac{\lambda_o}{\lambda_c}\right)^{\frac{\gamma+1}{\gamma-1}} \tag{5.41}$$

With equations (5.41) and (5.35) both substituted into equation (5.40), and noting that $U_{eff,o} = -\lambda_o + \zeta^2/2$, the general equation that must be satisfied by a critical point is

$$\begin{aligned} &\frac{\lambda_o}{\lambda_c}\left[\frac{1}{2}\left(\frac{\gamma+1}{\gamma-1}\right) + \frac{\lambda_c}{\lambda_o}U_{eff}(\chi_c)\right] = \\ &\left[\frac{1}{2}\left(\Lambda\frac{\mathrm{A}_c}{\mathrm{A}_o}\right)^2\left(\frac{\lambda_o}{\lambda_c}\right)^{\frac{\gamma+1}{\gamma-1}} - \lambda_o + \frac{\zeta^2}{2} + \frac{1}{\gamma-1}\right]. \end{aligned} \tag{5.42}$$

All appearances of λ_o/λ_c in equation (5.42) are to be eliminated using equation (5.39). The resulting equation can only be solved numerically—with a root finder capable of detecting multiple roots—except for the classic Bondi problem. The roots of equation (5.42) are all X-type critical points, in contrast with the isothermal critical point equation, equation (5.39), which can have roots that topologically resemble 'O-type' critical points but correspond to the location of velocity minimums.

We solved equation (5.42) for all of its roots using simple bracketing and bisection with a tolerance of 10^{-8} (Press et al. 1992). Once a numeric value for $\chi_c \equiv l_c/r_g$ is determined,

the location of the critical point in units of r_o is

$$\frac{l_c}{r_o} = \lambda_o \chi_c. \tag{5.43}$$

In Appendix D, we explain why equation (5.42) must always possess an X-type root yielding a transonic wind solution that does not satisfy the boundary condition $\rho(\chi = 0) = \rho_o$. These are not acceptable critical point solutions, although they can easily be mistaken as such because the resulting transonic Mach number profiles appear identical.

5.6 The Polytropic Fluid Solution

Rearranging equation (5.30) to isolate s gives

$$\left(\frac{w^{-1}}{\gamma - 1} + \frac{1}{2}\right) sw = e_c - \frac{\lambda_c}{\lambda_o} U_{eff}. \tag{5.44}$$

An explicit solution to the problem, i.e. a solution comprised of separated functions of the dependent and independent variables, follows from substituting equation (5.29) solved for s into equation (5.44) and multiplying both sides by $(\Lambda\, \mathrm{A}_c/\mathrm{A})^{-2\frac{\gamma-1}{\gamma+1}}$:

$$F(w) = \Lambda^{-2\frac{\gamma-1}{\gamma+1}} X(\chi), \tag{5.45}$$

where

$$F = \left(\frac{w^{-1}}{\gamma - 1} + \frac{1}{2}\right) w^{\frac{2}{\gamma+1}},$$
$$X = \left(\frac{\mathrm{A}}{\mathrm{A}_c}\right)^{2\frac{\gamma-1}{\gamma+1}} \left(e_c - \frac{\lambda_c}{\lambda_o} U_{eff}\right).$$

Note that an explicit solution cannot be found in terms of the kinetic energy ($y = sw/2$), as ridding the left hand side of equation (5.44) of χ-dependence to give $F = F(y)$ is not possible. Also note that insofar as there are solutions for which the ratios λ_c/λ_o and A/A_c are the same regardless of whether inner our outer boundary conditions will be applied,

the explicit solution is completely independent of the boundary conditions. Hence, inner or outer boundary conditions need to be applied separately to pick out the inflow or outflow solutions, respectively.

As Bondi pointed out in his 1952 paper, $\Lambda = \dot{m}/\dot{m}_c$ acts as an eigenvalue in that each value of Λ corresponds to a unique set of branches, or sets of points in the (χ, w)-plane that correspond to the two roots of the non-linear function $R(w, \chi) \equiv F(w) - \Lambda^{-2\frac{\gamma-1}{\gamma+1}} X(\chi) = 0$. He was the first to show that the solution possesses an X-type topology containing both (physically acceptable) single-valued branches for $\Lambda < 1$ and (unphysical) double-valued branches for $\Lambda > 1$. For $\Lambda < 1$, one root defines a subsonic branch with $w < 1$ and the other a supersonic branch in which $w > 1$ everywhere. This property makes the root-finding procedure for w straight forward, since for a given χ, the two roots w_1 and w_2 are always bracketed by $0 < w_1 < 1$ and $1 < w_2 < 10+$. For the unphysical $\Lambda > 1$ solutions, one root defines a sub-critical branch with $\chi < \chi_c$ and the other a super-critical branch with $\chi > \chi_c$ always. As $\Lambda \to 1$ from slightly above or below 1, either pair of branches approach each other, bending ever more toward the critical point, and finally join each other at the single point χ_c for $\Lambda = 1$, thus forming the transonic solutions. See Parker (1960) or Holzer & Axford (1970) for plots of the solution topology just summarized.

The Transonic Solutions

Bondi (1952) also explained why the maximum value of Λ occurs for the branches that pass through the critical point. We reiterate his logic linking the maximum moss-loss rate to the transonic solution, since it follows from simple mathematical considerations. For $\gamma > 1$, both F and X are well-behaved functions with minimum values, so a solution ceases to exist when the right hand side of equation (5.45) becomes smaller than the minimum of the left hand side, F_{min}. The product $\Lambda^{-2\frac{\gamma-1}{\gamma+1}} X(\chi)$ is made smallest for some X_{min} and

Λ_{max}. Therefore,

$$\Lambda_{max} = \left(\frac{F_{min}}{X_{min}} \right)^{\frac{\gamma+1}{2(\gamma-1)}} . \tag{5.46}$$

It is easily seen that F_{min} occurs for $w = 1$, i.e. $w = w_c$, at which value $F_{min} = .5(\gamma + 1)/(\gamma - 1)$. Evidently, $X_{min} = F_{min}$ is found at χ_c, which can readily be verified because equation (5.39) must hold at the critical point. Thus,

$$\Lambda_{max} \equiv \Lambda_c = 1. \tag{5.47}$$

The double-valued solutions that occur for $\Lambda > 1$ must accordingly have $X > X_{min}$, or equivalently $\chi < \chi_c$ or $\chi > \chi_c$ for all χ, to satisfy equation (5.45), this property having just been mentioned.

In practical terms, we have just shown that physically acceptable solutions obey $\Lambda \leq 1$ and that to obtain the transonic solutions, simply set $\Lambda = 1$. Of course, hindsight into the nature of the problem led to this convenient choice of Λ, also made by Holzer & Axford (1970).

Our formulation of the problem for $1 < \gamma < 5/3$ is now complete. In Appendix A, we provide formulae to compute all other variables and quantities of interest from the ones already given. We apply our formalism to recover the solution of the Bondi problem in Appendix B.

5.7 The Isothermal Solution

For an isothermal ($\gamma = 1$) EoS, the entire problem can be compactly solved in terms of the Lambert W function.[7] Also aptly called the product logarithm, the Lambert W

[7]The Wolfram demonstration project entitled 'The Solar Wind' (http://demonstrations.wolfram.com/TheSolarWind/), contributed by Ana-Maria Piso, alerted us to the use of the Lambert W Function to solve the isothermal equation of motion.

function is really a set of functions, defined as those satisfying

$$W(z)\exp[W(z)] = z, \tag{5.48}$$

z being the independent variable. In general, both z and $W(z)$ are complex variables. The many properties of $W(z)$ and several of its uses in physics can be found in (Valluri et al. 2000 and references therein). The essential properties of the Lambert W function, for our purposes, occur when $z = \chi$ is real. In that case, equation (5.48) can have two real solutions, conventionally referred to as $W_0(\chi)$ and $W_{-1}(\chi)$. $W_0(\chi)$ turns out to contain the everywhere subsonic branch of the transonic solution, and $W_{-1}(\chi)$ the everywhere supersonic branch. The advantage of using the Lambert W function is that both $W_0(\chi)$ and $W_{-1}(\chi)$ are built in to Mathematica, Maple, and MATLAB. We used this solution method to expediently survey the parameter space of our disk wind results, to visualize our isothermal solutions, and to calculate the results presented in §6.1. In addition, having a solution in terms of the Lambert W function is certainly advantageous for pedagogical purposes.

We can arrive at the isothermal solution by taking the limit as $\gamma \to 1$ of our explicit solution to the polytropic problem, equation (5.45). It follows more readily, however, by integrating the equation of motion, which for $\gamma = 1$ is reduced to

$$F \equiv \left(1 - \frac{1}{w}\right) w' + 2\left(g - \frac{\mathrm{A}'}{\mathrm{A}}\right) = 0. \tag{5.49}$$

Recalling that $g = dU_{eff}/d\chi$, we obtain

$$\ln w - w = 2[U_{eff} - \ln(\mathrm{A}/\mathrm{A}_o)] + constant, \tag{5.50}$$

where we have absorbed a factor of $\ln \mathrm{A}_o^{-2}$ into the constant. Exponentiating and multiplying by -1 gives

$$-w\exp(-w) = -\Gamma_B^2 \left(\frac{\exp[U_{eff}]}{\mathrm{A}/\mathrm{A}_o}\right)^2. \tag{5.51}$$

Here, Γ_B is a constant; it turns out to be the initial Mach number in a generalized Bondi problem (where A_o is the area at the outer boundary, not necessarily located at $r_o = \infty$), in that $d\dot{M}_c = \rho_o c_o A_o \Gamma_B$ gives back the known accretion rate of the isothermal Bondi problem (see Appendix B). The magnitude of Γ_B can be large ($\sim 10^2$) when A_o represents the area of the inner boundary. The value of Γ_B is obtained by evaluating equation (5.51) at the critical point, giving

$$\Gamma_B = \frac{\mathrm{A}_c}{\mathrm{A}_o} \exp\left[-\frac{1}{2} - U_{eff}(\chi_c)\right]. \tag{5.52}$$

'Operating' on both hand sides of equation (5.51) with the Lambert W function isolates $-w$. Hence, the solution in terms of the Mach number $\mathcal{M} = \sqrt{w}$ is

$$\mathcal{M}(\chi) = \sqrt{-W\left[-\left(\Lambda\Gamma_B \frac{\exp[U_{eff}(\chi)]}{\mathrm{A}(\chi)/\mathrm{A}_o}\right)^2\right]}. \tag{5.53}$$

We have re-introduced Λ into equation (5.53) to distinguish the transonic ($\Lambda = 1$) solutions from the everywhere sub/supersonic solutions ($\Lambda < 1$). Here again, setting $\Lambda > 1$ yields nonphysical, double-valued solutions.

The location of the critical point is obtained directly from equation (5.39); χ_c must satisfy

$$g_c = \frac{\mathrm{A}_c'}{\mathrm{A}_c}. \tag{5.54}$$

For our disk wind models, g_c is given by equation (5.32) and $\mathrm{A}_c'/\mathrm{A}_c = q\cos i/(f + \chi_c \cos i)$, where $q = 1$ for the CIA and model and $q = 2$ for the Converging model. Due to the non-linear dependence on $\cos i$, χ_c must again be solved for numerically. For the spherically symmetric Parker model, meanwhile, $\mathrm{A}_c'/\mathrm{A}_c = 2/(f+\chi) = 2/(r/r_g)$ (recall that $r_g = \lambda_o r_o$), while the gravitational force is simply $g = 1/(r/r_g)^2$. We immediately recover the well known sonic point distance $r_c = r_g/2$ from equation (5.54). The cylindrical Parker wind model (i.e. the CIA model at $i = 0^\circ$) discussed in §5.1 also has $g = 1/(r/r_g)^2$, while

$\mathrm{A}_c'/\mathrm{A}_c = 1/(r/r_g)$, giving $r_c = r_g$. We can therefore in general expect the CIA model to have critical points approximately twice as distant from those of the Converging model.

The mass loss rate is calculated from $d\dot{M} = \dot{m}A_o$ by knowing the mass flux density, $\dot{m} = \rho_o c_o \mathcal{M}_o$. From equation (5.53), we find that

$$\mathcal{M}_o = \sqrt{-W\left[-(\Lambda\Gamma_B)^2 \exp(-2\lambda_o + \zeta^2)\right]}. \tag{5.55}$$

It remains to solve for the critical mass flux density, $\dot{m}_c$, by way of the equation of motion, and show that it is consistent with $\mathcal{M}_o$ when $\Lambda = 1$. To proceed, recall that the enthalpy $h = c_s^2 \ln(\rho/\rho_c)$ rather than $c_s^2/(\gamma - 1)$ [see equation (5.7)]. We also have that $\lambda_c = \lambda_o$ for $\gamma = 1$ because the sound speed is constant. Then the dimensionless Bernoulli equation is

$$e_c = \frac{\mathcal{M}^2}{2} + U_{eff} + \ln(\rho/\rho_c). \tag{5.56}$$

The critical point constant, when evaluated at the critical point, again results in an independent constant,

$$e_c = \frac{1}{2} + U_{eff}(\chi_c). \tag{5.57}$$

However, the correspondence of equation (5.57) with the the critical point constant of our polytropic solution is far from exact due to the liberty we took in defining the enthalpy as $\ln(\rho/\rho_c)$. With this choice, $e_c < 0$, implying a negative Bernoulli constant B_o, whereas e_c tends to infinity for $\gamma \to 1$ in equation (5.35). The diskrepancy arises because the internal energy density is infinite for an isothermal EoS, allowing gas to still escape to infinity regardless of whether or not it is gravitationally bound. Suffice it to say that transonic solutions do not exist for $1 < \gamma < 5/3$ unless B_o is positive (Holzer & Axford 1970), and furthermore, B_o should increase as γ decreases from 5/3 to 1 (e.g., Blandford & Begelman 1999), as seen by equation (5.35).

Comparing equation (5.57) with equation (5.52), we can now write the generalized Bondi accretion rate as simply

$$\Gamma_B = (\mathrm{A}_c/\mathrm{A}_o)\exp(-e_c). \tag{5.58}$$

The density at the critical point is found by evaluating equation (5.56) at the lower boundary,

$$\frac{\rho_c}{\rho_o} = \exp(-e_c)\exp\left[-\lambda_o + \frac{\zeta^2}{2} + \frac{\mathcal{M}_o^2}{2}\right]. \tag{5.59}$$

In turn, ρ_c/ρ_o is used to evaluate the critical mass flux density. From the continuity equation, $\dot{m}_c = \rho_o c_o(\mathrm{A}_c/\mathrm{A}_o)(\rho_c/\rho_o)$, or

$$\dot{m}_c = \rho_o c_o \Gamma_B \exp\left[-\lambda_o + \frac{\zeta^2}{2} + \frac{\mathcal{M}_o^2}{2}\right]. \tag{5.60}$$

This equation for $\dot{m}_c$ can be rewritten as a non-linear equation for $\mathcal{M}_o$ because $\mathcal{M}_o = \dot{m}_c/\rho_o c_o$. As mentioned above, it is required that equation (5.60) be consistent with equation (5.55) when $\Lambda = 1$, which can readily be verified using the Lambert W function. To an excellent approximation when $\mathcal{M}_o << 1$ (valid when $\lambda_o >> 1$),

$$\dot{m}_c = \rho_o c_o \Gamma_B \exp\left[-\lambda_o + \frac{\zeta^2}{2}\right]. \tag{5.61}$$

We see that $\dot{m}_c$ is always smaller than $\rho_o c_o \Gamma_B$ because the highest rotational velocity is typically the Keplerian value, $\zeta^2 = \lambda_o$ (corresponding to the breakup speed for stars).

With $\dot{m}_c$ in hand, the density distribution follows immediately from the continuity equation,

$$\frac{\rho(\chi)}{\rho_o} = \frac{\Lambda\Gamma_B \exp\left[-\lambda_o + \zeta^2/2 + \mathcal{M}_o^2/2\right]}{(\mathrm{A}(\chi)/\mathrm{A}_o)\mathcal{M}(\chi)}. \tag{5.62}$$

It should be verified that $\rho(\chi = 0)/\rho_o = 1$ upon implementation of these equations.

The barometric law that we quoted in §3 is derived from equation (5.62). We consider a spherically symmetric ($\zeta = 0$) Parker wind applied to a isothermal planetary atmosphere.

Taking r_o to be the radius of the exobase, ρ_o is the density at this height. Such an atmosphere can be modeled as a transonic Parker wind if, in the steady state, the top level of the atmosphere is itself moving at speeds approaching the speed of sound at the exobase. On the other hand, a static atmosphere, undergoing mass loss via evaporation, should approximately resemble a Parker wind solution with $\dot{m} << \dot{m}_c$ (corresponding to an everywhere subsonic solution with a finite density at infinity). Looking to equation (5.53), we see that for small mass-loss rates ($\Lambda << 1$), the argument of W is small and it is valid to expand W to leading order.[8] Thus, equation (5.62) becomes

$$\rho = \rho_o \exp\left[\lambda_o(r_o/r) - \lambda_o + \mathcal{M}_o^2/2\right]. \tag{5.63}$$

For a strictly static atmosphere ($\mathcal{M}_o = 0$), we recover a barometric law, but one derived from hydrodynamic (rather than hydrostatic) equilibrium.

[8] $W(x) \approx x - x^2 - \frac{3}{2}x^3 + \ldots$

CHAPTER 6

RESULTS

6.1 Global Scaling Relationships

The issue we address here is how the functional forms of our solutions can be used as scaling relationships to calculate the properties of a multi-dimensional 'global' disk wind model. This topic is especially relevant to studies of protoplanetary disks, as discussed in §3.3. Of primary importance in this regard is the mass flux density for transonic winds, $\dot{m}_c = \rho_o c_o (\mathrm{A}_c/\mathrm{A}_o)(\rho_c/\rho_o)$. Significant diskrepancies in the integrated (global) mass-loss rate, $\dot{M} = 4\pi \int_{r_{in}}^{r_{out}} \dot{m}_c \sin i \, r_o dr_o$ can arise from model-dependent differences in the assumed or calculated value of the initial velocity (see, e.g. Figure [7] in Font et al. 2004). In other words, the primary source of uncertainty resides in the determination of the initial Mach number of the flow, since $\dot{m}_c = \rho_o c_o \mathcal{M}_o$, and both ρ_o and c_o are ordinarily determined or prescribed by independent means. For instance, GH09 combine a realistic treatment of the photevaporative heating process in protoplanetary disks by separately calculating the isothermal EUV ionization front and the FUV and X-ray heated neutral flow surface, thereby self-consistently determining the base density and temperature on the flow boundary, which extends spherically through some solid angle above and below the disk midplane at the location $r = r_o$, and hence provides $\rho(r = r_o) = \rho_o(z)$ and $c_s(r = r_o) = c_o(z)$. Since their radiative transfer calculation assumed hydrostatic equilibrium ($\mathcal{M}_o = 0$), the hydrodynamics had to be included separately to calculate $\mathcal{M}_o$. Employing isothermal Parker wind solutions offer a convenient way to accomplish this, for c_o enters only through the HEP and the solutions are independent of ρ_o. Given a value of the HEP, isothermal Parker wind solutions uniquely specify the sonic point distance from equation (5.54) and the corresponding initial Mach number, equation (5.55).

Figure 6.1. $\mathcal{M}_o$ vs. r_o/r_g for the extrapolated streamline function of GH09. The dashed curve is the approximate initial Mach number, given by equation (6.2), which is smaller than that derived from the scaling relationships used by GH09 (solid line) by a factor of $\exp(-0.5)$. The dotted curve is the exact $\mathcal{M}_o$ (equation (5.55)) in terms of the Lambert W function, which naturally terminates at $\mathcal{M}_o = 1$ because the Lambert W function becomes complex. This plot shows that GH09's extrapolation procedure gives sensible predictions for $\mathcal{M}_o$, but the integrated mass-loss rate can nevertheless differ substantially from that calculated using the exact solution in the region $0.1r_g < r_o < r_g/2$.

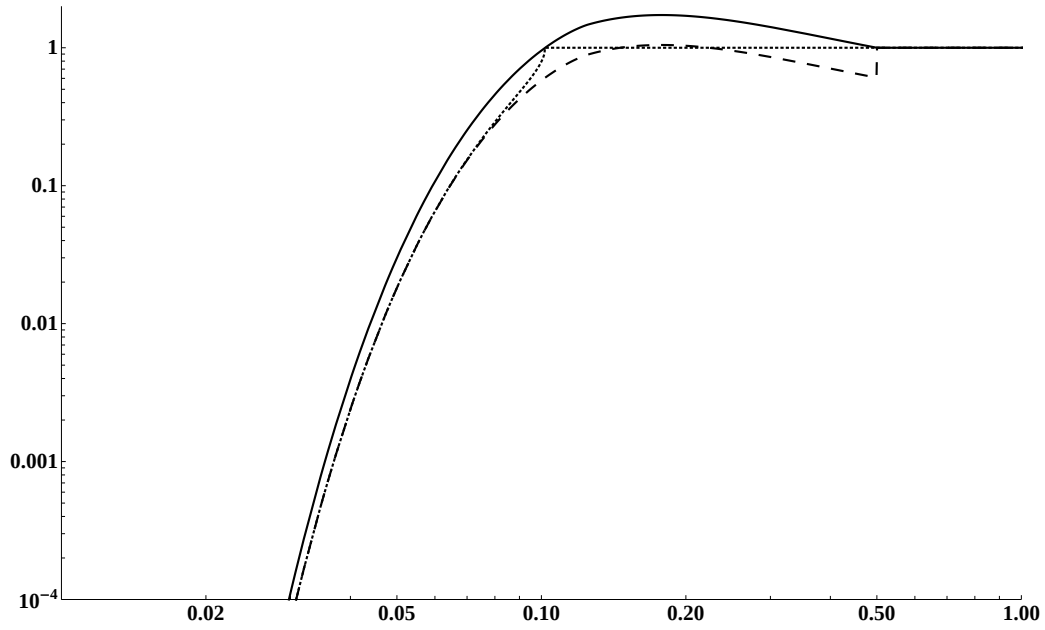

In estimating global mass loss rates from protoplanetary disk winds with Parker winds, however, several difficulties present themselves: (i) $\mathcal{M}_o$ depends sensitively on the the effective potential and the area occupied by the flow at the sonic point (see equation (5.52)); (ii) the parameter space of isothermal Parker wind solutions is $2 < \lambda_o < \infty$ if there is no rotation and $\sim 10 < \lambda_o < \infty$ for Keplerian rotation[9], implying for $r_g = constant$ that $\mathcal{M}_o$ can only be evaluated out to a distance of $r_o = r_g/2$ and $r_o = r_g/10$, respectively, while for $r_g = r_g(r_o)$, the temperature constraint given by the inequality (3.7) must be satisfied; (iii) the boundary of a Parker wind is a spherical surface at the footprint of the radial streamlines and cannot be used to realistically approximate a 'vertical' outflow. Difficulty (iii) limited the studies of Adams et al. (2004) and GH09, in that they could only consider radial outflows through some solid angle. Our models retain the simplicity of Parker winds, while providing a geometric boundary on which to apply physical conditions for biconical outflows.

As we described in §3.3, GH09 extrapolated between the critical point equations of various Parker wind solutions to overcome difficulty (ii). Specifically, they approximated the sonic surface with the formula

$$\frac{r_c}{r_o} = \begin{cases} \lambda_o(1+\sqrt{1-8/\lambda_o})/4, \text{ if} & \lambda_o \geq 8 \\ (\lambda_o/2+2)/3, \text{ if} & 2 \leq \lambda_o < 8 \\ 1, \text{ if} & \lambda_o < 2 \end{cases} \tag{6.1}$$

Using equation (6.1) along with their numerical results for ρ_o and c_o, GH09 obtained the mass flux density as a function of r_o by utilizing the scaling relationship for $\dot{m}$ derived by Adams et al. (2004). The latter is essentially equation (5.61), rewritten in terms of

[9]Despite there being well-defined critical points down to $\lambda_o = 8$ as implied by the critical point equation for an isothermal Parker wind with Keplerian rotation, $r_c/r_o = (\lambda_o/4)(1+\sqrt{1-8/\lambda_o})$, by plotting the isothermal solution presented in §5.7, it can be seen that there is not actually a continuous transonic solution for $\lambda_o < 9.83$.

$\mathcal{M}_o = \dot{m}/\rho_o c_o$ with Keplerian rotation ($\zeta = \sqrt{\lambda_o}$) assigned:

$$\mathcal{M}_o \approx \Gamma_B \exp(-\lambda_o/2), \tag{6.2}$$

where

$$\Gamma_B = \left(\frac{r_c}{r_o}\right)^2 \exp\left[\lambda_o \left(\frac{r_c}{r_o}\right)^{-2} \left(\frac{r_c}{r_o} - \frac{1}{2}\right) - \frac{1}{2}\right]. \tag{6.3}$$

It is informative to assess the global wind properties that arise from this extrapolation procedure, all of which can be derived from $\mathcal{M}_o$. We therefore confine our attention to calculating $\mathcal{M}_o$, and for simplicity we consider a disk with a constant temperature profile so that r_g is constant.

As stated in Adams et al. (2004), equation (6.2) is strictly valid when $r_o << r_g$, i.e. when $\lambda_o >> 1$, but approximately holds for larger r_o also. In Figure 6.1, we illustrate the error arising from this approximation to the exact solution, as well as the error resulting from the use of the extrapolated sonic point function. The three curves shown are the initial Mach number given by equation (6.2) (dashed line), the exact relation for $\mathcal{M}_o$ (dotted line) in terms of the Lambert W function, equation (5.55), and the expression that we derived for $\mathcal{M}_o$ based on equations (3)-(5) in GH09 (solid line), which does not include the factor of $\exp(-0.5)$ that enters through e_c. We see that our approximate and exact expressions for $\mathcal{M}_o$ are equivalent until $\mathcal{M}_o \approx 0.5$, and differ substantially at larger radii due to difficulty (i). The Lambert W function solution terminates once $\mathcal{M}_o = 1$ at $r_o \approx r_g/10$ (and we extended the curve to remain at $\mathcal{M}_o = 1$ thereafter). The dashed line peaks at $\lambda_o \approx 5.4$, for which value $\mathcal{M}_o \approx 1.05$, while the solid line peaks at $\mathcal{M}_o \approx 1.5$ and for $r_o > r_g/2$ takes the constant value 1.0. This plot indicates that use of equation (6.1) without the factor of $\exp(-0.5)$ will lead to an overestimate of the total mass-loss rate (and an underestimate with this factor) compared to a calculation that implements exact Keplerian Parker wind

Figure 6.2. Equivalent nozzle function, $N(\chi)$, vs. χ, normalized so that $N(\chi_c) = \mathcal{M}_o$ as given by equation (6.2). The topmost dashed-dotted curve is the nozzle function for a Keplerian Parker wind, followed by that of the Converging (dashed) and CIA (solid) models for $i = 60^\circ$. The bottom dotted curve is for the spherically symmetric Parker wind. Rotating these nozzle functions about the χ-axis sweeps out the area of the de Laval Nozzle, one with steady-state flow properties identical to that of the wind. The horizontal lines give the exact value of the initial Mach number, calculated using equation (5.55). They are, from top to bottom, $\mathcal{M}_o = [0.497, 0.134, 0.036, \&0.002]$, with corresponding critical points (throat positions) $\chi_c = [0.290, 0.333, 0.779, 0.409]$. All nozzle functions were calculated with $\lambda_o = 11$. The hump on the topmost curve is a bulk velocity minimum, located at $\chi = 0.029$.

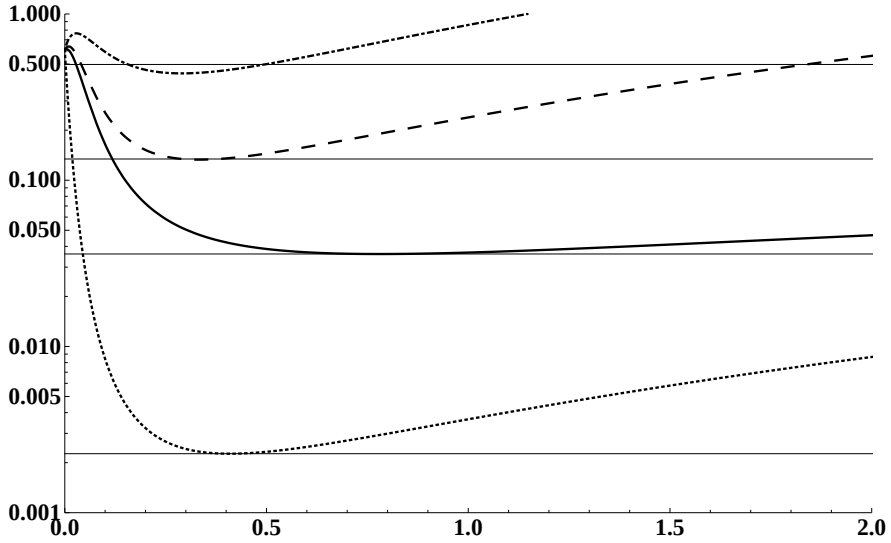

solutions based on the Lambert W function. In other words, the simplest way to overcome difficulty (ii) is to merely assume that $\mathcal{M}_o = 1$ for $r_o \gtrsim r_g/10$. Again, this example assumed that r_g is constant, so it is merely illustrative and may not have a direct bearing on the results of GH09.

The Equivalent Nozzle Function

A useful proxy for gauging the error in the initial Mach number more generally, and to thereby further address difficulty (i), is obtained by defining the equivalent nozzle function. The well-known equation of motion for the de Laval nozzle is, in our notation,

$$\left(1 - \frac{1}{w}\right) w' = 2\frac{N'}{N}, \tag{6.4}$$

where $N = N(\chi)$ is the cross-sectional area of the nozzle at any distance χ. Making the comparison with equation (5.49), $N(\chi)$ is obtained by solving $d \ln N = d \ln A - dU_{eff}$, giving

$$N(\chi) = \frac{A(\chi)}{A_o} \exp\left[-U_{eff}(\chi) - \left(\lambda_o - \frac{\zeta^2}{2} + \frac{1}{2}\right)\right]. \tag{6.5}$$

We have normalized $N(\chi)$ so that at the critical point, χ_c, it equals the approximate $\mathcal{M}_o$, given by equation (6.2). Since the critical point occurs at the 'throat' of the nozzle, where the cross-sectional area is a minimum, $N(\chi)$ is a visual tool that can be used to find both the sonic point and the approximate initial Mach number (and hence mass-flux density) by inspection. In Figure 6.2, we plot the nozzle functions of the Keplerian rotating Parker wind (dashed-dotted line), the Converging Model at 60° (long-dashed line), the CIA model at 60° (solid line), and the spherically symmetric Parker wind (dotted line) for $\lambda_o = 11$. The horizontal lines correspond to the exact value of the initial Mach number from equation (5.55). We see that all of the horizontal lines except that of the Keplerian Parker wind with $\mathcal{M}_o \approx 0.5$ intersect very near the minimums of the nozzle functions, showing that equation (6.2) is a very good approximation when $\mathcal{M}_o$ is small.

A noticeable feature of the nozzle functions is the initial hump close to the opening (near $\chi = 0$) for the models undergoing Keplerian rotation. The spherically symmetric Parker wind nozzle is everywhere converging before the throat and diverging thereafter, thus ensuring that the flow will never decelerate. The presence of the humps indicates that the flow is entering a diverging nozzle ($N' > 0$), so that for initially subsonic flow, we must have $w' < 0$ by equation (6.4): the flow decelerates until reaching the top of the hump where $N' = 0$. The flow is still subsonic at this location, implying that the acceleration must be zero ($w' = 0$), i.e. the flow has reached its minimum velocity. The flow then proceeds to accelerate with the converging nozzle, traverse the sonic point at the throat where $w = 1$ and $N' = 0$ (but $w' \neq 0$), and continues to accelerate supersonically ($w' > 0$ and $w > 1$) in

the diverging region where $N' > 0$. Hence, we can understand the general characteristics of the wind velocity profile simply by examining the shape of the nozzle function.

Moreover, plotting $N(\chi)$ allows one to easily infer the effects of altering the geometry of the flow or the effective potential. For instance, the humps practically disappear by setting $A(\chi) = A_o$. Recalling Figure 1.2, the streamlines found by Luketic et al. (2010) first originate from the disk midplane in a more vertical fashion before bending radially, implying that the area between streamlines indeed behaves as if $A(\chi) = A_o$ for very small χ. Therefore, it is likely that the velocity minimums would not occur in a model that captures this feature, although it is worth noting that Luketic et al. (2010) observe non-monotonic radial velocity profiles in their fiducial run (see their Figure 5).

Comparing the nozzle functions of the CIA and Converging models, it is clear that the former model has a sonic point about twice as distant as the latter, as expected. Closer sonic points imply smaller initial Mach numbers for a given HEP, and since $\mathcal{M}_o$ is a direct gauge of the mass flux density, the total mass loss rate for a CIA wind will also be smaller in general. These differences all result from the halted expansion room of the CIA model, as will become clear in §6.2. Both winds experience a reduced centrifugal force at $i = 60°$, explaining why the Keplerian Parker wind has a significantly higher initial Mach number. We can therefore arrive at the result that the mass flux densities of our disk wind models are always bounded from below by that of the spherically symmetric Parker wind and above by that of the Keplerian Parker wind.

The Mass Flux Density for Isothermal vs. Polytropic Winds

From equation (6.2), the initial Mach number of our isothermal solutions scale as $\exp(-\lambda_o/2)$, and this term controls the mass flux density ($\dot{m} = \rho_o c_o \mathcal{M}_o$) for large HEP. The exponential dependence results from the logarithmic enthalpy term and acts to suppress the

wind whenever when the thermal energy of the gas is small compared to the escape velocity, e.g. when the gas is deep in the potential well of the inner disk region and shielded from high energy photons. Adams et al. (2004) explored the dependence of the mass loss rate on the factor $\exp(-\lambda_o/2)$ in detail, showing that sub-critical disks that are subjected to modest to high FUV radiation field intensities can undergo total mass loss rates on the order of $10^{-7}\,M_\odot\,yr^{-1}$ if their host stars have masses under 1 $M_\odot$, implying disk dispersal time-scales of ~ 10 Myr — roughly the time-scale for planet formation.

As we mentioned in the introduction, BMS83 found the same exponential dependence in their isothermal wind region E, namely $\dot{m} \propto \exp(-T_g/2T_{IC})$, where T_g is the 'escape temperature' defined by $kT_g = \mu m_p V_{esc}^2$. To make the comparison explicit, we must recall equation (**??**), which for $\gamma = 1$ and $\xi = r_o/R_{IC} = T_{IC}/T_g$, says that the HEP is simply $\lambda_o = T_g/T_o$. For a tightly bound corona heated to the Compton temperature, $T_o = T_{IC} < T_g$, and we can indeed identify the HEP as being equal to T_g/T_{IC}.

Similar agreement can be found using polytropic models, which are able to sample a larger range of thermodynamic conditions and can therefore lead to more accurate disk dispersal time-scale estimates. The procedure for incorporating the hydrodynamics 'by hand' using Parker wind or Parker-like disk wind models is the same as that given above, the only change being that the initial Mach number is now given by $\mathcal{M}_o = (\mathrm{A}_c/\mathrm{A}_o)(\lambda_o/\lambda_c)^{\frac{\gamma+1}{2(\gamma-1)}}$. (Correspondence with the isothermal result can be obtained using $\rho_c/\rho_o = (\lambda_o/\lambda_c)^{1/(\gamma-1)}$.) Thus, for polytropic winds, the exponential terms in equation (6.2) are replaced by a strong functional dependence on the temperature at the sonic point ($\lambda_o/\lambda_c = T_c/T_o$), so the mass flux density scales as

$$\dot{m} = \rho_o c_o (\mathrm{A}_c/\mathrm{A}_o) \left(\frac{T_c}{T_o}\right)^{\frac{\gamma+1}{2(\gamma-1)}} . \tag{6.6}$$

For $\gamma = 5/3$, we recover the temperature dependence found by BMS83 in their Region C,

namely $\dot{m} \propto (T_c/T_o)^2$. (To make the comparison with BMS83, T_c is to be associated with their 'characteristic' temperature T_{ch} and T_o with T_g, obeying $T_{ch} < T_g < T_{IC}$.)

By equation (5.39), we can instead express the initial Mach number as

$$\mathcal{M}_o = \frac{\mathrm{A}_c}{\mathrm{A}_o} \left(g_c \frac{\mathrm{A}_c}{\mathrm{A}'_c} \right)^{\frac{\gamma+1}{2(\gamma-1)}} . \tag{6.7}$$

Recalling difficulty (i), we see that $\mathcal{M}_o$ now depends sensitively on the effective gravitational force instead of $\exp(-U_{eff})$, as well as on the ratio of the flow tube area and the streamline divergence at the critical point.

From this section it should be clear that the full range of initial Mach numbers from nearly 0 to 1 can result from a relatively small range of HEP values, the lowest of which yield winds launched from nearly sonic speeds. This sensitivity becomes more extreme as the polytropic index is increased from 1 to 5/3. In the remainder of §6, we explore the parameter space of polytropic transonic solutions in detail, to convey a sense of the diversity of wind solutions that are mathematically permitted.

6.2 Parameter Survey of Polytropic Transonic Disk Wind Solutions

The parameter space of our disk wind models is all values of (γ, λ_o, i) that lead to transonic solutions. We limit our attention to two intermediate angles $i = 30^\circ$ and $i = 60^\circ$. We survey this parameter space in Figure 7.1 by plotting critical point distances ($\lambda_o \chi_c = l_c/r_o$) vs. HEP for select γ ranging from nearly isothermal ($\gamma = 1.01$) to adiabatic ($\gamma = 5/3$).

The top most panel of Figure 7.1 shows that for the Converging model, nearly isothermal winds become sonic slightly within a distance of $l_c/r_o = \lambda_o/2 - 1$ from the disk midplane, while the CIA model has a sonic distance about twice a great. For comparison, recall from §5.7 that spherically symmetric isothermal Parker winds have $r_c/r_o = 1 + l_c/r_o = \lambda_o/2$. As γ increases, subsequent panels show that CIA critical points are shifted still further

downstream of Converging model critical points. Also, transonic solutions at higher γ require progressively smaller HEP values, only the smallest of which yield critical points under $\sim 10r_o$. Transonic solutions with the least distant critical points have very high initial Mach numbers and delimit the edge of the parameter space. Two plots of $\mathcal{M}_o$ vs. λ_o are shown by the inset plots on the $\gamma = 1.2$ and $\gamma = 1.5$ panels. $\mathcal{M}_o$ typically ranges from ~ 1 for the closest critical points to less than 10^{-3} for the most distant critical points.

The inset plot in the $\gamma = 1.2$ panel of Figure 7.1 demonstrates the primary effect of changing the inclination angle. For a given HEP in either model, e.g. $\lambda_o = 8$, the $i = 60^\circ$ solutions are launched with smaller initial Mach numbers than the $i = 30^\circ$ solutions. This is a simple consequence of the reduction in centrifugal force at larger inclination angles. The extra rotational energy raises $\mathcal{M}_o$ for $i = 30^\circ$ above $\mathcal{M}_o$ for $i = 60^\circ$. Conversely, the reduced centrifugal force for $i = 60^\circ$ permits critical points to extend to smaller HEP (e.g., higher temperatures) before reaching $\mathcal{M}_o \approx 1$.

A peculiar feature of Figure 7.1 is the appearance of a 'tail' on the critical point curves, signifying that at the lowest HEP for any given curve with $\gamma \gtrsim 1.2$, there are two transonic solutions. The tail transonic solution has its sonic point in close proximity to the disk and therefore has a higher initial Mach number than the second solution. As γ increases, this tail grows in length, while the 'normal' critical point curve shrinks. Only the tail extends beyond the vertical lines at $\lambda_o = 2/(\gamma - 1)$; to the right of this line, solutions have higher initial velocities than they do terminal velocities. Notice that the normal critical point curve has the property that the sonic point distance increases with increasing HEP (e.g., with smaller temperatures), as one would intuitively expect. Meanwhile, the tail displays the opposite behavior, so that more distant sonic points with lower initial Mach numbers have *higher* temperatures. We postpone further discussion of these features, as they are

addressed in §7.

Our parameter survey reveals that disk winds possess solutions for $\gamma = 5/3$, in contrast to Parker winds (both with and without rotation). Figure 7.2 shows that the Converging model has solutions to the right of the vertical line for a narrow range of HEP around $\lambda_o = 3.9 \pm 0.05$ for $i = 60^\circ$. The bottom panel reveals that these solutions also have $\mathcal{M}_o \approx 1$, making them very unrealistic. There are no solutions for the Converging model at $i = 30^\circ$ for $\gamma = 5/3$ (at least not within $l = 10^3 r_o$). Meanwhile, the CIA model has viable transonic solutions to the left of the vertical line (i.e. with $v_o < v_\infty$), permitting small initial Mach numbers.

Overall, this parameter survey indicates that purely geometric differences, attributable to the CIA model's lack of streamline divergence, give rise to the more versatile CIA wind. At small γ (i.e. in the top three panels of Figure 7.1), the CIA model has transonic solutions that begin for λ_o about half as small as the minimum HEP allowed for the Converging model. At larger γ, the critical points for the CIA model span a more appreciable range of HEP and altogether dominate for $\gamma = 5/3$.

Physically, these geometric effects are a manifestation of the rate of enthalpy dissipation. Just considering the Bernoulli function, it is clear that the more rapidly that heat is liberated, the faster the flow must become to keep B_o constant. Converging streamlines exhibit both lateral expansion due to streamline divergence and azimuthal expansion as the wind cone widens, so the enthalpy can dissipate faster than it can with the CIA model. Conversely, the confined expansion imposed by the CIA streamline configuration allows the flow to retain more of its enthalpy as it expands, so that the flow can be launched at smaller λ_o before the initial Mach number approaches unity. As γ increases and the flow starts off with less enthalpy, a smaller compensatory reduction in HEP is required to launch

transonic solutions compared to the Converging model. These considerations imply that the acceleration zones of these two models will be substantially different, which is our next result.

6.3 Disk Wind Acceleration Zones

Each critical point location given plotted in 7.1 has an associated acceleration zone, which we define as the distance where the flow reaches 90% of its terminal velocity, i.e. the location l at which $v(l)/v_{esc} = 0.9\sqrt{e_c/\lambda_c}$ (see equation (A.3)). In Figure 7.3 we plot the wind acceleration zone as a function of HEP for $i = 60^\circ$ and various γ intermediate between the isothermal and adiabatic flow regimes. This plot is useful for understanding the dependence of the flow behavior on the polytropic index for either disk wind model. A nearly isothermal wind has its temperature held constant to very large distances, so the acceleration zone extends far beyond a closer to adiabatic wind whose temperature falls off rapidly.

Figure 7.3 further illustrates how the CIA model gives rise to a very different wind than does the Converging model, again attributable to the CIA model's geometrical confinement curtailing adiabatic expansion. The acceleration zone of the CIA model lies beyond $l = 10^7\, r_o$ for $\gamma = 1.1$, whereas the Converging model has an acceleration zone within $l = 10^5\, r_o$ for $\lambda_o < 10$. We noted from Figure 7.3 that the sonic surface of the CIA model is roughly twice as distant as that of the Converging model. Apparently, a factor of two increase in the critical point distance translates into a two order of magnitude gain in the extent of the acceleration zone! As γ increases, the acceleration zone becomes progressively closer to the disk midplane, but there remains a two order of magnitude separation between our disk wind models.

Together, Figures 7.1 and 7.3 indicate that Parker-like disk wind solutions encompass a vast range of initial conditions and thermodynamic environments (by way of λ_o and γ). Owing to the variety of astrophysical systems and physical scales that we have in mind, it is certainly reasonable that the criteria for judging realistic solar wind solutions, namely $\mathcal{M}_o << 1$ and $l_c/r_o \lesssim 10$, should to be relaxed somewhat. While solutions that become sonic at great distances from the midplane need not be outright rejected, their flow parameters are in an implausible range, one that may have some bearing on the stability of the wind. Physically, distant sonic points imply that the outflowing subsonic gas will be subjected to disturbances that would not disrupt a flow with a smaller HEP or γ that is already supersonic. We therefore see that viable wind solutions probably possess a substantially more narrow HEP range than the full range yielding critical point solutions in each panel.

It is hoped that the solution properties laid out here can help to interpret the results of self-consistent, multi-dimensional, hydrodynamic simulations of disk winds. Such simulations typically calculate both the sonic surface and the acceleration zone, as these are fundamental properties of transonic wind solutions. Given the sonic point distance and the radial extent of the acceleration zone, our Figures 7.1 and 7.3 together yield the corresponding HEP and γ of a Parker-like disk wind solution. Further examining the shape of the streamlines calculated in the simulations, the inclination angle and streamline divergence can be estimated, thereby permitting the simulation results to be approximated by either the CIA or the Converging model. By comparing the velocity, density, temperature, and Mach number profiles of the simulation results with our 1D models, it is then possible to systematically address the effects of taking into account additional processes in the simulations. In the remainder of this section, we tabulate and plot illustrative transonic disk wind solutions.

6.4 The CIA vs. the Converging Model

Here we compare transonic solutions for our two streamline geometries. Recalling our Figure 4.1, the 2D disk wind model that we are attempting to explore with our 1D solutions is comprised of two wind regions. The inner region hosts Converging streamlines beginning at $i \approx 60^\circ$, that then diverge out to some distance along the midplane until the inclination angle coincides with that of the outer wind region, occupied by CIA streamlines at $i \approx 30^\circ$.

We first make a comparison between the angles $i = 30^\circ$ and $i = 60^\circ$ for the same set of parameters (λ_o, γ) for either model. In Figure 7.4 we show the Mach number in the subsonic flow regions (upper panel), as well as the velocity and density profiles on a larger scale (lower panel), for solutions with $\lambda_o = 8$ and $\gamma = 1.2$. The properties of these solutions are tabulated in Table 2. The most striking difference between these models is the order of magnitude difference in their initial velocities. Since kinematic models typically assume a velocity law based solely upon v_o, v_∞, and a parameter controlling the slope of the velocity, the values of these quantities are sensitive to the type of wind geometry. Flow launched from $i = 30^\circ$ in either geometry have higher initial velocities due to the increased centrifugal force, in agreement with the $\gamma = 1.2$ panel of Figure 7.1. Despite having substantially different initial velocities, all four solutions tend to nearly the same terminal velocity because the Bernoulli constant $B_o = v_\infty^2/2$ should be unchanged for a similar set of wind parameters. Note that this is not obvious from the middle panel of Figure 7.4, as the CIA model, with its extended acceleration zone, has only reached $\sim 50\%$ of its terminal velocity while the Converging model is within $\sim 25\%$ of v_∞/v_{esc}. What is apparent from this panel is that the inclination angle only affects the transonic solutions in the subsonic flow regions.

The bottom panel of Figure 7.4 shows that the density of CIA model varies asymptotically as $\rho \propto l^{-1}$, whereas the Converging model has $\rho \propto l^{-2}$ (the dotted lines are plots

of $1/(1 + l/r_o)^q$, with $q = 1$ or 2 for comparison). This is a simple consequence of the continuity equation, the CIA model having an area term $A \propto l$ asymptotically. We see that the density at the critical point is smaller in the CIA model because the CIA wind remains subsonic out to distances three times as large as the Converging wind; the flow has a larger distance over which to expand. This difference also accounts for why the CIA model has a larger critical point constant and a smaller temperature at the critical point (recall that $\lambda_c/\lambda_o = T_c/T_o$) — see Table 2.

Comparing the slopes of bulk velocity profiles in Figure 7.4, it would appear as if the CIA wind has a higher velocity gradient. This is not the case, however, because the sonic points of the two wind geometries do not coincide. To accurately contrast the two flow accelerations, we must consider transonic solutions with the same sonic point distance. In Table 3 we list the properties of solutions that have $l_c/r_o \approx 10$ for two polytropic indices, $\gamma = 1.01$ and $\gamma = 4/3$. The velocity and density profiles for each solution is plotted in Figure 7.5. It is clear that the nearly isothermal Converging wind has the largest velocity gradient. The $\gamma = 1.01$ CIA wind requires a higher launching velocity due to its smaller value of the HEP. From Table 3, we see that the HEP of a nearly isothermal CIA wind must be about half that of a $\gamma = 1.01$ Converging wind. This has the following implication: for flow emerging from a region with the same escape velocity, the temperature must be twice as large to launch a CIA wind that becomes sonic at the same distance as a Converging wind. Conequently, the confined expansion results in a much denser nearly isothermal CIA wind at $l \gtrsim r_o$.

The density contrast between these two models at $\gamma = 4/3$ is reduced to within an order of magnitude. From the top panel, we see that the situation is somewhat reversed from the nearly isothermal case. Most obviously, it is required that the initial velocity be

substantially greater to compensate for the reduced energy input. This in turn requires higher temperatures or lower escape velocities, as reflected by the smaller values of the HEP in Table 3. It is evident from Figure 7.5 that the CIA model at $\gamma = 4/3$ has the larger velocity gradient and the smaller initial velocity. Furthermore, velocity minimums, which are barely visible for $\gamma = 1.01$, are now a prominent feature of the velocity profile. We mentioned in §4 that gas rotating at Keplerian speeds must initially decelerate upon leaving the disk, independent of the flow parameters. This is a simple consequence of equation (5.33); evaluated at $\chi = 0$ for $\zeta^2 = \lambda_o$, we have that $y' < 0$ provided $q > 0$, and $q = 1$ for the CIA model and 2 for the Converging model. For the $\gamma = 4/3$ Converging wind, the amount of deceleration is quite pronounced, persisting out to $l \approx r_o$.

6.5 Degenerate Transonic Solutions

As a final demonstration of our disk wind results, we focus on the solutions for the CIA model with $\gamma = 5/3$. Referring to to Figure 7.2, we aim to examine the two solutions that arise for the same HEP values for either angle shown. We selected $\lambda_o = 2.3$ for $i = 60^\circ$ and $\lambda_o = 2.9$ for $i = 30^\circ$ — see Table 4 for an indication of how these degenerate solutions differ. Mach number and density profiles are plotted in the top two panels of Figure 7.6. In the bottom panel we plot the corresponding temperature profiles ($T(\chi)/T_o = (\rho(\chi)/\rho_o)^{\gamma-1}$) appropriate for a photoionized disk heated to $\sim 10^4$ K to illustrate the dilemma posed by degenerate solutions: if dust formation is to be taken into account, which of the two profiles are we to believe? The inset plots show a peculiar feature of the solutions lying on the tail of the critical point curves in Figure 7.2, those labelled (1): the temperature (and hence density) undergoes a substantial climb upon rising above the midplane, by as much as 700 K for the $i = 60^\circ$ tail solution. This behavior is not unique to $\gamma = 5/3$ and can be explained

as follows. Since the area made available to the flow upon just rising above the midplane is roughly constant, the continuity equation implies $\dot{m} \approx \rho v$. A decrease in velocity will thus be accompanied by a slight increase in density, in general. The magnitude of this effect is then dependent on the initial velocity. For the $i = 60^\circ$ solutions, v_o is only slightly below c_o for (1), so only a marginal increase in velocity is needed to reach to sonic point. The increase in temperature then acts to prevent the flow from immediately becoming sonic. Similarly, for the $i = 30^\circ$ solutions, (1) actually has the higher initial velocity, but (2) goes sonic first because (2) adiabatically cools, whereas (1) undergoes adiabatic heating for $l \lesssim 0.2 r_o$.

CHAPTER 7

DISCUSSION

As it stands, we have solved and graphically analyzed the Eulerian equations for polytropic winds undergoing Keplerian rotation and traversing the geometry of Figure 4.1. To fully uncover the new aspects of our solutions, we must revisit the spherically symmetric Parker problem, as well as the 'rotating' Parker problem (i.e. a Parker wind following trajectories that conserve specific angular momentum). Analytical considerations of the behavior of Parker winds at higher γ constitute the basis of our discussion.

Recalling Figure 7.1, the critical points lying to the right the vertical dotted lines at $\lambda_o = 2/(\gamma - 1)$ for $\gamma \gtrsim 4/3$ correspond to transonic solutions with initial Mach numbers just slightly below unity. We described these points as originating on a 'tail' of the critical point curves to the left of the vertical line; they correspond to a second transonic solution for the same set of parameters. The lengthening of this tail with increasing γ happens gradually, and the tail points represent the only transonic solutions once they lie to the right of the vertical line.

In this section we account for this behavior, by first showing that critical point solutions to the right of the vertical line have initial velocities exceeding their terminal velocities. We classify solutions with this property as being in the 'enthalpy deficit regime', defined in §7.1. The role of enthalpy will become clear in §7.2, where we examine the simplest class of transonic solutions in the enthalpy deficit regime: those with $3/2 < \gamma < 5/3$ in the spherically symmetric Parker problem. Considerations of this regime with the rotating Parker problem allow us to uncover the origin of the tail points and to explain the presence of minimums in the transonic velocity and Mach number profiles of our disk wind solutions.

This section is geared toward investigators interested in the mathematical properties of Parker winds. Readers more interested in the observational implications of our results are referred to our Conclusions.

7.1 The Enthalpy Deficit Regime

Depending on whether the sum of the enthalpy and the effective potential energy terms at the boundary is positive or negative, we define the flow as having an enthalpy surplus or deficit, respectively. By our dimensionless Bernoulli function, $e_c = y + (\lambda_c/\lambda_o)U_{eff} + h/c_s(\chi_c)^2$, if the sum of the second and third terms is negative at $\chi = 0$, the kinetic energy y must decrease as the sum becomes less negative at $\chi > 0$ to keep e_c constant. Hence, the flow will initially decelerate in the enthalpy deficit regime and we can expect the bulk velocity profile to possess a minimum, in general. The flow can still be transonic because the sound speed (eventually) decreases faster than does the velocity.

Since $h(\chi = 0)/c_s(\chi_c)^2 = s_o/(\gamma - 1)$ and $U_{eff}(\chi = 0) = -\lambda_o + \zeta^2/2$, where $s_o = \lambda_c/\lambda_o$, the defining condition for enthalpy deficit flow places the following requirement on the HEP:

$$\lambda_o > \frac{1}{\gamma - 1} + \frac{\zeta^2}{2}. \tag{7.1}$$

For Keplerian velocities ($\zeta^2 = \lambda_o$), this condition is simply $\lambda_o > 2/(\gamma - 1)$. We see that this regime is encountered only for γ sufficiently larger than 1. From Figure 7.1, the Converging model enters this regime for $\gamma \geq 4/3$, while the CIA model only enters it for $\gamma \approx 5/3$ (see Figure 7.2).

As discussed by Holzer & Axford (1970), transonic winds require a positive Bernoulli constant, i.e. $e_c = B_o/c(\chi_c)^2 > 0$. The Bernoulli function thereby permits an alternative definition of the enthalpy deficit regime, namely $y_o > e_c$. Equivalently, since $v_\infty/v_{esc} =$

$\sqrt{e_c/\lambda_c}$ (see equation (A.3)),

$$v_o > v_\infty. \tag{7.2}$$

In terms of the initial Mach number, this lower bound reads $\mathcal{M}_o > \sqrt{2e_c(\lambda_o/\lambda_c)}$. However, λ_o/λ_c is just the ratio of the temperatures at the critical point and the footprint of the streamline. T_c must certainly be less than T_o for $1 < \gamma < 5/3$ due to adiabatic cooling. Therefore, the bound $\lambda_o/\lambda_c < 1$ implies that $e_c < \mathcal{M}_o^2/2$. Since transonic solutions must by definition obey $\mathcal{M}_o < 1$, yet another condition for enthalpy deficit flow is

$$e_c < \frac{1}{2}. \tag{7.3}$$

The mathematical implication of there being a nonzero lower limit placed on v_o or $\mathcal{M}_o$ naturally leads to the conclusion reached by Parker (1960) that viable solar wind solutions satisfy $1 < \gamma < 3/2$. Only this class of solutions can have vanishingly small initial velocities, criteria that Parker imposed as a boundary condition. For the same reason, the class of $3/2 \leq \gamma < 5/3$ solutions were overlooked in followup treatments, e.g. that of Carovillano & King (1965). Adhering to the physical assumption that the gas is launched from highly subsonic speeds automatically excludes the enthalpy deficit regime.

Even if phenomenologically motivated, diskounting the enthalpy deficit regime prohibits insight into the full nature of the problem. Namely, we benefitted from the realization that Parker winds undergo a regime change because the flow must tap into its own kinetic energy to become transonic.[10] It is informative to view the γ-dependence of the classic Parker problem from an enthalpy standpoint.

[10]In stark contrast, spherically symmetric (Bondi) accretion flow is safely in the enthalpy surplus regime for all γ since both the potential and velocity vanish at the boundary, taken to be infinity.

7.2 The Role of Enthalpy: Spherically Symmetric Parker Winds

In the classic Parker problem, the transonic bulk velocity profile is a monotonically decreasing function of r for $\gamma > 3/2$ (see e.g., Lamers & Cassinelli, 1999). It follows that this class of solutions has $v_o > v_\infty$ and should therefore lie in the enthalpy deficit regime. To show this explicitly, we merely note that the value of the critical point constant, $e_c = (5 - 3\gamma)/2(\gamma - 1)$, combined with the inequality (7.3) yields $\gamma > 3/2$. Furthermore, the inequality (7.1) with $\zeta = 0$ allows us to infer the following allowed HEP ranges (already quoted in Table 1),

$$\begin{aligned} 2 < \lambda_o < \frac{1}{\gamma - 1}, &\quad \text{if } \gamma < \frac{3}{2}; \\ \frac{1}{\gamma - 1} < \lambda_o < 2, &\quad \text{if } \gamma > \frac{3}{2}. \end{aligned} \tag{7.4}$$

The enthalpy deficit regime therefore consists of decelerating transonic solutions confined to a very narrow range of small HEP values.

This much has been emphasized in textbook treatments of the classic Parker problem: $\gamma = 3/2$ is the one value for which all of the enthalpy is used up to lift the gas out of the potential well, with none left over to supply kinetic energy (Lamers & Cassinelli 1999). The complete story is told by the dimensionless Bernoulli function, manipulated to read

$$\frac{\lambda_c}{\lambda_o} = \frac{e_c}{\left[\frac{1}{\gamma - 1} - \lambda_o\right] + \mathcal{M}_o^2/2}. \tag{7.5}$$

We can look upon equation (7.5) as either the temperature ratio T_o/T_c, or as representative of the critical point distance, as $r_c/r_o = \lambda_c/2$. Comparing the bracketed term in the denominator of equation (7.5) with the allowed HEP ranges allows us to infer the behavior of the critical point as γ increases. For transonic flows with a high energy input, meaning that γ is close to 1, there is always a significant excess of enthalpy beyond that used to combat gravity that can contribute to increasing the kinetic energy of the gas. Regardless of

the HEP, $\mathcal{M}_o$ is small because the high energy input permits $v_o << c_o$. The bracketed term is made smallest for large λ_o, i.e., for lower coronal temperatures, so we have the intuitive notion that the smaller the coronal temperature, the more distant the sonic point and the smaller the initial Mach number.

As $\gamma \to 3/2$ from below, progressively smaller HEP are required to compensate for the lower energy input into the wind as it expands. This is shown by curves on the right half of Figure 7.7. There remains a small enthalpy excess, so higher temperatures still lead to higher initial Mach numbers and less distant sonic points. We show representative initial Mach numbers at $r_c/r_o = 3$ and $r_c/r_o = 30$ for $\gamma = 1.48$ to illustrate that $\mathcal{M}_o$ can be almost as small as when γ is much less than 3/2, but only if the sonic point is very far away. (For comparison, for $\gamma = 1.1$, $r_c/r_o = 3$ corresponds to $\lambda_o = 4.145$ and has $\mathcal{M}_o = 0.185$, while $r_c/r_o = 30$ corresponds to $\lambda_o = 8.76$ and has $\mathcal{M}_o = 1.5 \times 10^{-6}$). Realistic solutions that traverse the sonic point within a few r_o therefore require relatively high initial Mach numbers compared to those when γ is small.

For the special case $\gamma = 3/2$, the bulk velocity is a constant at all radii. The inequality 7.2 reveals that the HEP is confined to the single value $\lambda_o = 2$. We show in Appendix D that for this particular value, $v(r) = c_o$, i.e. $\mathcal{M}_o = 1$ and $r_c = r_o$. The flow behavior for the class of accelerating solutions $1 < \gamma < 3/2$ can therefore be summarized as transitioning from an extreme surplus of enthalpy near $\gamma = 1$ that permits $\mathcal{M}_o \approx 0$ at low temperatures, to a scarcity of enthalpy near $\gamma = 3/2$ that requires high temperatures and results in barely accelerating transonic solutions.

We then reach the high temperature regime ($> 4 \times 10^6$ K for solar parameters) of decelerating flow. This class of critical point solutions with $3/2 < \gamma < 5/3$ was found by Dahlberg (1964) using a highly implicit formulation. Parker, responding to this finding,

stated "it would be interesting to work out what conditions the solutions would fit to at the base of the corona where they start" (Parker 1965). Surprisingly, this never appears to have been done!

We duly noted that the high temperature regime is characterized by an enthalpy deficit. As shown by the curves to the left of $\lambda_o = 2$ in Figure 7.7, critical point distances vary oppositely with HEP than for $\gamma < 3/2$; as the temperature decreases for a given γ, so does the sonic point distance, while the initial Mach number increases. These features are easily explained. Loosely speaking, since the flow is slowing down, not speeding up, the gas can become sonic sooner only if the sound speed can quickly drop below the local magnitude of the bulk velocity, a scenario that is expedited if c_o is smaller (λ_o larger) to begin with. More rigorously, the bracketed term in equation (7.5) is negative, so lowering the temperature (increasing λ_o) forces the initial Mach number to be higher, as only a high launching velocity can compensate for the enthalpy deficit. As a secondary effect, the temperature is so high that lowering it somewhat contributes to increasing $\mathcal{M}_o$. Smaller sonic point distances follow. We do note, however, by our representative values of $\mathcal{M}_o$ at $r_c/r_o = 3$ and $r_c/r_o = 30$ for $\gamma = 1.48$, that the initial Mach number in this regime does not greatly exceed $\mathcal{M}_o$ for $\gamma < 3/2$. Indeed, $\mathcal{M}_o$ can be much less than 1, but only for very distant sonic points.

Comparing Figure 7.7 with Figure 7.1 for $\gamma = 1.5$, we see that the sonic points for our disk wind models are not at all symmetric in the neighborhood of the vertical lines, as they are in Figure 7.7 around $\lambda_o = 2$. Moreover, the regime change to enthalpy deficit flow occurs significantly below $\gamma = 3/2$, and its onset is marked by the occurrence of velocity minimums, indicating that the flow is decelerating. Velocity minimums arise by adding angular momentum to the problem.

7.3 The Appearance of Velocity Minimums: Parker Winds with Rotation

We can analytically investigate the effects of including angular momentum by considering the 'rotating Parker problem', in which the streamlines are radial and spherically divergent but rotate rigidly with velocity $u_\phi = \zeta c_o$. Since stars differentially rotate, this solution is valid near the equatorial plane only. In a disk wind context, this solution can be viewed as a wind emanating from the edge of a flared, rigidly rotating disk; the differentially rotating, 'Keplerian Parker wind' solution of §6.1 corresponds to the special case $\zeta = \sqrt{\lambda_o}$. Results for the spherically symmetric Parker problem are recovered by setting $\zeta = 0$.

We begin by finding the relationship between $\hat{r}_c$ and λ_c, where we are calling $\hat{r} = r/r_g = (r/r_o)/\lambda_o$. The effective gravitational force is $g = [1 - (\zeta^2/\lambda_o^2)/\hat{r}]/\hat{r}^2$ (see equation (5.32)), so we have by equation (5.39) that

$$\frac{\lambda_c}{\lambda_o} = \frac{2\hat{r}_c}{1 - (\zeta/\lambda_o)^2/\hat{r}_c}. \tag{7.6}$$

This equation is quadratic in $\hat{r}_c$ with solution,

$$\frac{r_c}{r_o} = \frac{\lambda_c}{4}\left[1 \pm \sqrt{1 - 8\frac{(\zeta/\lambda_o)^2}{\lambda_c/\lambda_o}}\right]. \tag{7.7}$$

Only the positive root is satisfied by the location of the critical point. Is there any meaning to the negative root? In the isothermal ($\lambda_c = \lambda_o$) case, in which the positive root of equation (7.7) directly yields the location of the critical point, the negative root gives the radius where the bulk velocity reaches its minimum value:[11]

$$\frac{r_{min}}{r_o} = \frac{\lambda_o}{4}\left[1 - \sqrt{1 - 8\left(\frac{\zeta}{\lambda_o}\right)^2}\right]. \tag{7.8}$$

[11] We are only concerned with the locations of local minimums, but equation (7.8) yields the location of local maximums also. Indeed, in the limit $\zeta \to 0$, $r_{min} = 0$ is a velocity minimum for $\gamma < 3/2$ and a velocity maximum for $\gamma > 3/2$. Note that purely decelerating flows, which are mathematically equivalent to having bulk velocity minimums at infinity (or maximums at $r_c/r_o < 1$), do not occur for sufficiently high rotation rates.

This occurrence can be accounted for mathematically by recalling the derivation leading up to equation (5.39). As we discussed in §5.5, the critical point must satisfy both the singularity and regularity conditions. The latter defines y' when $y = 1/2$. The former simply picks out all points for which the equation of motion does not depend on the acceleration, a condition that is also satisfied if the acceleration is 0, i.e. at points where the velocity is a local maximum or minimum. In other words, while the location of the critical point must satisfy equation (7.6), there exist rotation rates when $\lambda_c = \lambda_o$ in which points where $y' = 0$, not critical points where $y = 1/2$ (and $y' = 0/0$ by equation (5.33)), also obey this equation.

For the polytropic case, the equation governing the location of bulk velocity minimums has the same form as equation (7.7), but involves $s_{min} \equiv s(\chi = \chi_{min})$:

$$\frac{r_{min}}{r_o} = \frac{\lambda_c}{4 s_{min}} \left[1 \pm \sqrt{1 - 8 \frac{(\zeta/\lambda_o)^2}{\lambda_c/\lambda_o} s_{min}} \right]. \tag{7.9}$$

In general, this location can only be solved for numerically, as s_{min} is a function of both $w(\chi_{min})$ and $A(\chi_{min})$. However, equation (7.8) still approximates this location when $r_{min} \lesssim 2r_o$ if the flow is close to being isothermal, say $\gamma \lesssim 1.1$. In that circumstance, $s_{min} \approx s_o = \lambda_c/\lambda_o$, and the negative root of equation (7.9) reduces to equation (7.8).

Analyzing equation (7.9), velocity minimums will not arise unless $r_{min}/r_o > 1$, implying the bound

$$s_{min} > \frac{\lambda_c}{2} \left(1 - \frac{\zeta^2}{2} \right). \tag{7.10}$$

As it is, this inequality is not very insightful since λ_c is unknown, but since the flow will adiabatically cool, we must also have $s_{min} < s_o = \lambda_c/\lambda_o$. Combining these two inequalities, we can conclude that for a given rotation rate, velocity minimums will not be present unless

$$\lambda_o < 2 + \zeta^2. \tag{7.11}$$

This criteria follows more directly from the equation of motion, as it is the condition for the flow to decelerate off the midplane, i.e. for $y'(\chi = 0) < 0$. Hence, inequality (7.11) is the statement that flows undergoing deceleration must be of very high temperature! It certainly contradicts our intuitive notion that higher temperatures give rise to winds with steeper positive velocity gradients. Evidently, the enthalpy deficit regime must have $\lambda_o < 2 + \zeta^2$, and the appearance of velocity minimums is to the rotating Parker problem what purely decelerating flow is to the spherically symmetric Parker problem. Recall that solutions in the latter problem with $\gamma > 3/2$ still have monotonically increasing Mach number profiles; never does the bulk velocity decrease faster than the sound speed, which would cause $\mathcal{M}$ to decrease. An effect of rotation is to allow this happen, as pointed out by Keppens & Goedbloed (1999). Of course, the locations of Mach number minimums and bulk velocity minimums do not coincide. It will be seen below that Mach number minimums imply accompanying bulk velocity minimums, but the converse is not true.

Notice that for Keplerian rotation ($\zeta^2 = \lambda_o$), the inequality (7.11) is always satisfied, explaining why the bulk velocity profiles of our disk wind solutions possess minimums at all γ. It remains to explain the occurrence of tails on the disk wind critical point curves, which imply that there are two transonic solutions for the same set of parameters. For this, we must carefully study the enthalpy deficit regime of the rotating Parker problem.

7.4 The Enthalpy Deficit Regime with Rotation

The value $2 + \zeta^2$ is the critical HEP below which the bulk velocity must initially decelerate before becoming transonic. Each rotation rate must correspondingly lead to a unique polytropic index, γ_t say, that determines the onset of enthalpy deficit flow. By the inequality

7.1,

$$\gamma_t = 1 + \frac{1}{2 + \zeta^2/2}. \tag{7.12}$$

Necessary (but not sufficient) criteria to reach the enthalpy deficit regime is for *both* $\lambda_o < 2 + \zeta^2$ and $\gamma > \gamma_t$. Sufficient criteria is, by definition, that $\lambda_o > 1/(\gamma - 1) + \zeta^2/2$. The inclusion of rotation lowers γ_t below 3/2, which may seem counterintuitive. Physically, due to the boost from the centrifugal force, winds must be launched with lower temperatures overall. This in turn reduces the enthalpy at the base ($h \propto T$), so a compensatory reduction in γ is required for the enthalpy deficit regime to occur because the magnitude of the effective potential is reduced with rotation.

Another effect of rotation is to smooth the transition from 'normal' critical point behavior, that with r_c/r_o increasing with HEP, to enthalpy deficit behavior. This situation is shown in Figure 7.8, which is the rotational analogue to Figure 7.7. In both figures, $\lambda_o = 2 + \zeta^2$ marks the critical HEP below which r_c/r_o begins to decrease as λ_o increases. An obvious difference is that in Figure 7.8, two wind solutions arise for the same HEP to left of the vertical dotted line, reminiscent of our disk wind results. Despite these tail critical points displaying enthalpy deficit behavior, never do they correspond to transonic solutions with $v_o > v_\infty$ if $\gamma < \gamma_t = 1.4$. Only the (parts of) curves that are bolded have $\lambda_o > 1/(\gamma - 1) + \zeta^2/2$. (The tail of the $\gamma = 1.41$ curve is the first to have points with $\lambda_o > 1/(\gamma - 1) + \zeta^2/2$.) As the fully enthalpy deficit regime is approached, the tail grows in length and the normal critical points begin to disappear altogether.

The HEP bounds reflect these considerations. If $\gamma < \gamma_t$ and there is only one transonic solution per HEP (i.e. if the curve has no tail), then

$$2 + \zeta^2 < \lambda_o < \frac{1}{\gamma - 1} + \frac{\zeta^2}{2}. \tag{7.13}$$

Whenever there are two critical points per HEP, the normal critical points have

$$\lambda_{o,min}(\gamma,\zeta) < \lambda_o < \frac{1}{\gamma-1} + \frac{\zeta^2}{2}. \tag{7.14}$$

The minimum HEP attained, $\lambda_{o,min}(\gamma,\zeta)$, appears to be a priori unknown and is a function of both γ and ζ. The points lying on the tail, meanwhile, have

$$\lambda_{o,min}(\gamma,\zeta) < \lambda_o < 2 + \zeta^2. \tag{7.15}$$

Only once γ is high enough above γ_t such that there is again only one critical point per HEP do we encounter the fully enthalpy deficit regime. In that case, the tail becomes the entire critical point curve and the HEP bound is

$$\frac{1}{\gamma-1} + \frac{\zeta^2}{2} < \lambda_o < 2 + \zeta^2. \tag{7.16}$$

Since γ_t is the polytropic index at which $1/(\gamma-1) + \zeta^2/2 = 2 + \zeta^2$, it marks where the upper bounds switch places.

Another look at the transition from enthalpy surplus to deficit flow given in Figure 7.9. Rather than changing γ for a fixed rotation rate, we set $\gamma = 1.46$ and vary the rotation rate from 0 from to $\zeta = 1.5$. In this way, the enthalpy deficit regime is gradually reached as γ_t drops from 1.5 for $\zeta = 0$ to 1.32 for $\zeta = 1.5$. Notice that the enthalpy surplus critical point curves, the first of which begins at $r_c/r_o \approx 1.02$ for $\zeta = 0$, steadily shift upward to begin and end at higher sonic point distances as the rotation rate is increased. Slightly past $\zeta = 1$, however, the HEP range becomes maximally confined by $\lambda_{o,min}(\gamma,\zeta) < \lambda_o < 2 + \zeta^2$, and only enthalpy deficit roots are allowed. The latter make an appearance on the tail of the $\zeta = 0.6$ curve, the first curve to have $\lambda_o < 2 + \zeta^2 = 2.36$ and $\gamma > \gamma_t = 1.4587$.

Figure 7.9 reveals that, at a fixed energy input (i.e. constant γ) near the enthalpy deficit regime, increasing the rotation rate steadily increases the minimum HEP for which critical

point solutions exist and pushes the lowest sonic point distance to higher values. That is to say, the centrifugal force permits transonic solutions to arise at lower temperatures overall. The flow remains subsonic out to progressively larger radii because a balance must be struck between keeping the flow subsonic at these (still high) temperatures under low effective gravity and simultaneously supplying enough energy to launch a transonic wind when there is little energy injected into the flow at these high γ.

We have selected critical points at $r_c/r_o \approx 11$ in Figure 7.9 to illustrate the effect that rotation has on the Mach number profiles. These critical point solutions have the properties listed in Table **??** and are plotted in Figure 7.10. Curves with higher rotation rates always have larger initial Mach numbers, as expected. Bulk velocity minimums occur whenever the HEP is less than $2 + \zeta^2$, met by solutions (4) and higher, while we see that the Mach number profiles have minimums only for the three solutions in the enthalpy deficit regime, namely (5), (6) and (7). However, having $v_o > v_\infty$ is not a necessary condition for there to be a Mach number minimum, only a sufficient one. Indeed, all critical points on the tail curves exhibit Mach number minimums at the rotation rates that we sampled. At even higher rotation rates, Mach number minimums occur for points on the normal critical point curves. The appearance of Mach number minimums for our disk wind solutions is therefore solely an effect of the high Keplerian rotation rate.

7.5 Summary & Conclusions

We have described in a unified fashion how Parker winds are applicable to modeling the rapid hydrodynamical escape of gas in stars, planets, and accretion disks. Accretion disk winds distinguish themselves in that Parker-like disk winds can result both when (i) the density structure is that of a nearly hydrostatic corona, as with stars and planets

and when (ii) the gas is only slightly inhibited by gravity, residing for example, at radii $r_o > R_{IC}$ for Compton heated coronae. When the HEP lies outside the parameter space of transonic Parker wind solutions, it indicates either that gravity is too strong (and the heating insufficient) to drive a wind or, when the HEP falls below the lower bound, that gravity is unimportant and the gas is free to expand upon being heated. In the latter case, the initial Mach number is 1 according to Parker wind solutions, implying a mass flux density of $\dot{m} = \rho_o c_o$. We showed by way of a simple example that the extrapolation procedure used by GH09 to extend the parameter space of Parker wind solutions is unnecessary. A more conservative and likely more accurate estimate of the global mass loss rate is obtained by simply assuming that $\dot{m} = \rho_o c_o$ in their extrapolated region.

Our main objective was to investigate the dynamical properties of two axially symmetric, thermally driven disk wind models, one with significant adjacent streamline divergence (the Converging model) and another with a complete lack thereof (the CIA model). We made no attempt to construct a 'global' disk wind model by combining the CIA and Converging models in accordance with Figure 4.1. (It would be straight forward, for example, to assign a temperature profile to the disk midplane and calculate the equivalent variation of the HEP as a function of r_o.) Nevertheless, we surveyed the full parameter space of possible transonic wind solutions for both the CIA and the Converging models, so our results embody such a global model.

Since the CIA and Converging models only differ by their respective amounts of streamline divergence, we can attribute the differences in the properties of their solutions as being solely due to geometric effects. Our results have implications for kinematic models that adopt a similar flow geometry for the purposes of computing synthetic spectra to compare with observations. Namely, use of the Converging model will significantly overestimate the

acceleration of the flow if the true wind configuration more closely resembles the CIA model. The latter model features a greatly extended acceleration zone, a more distant sonic surface, and a smaller mass flux density than the Converging model for similar footprint conditions.

We emphasize that detailed hydrodynamical simulations show that by taking into account the interactions of neighboring flow tubes, a self-similar streamline geometry emerges (recall Figure 1.2). We have neglected to mention elsewhere that CIA-like streamlines have also been found analytically from similarity solutions of idealized models for galactic superwinds. Both the self-similar solutions of Bardeen & Berger (1978), which took into account a gravitational potential, and those of Zirakashvili & Völk (2006), which did not involve gravity, are examples. The sonic surface found by Zirakashvili & Völk (2006) bears remarkable resemblance to that obtained in several of the 2.5D simulation runs of Woods et al. (1996) and in the fiducial run of Luketic et al. (2010) (and see also Figure 1 of Font et al. 2004). Namely, the simulations revealed that regions of self similar flow have $z_c \approx 0.25x$ for cylindrical coordinates x and z in units of R_{IC}. The sonic surface of a similarity solution is necessarily a straight line, but that the slope is also about 1/4 in arbitrary units is certainly uncanny (see Figure 1 in Zirakashvili & Völk 2006 and also the discussion in Woods et al. 2006). This connection deserves further attention because the mass loss rate is essentially set by the location of the sonic surface.

We plan to follow up this work with calculations of synthetic line profiles for the geometry of Figure 4.1, to gauge whether adding a CIA-type wind in addition to an inner, Converging wind will significantly alter the line profile characteristics. Kinematic models typically approximate the velocity profile of the flow using a beta-law appropriate for a line-driven stellar wind (CAK), e.g. $v(l) = v_o + (v_\infty - v_o)(1 - r_o/(r_o + l))^\beta$, where β is an ad-hoc parameter controlling the slope of the velocity with distance. The velocity profiles of our

disk wind models are only well-approximated by this monotonic velocity-law beyond $l \approx r_o$. The presence of velocity minimums implies that the flow can undergo significant deceleration for $l < r_o$. We showed this to be an effect of our assumed geometry and will likely not occur if streamlines instead originate from some elevated flow surface above the disk midplane.

On the other hand, our discussion of the spherically symmetric and rotating Parker wind solutions showed that deceleration is associated with a flow regime characterized as having an enthalpy deficit over an appreciable range of the parameter space. It is not inconceivable this type of outflow can be realized in an astrophysical setting, but consider what it would entail: the wind would have to reach a steady state in which the flow is launched with a higher initial velocity than its terminal velocity. A more realistic 1D treatment could shed light on this issue. That would require exploring different effective potentials and flow geometries. We showed that the equivalent nozzle function can be helpful in this regard, as a means to gauge whether or not the flow is monotonic without actually finding the transonic solutions.

Additionaly, solving the time-dependent problem is likely to yield insights into the full domain of viable wind solutions. Especially considering that we found degenerate transonic solutions, uncovering the effects of time-dependence is a worthwhile task, one that we plan to undertake in a future work.

Table 7.1. Properties of the $\gamma = 1.2$, $\lambda_o = 8.0$ transonic solutions plotted in Figure 7.4:

Model, i	l_c/r_o	λ_c	e_c	$\mathcal{M}_o$	v_o/V_{esc}	v_∞/V_{esc}
Con, 30°	11.626	27.194	3.436	0.1464	0.0518	0.5027
Con, 60°	11.303	27.731	3.470	0.0475	0.0168	0.5003
CIA, 30°	33.979	35.910	4.489	0.0079	0.0028	0.5000
CIA, 60°	33.054	35.909	4.489	0.0045	0.0016	0.5000

Table 7.2. Properties of the $i = 30°$ transonic solutions plotted in Figure 7.5:

Model, γ	λ_o	l_c/r_o	λ_c	e_c	$\mathcal{M}_o$	v_o/V_{esc}	v_∞/V_{esc}
Con, 4/3	5.695	10.0128	23.989	1.425	0.6098	0.2555	0.3447
CIA, 4/3	4.304	10.0107	11.992	2.463	0.2678	0.1291	0.6409
CIA, 1.01	11.370	10.0087	11.990	99.463	0.0464	0.0138	4.0731
Con, 1.01	21.710	10.0033	23.970	98.425	0.0044	0.0010	2.8657

Table 7.3. Properties of the degenerate $\gamma = 5/3$ transonic solutions for the CIA model plotted in Figure 7.6:

i, Label	λ_o	l_c/r_o	λ_c	e_c	$\mathcal{M}_o$	v_o/V_{esc}	v_∞/V_{esc}
30°, (1)	2.9	7.7097	9.7132	0.9517	0.6843	0.4018	0.4427
30°, (2)	2.9	44.5443	46.4707	0.9915	0.1541	0.0905	0.2066
60°, (1)	2.3	1.9071	3.3360	1.1330	0.9286	0.6123	0.8242
60°, (2)	2.3	2.9101	4.5759	1.0790	0.6203	0.4090	0.6867

Table 7.4. Properties of the $\gamma = 1.46$ transonic solutions plotted in Figure 7.10:

Label	ζ	γ_t	λ_o	$(\lambda_o)^*_{crit}$	r_c/r_o	λ_c	e_c	$\mathcal{M}_o$	v_o/v_{esc}	v_∞/v_{esc}
(1)	0.	1.5	2.137	2.1739	11.1673	22.3347	0.6739	0.2348	0.1136	0.1737
(2)	0.25	1.4923	2.169	2.2052	10.9180	21.8939	0.6713	0.2463	0.1183	0.1751
(3)	0.5	1.4706	2.268	2.2989	11.1108	22.4442	0.6639	0.2690	0.1263	0.1720
(4)	0.75[†]	1.4384	2.435	2.4551	11.1302	22.7323	0.6527	0.3154	0.1429	0.1694
(5)	1.0	1.4	2.677	2.6739	10.9287	22.6310	0.6385	0.3965	0.1714	0.1680
(6)	1.25	1.3596	3.009	2.9552	11.0326	23.1550	0.6245	0.5196	0.2118	0.1642
(7)	1.5	1.32	3.485	3.2989	11.0584	23.4881	0.6119	0.7441	0.2819	0.1614

* $(\lambda_o)_{crit} = 1/(\gamma - 1) + \zeta^2/2$

[†]For $\lambda_o = 2.435$, there are two wind roots; the second has $r_c/r_o = 6.2391$, $\mathcal{M}_o = 0.4455$, & $\lambda_c = 12.958$

Figure 7.1. Distance to critical (sonic) points from the disk midplane for the CIA and Converging models in units of r_o (that is, $\lambda_o \chi_c = l_c/r_o$) for two inclination angles, $i = 30°$ and $i = 60°$, as a function of the HEP, $\lambda_o = v_{esc}^2/2c_o^2$. Vertical lines mark the value $\lambda_o = 2/(\gamma - 1)$; critical points to the right of this line correspond to transonic solutions with $v_o > v_\infty$. The inset plots display $\mathcal{M}_o$ vs. λ_o and show that the smallest critical point locations have initial Mach numbers approaching unity. The effect of increasing the inclination angle (reducing the centrifugal force) is to allow transonic solutions at smaller HEP.

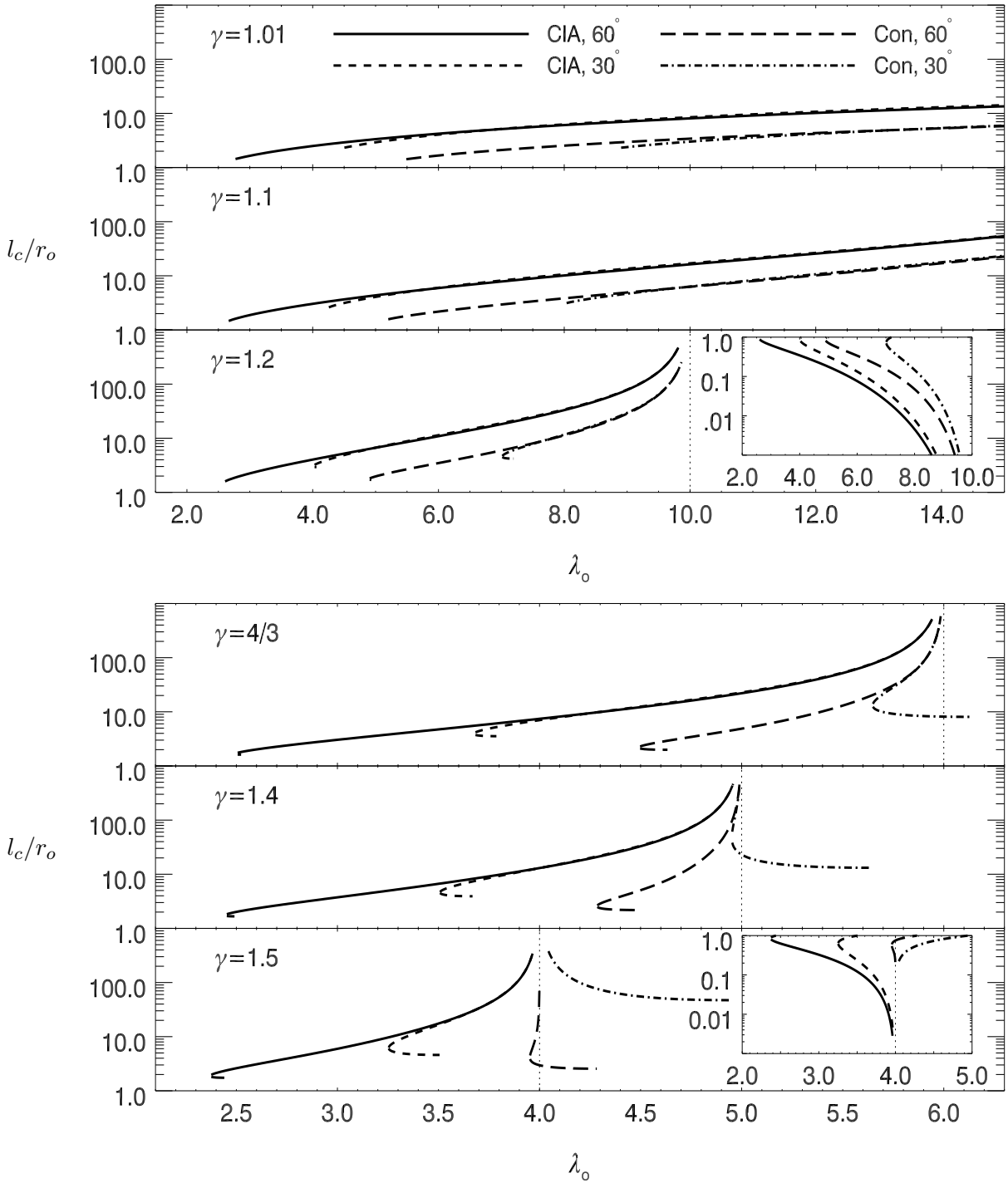

Figure 7.2. Critical point locations (top) and initial Mach numbers (bottom) vs. HEP for $\gamma = 5/3$. See Figure 7.1 for a legend. The Converging model has no solutions for $i = 30°$ (nor does the Parker model with or without rotation). For $i = 60°$, the Converging model has transonic solutions with very high initial Mach numbers and $v_o > v_\infty$ for a small range of HEP around $\lambda_o = 3.9$. Owing to its lack of streamline divergence, the CIA model has solutions for a substantial range of HEP to the left of the vertical line, meaning that these solutions have $v_o < v_\infty$. Compared to a nearly isothermal wind, the distance to the critical point and the initial Mach number are both very sensitive functions of λ_o. Moreover, they are double-valued for the lowest HEP values at a given angle, meaning that two different transonic solutions arise for the same λ_o.

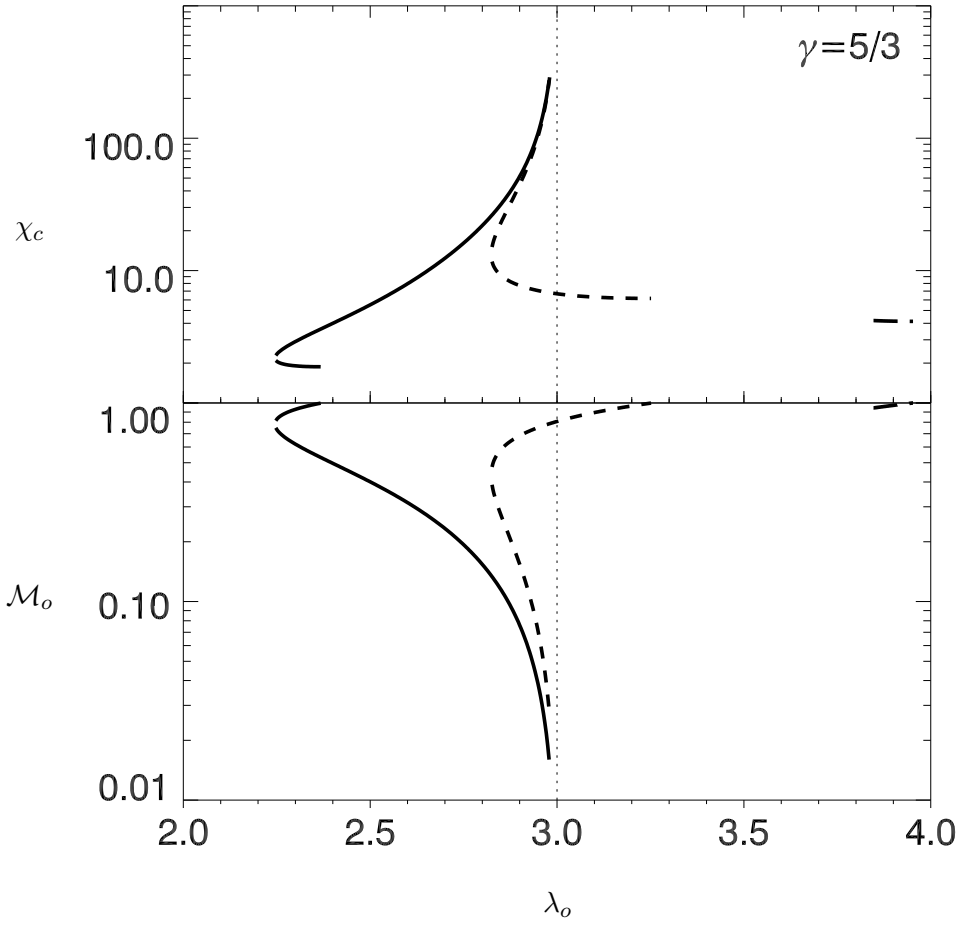

Figure 7.3. The acceleration zone, defined as the distance l/r_o where $v(l) = 0.9\,v_\infty$, of the CIA model (solid) and Converging model (long-dashed) for $i = 60^\circ$ vs. HEP. The vertical scale is the same for each panel and ranges from $1.0\,r_o$ to $10^{10}\,r_o$. The acceleration zone of the CIA model is consistently $2-3$ orders of magnitude greater than that of the Converging model for each γ.

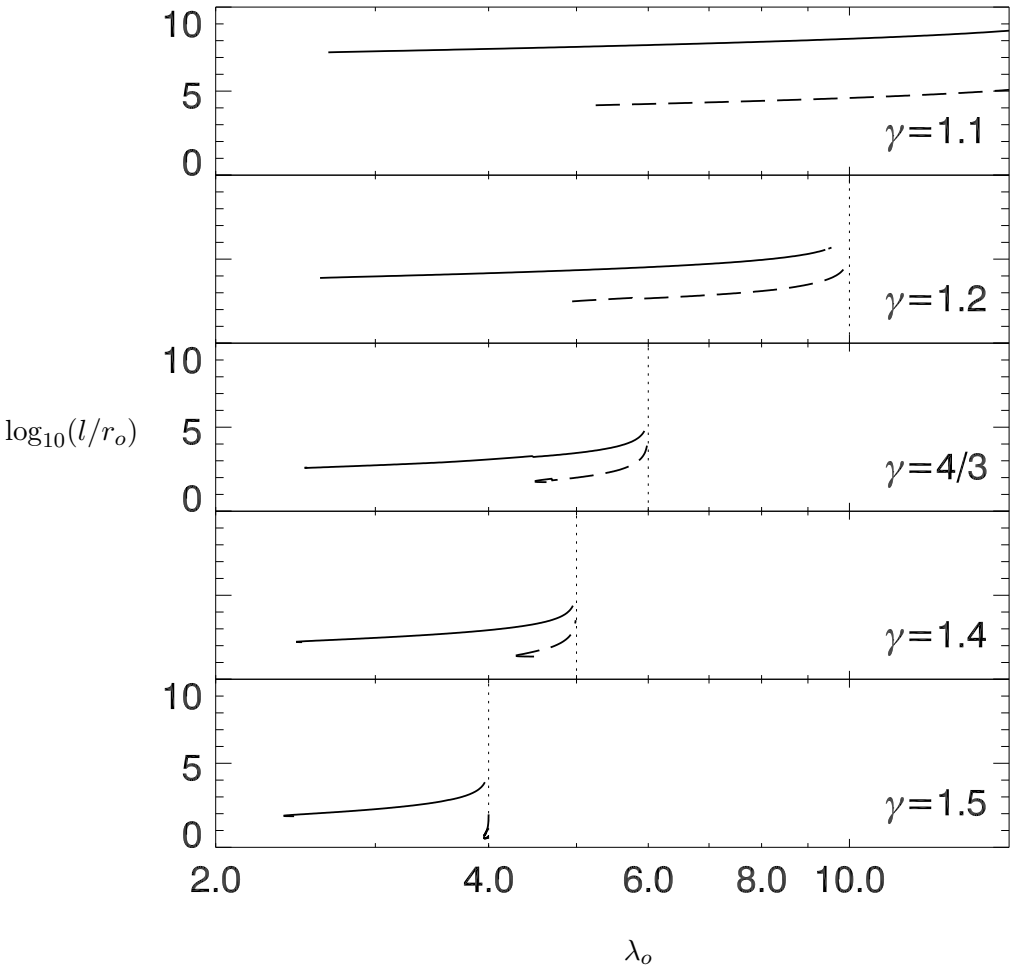

Figure 7.4. Transonic disk wind solutions for the Converging and CIA models for $\gamma = 1.2$ and $\lambda_o = 8$. The top panel is the Mach number as a function of l/r_o, while the middle and bottom panels are the bulk velocity (in units of v_{esc}) and the density (in units of ρ_o) vs. l/r_o, respectively. The dotted lines in the bottom panel are plots of $1/(1 + l/r_o)^q$ to show the asymptotic slopes of CIA model ($q = 1$) and the Converging model ($q = 2$). Properties of these solutions are given in Table 2.

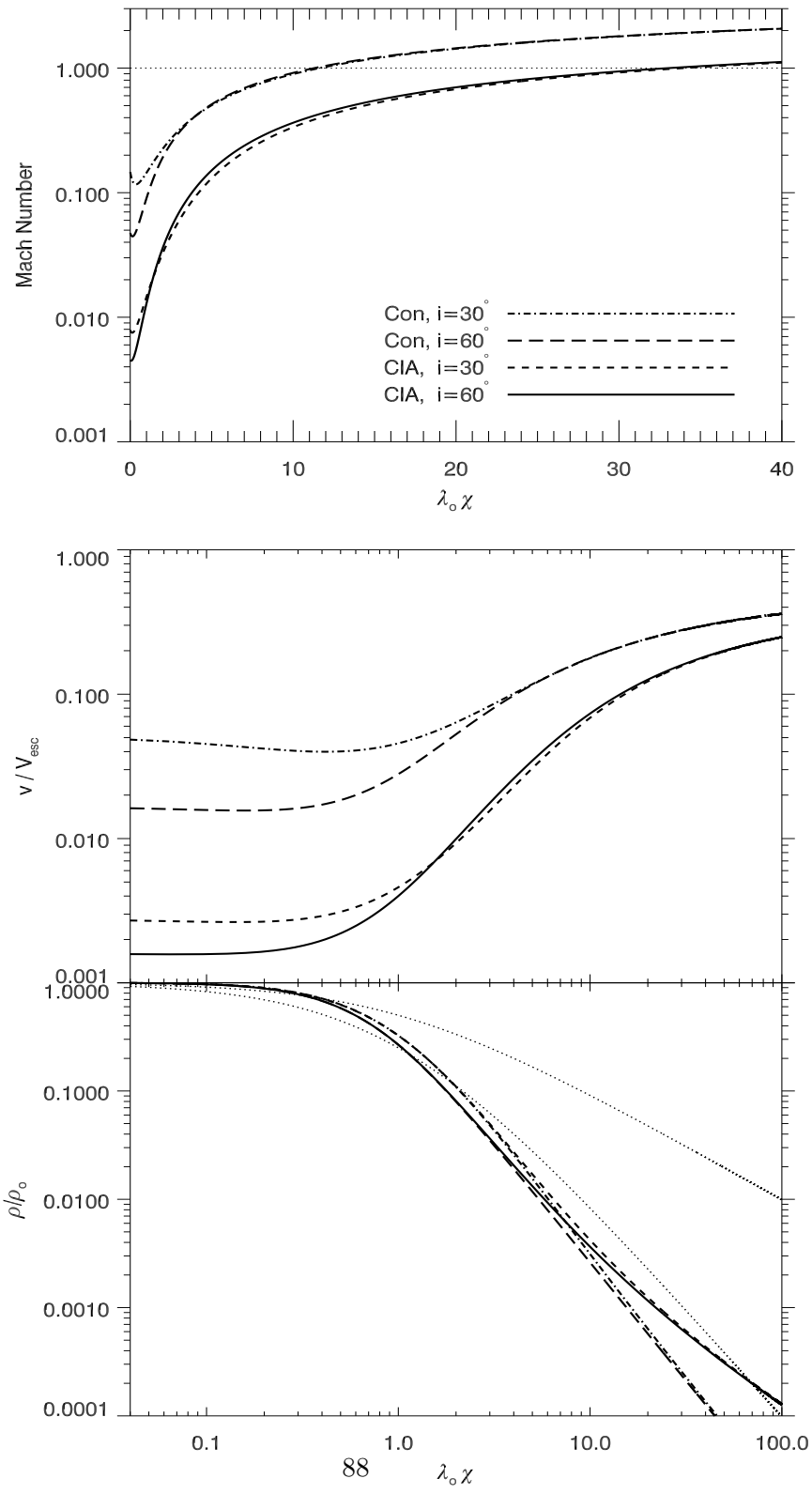

Figure 7.5. Transonic disk wind solutions for the Converging and CIA models for parameters γ, λ_o yielding the same sonic point distance, $l_c/r_o \approx 10$—see Table 3.

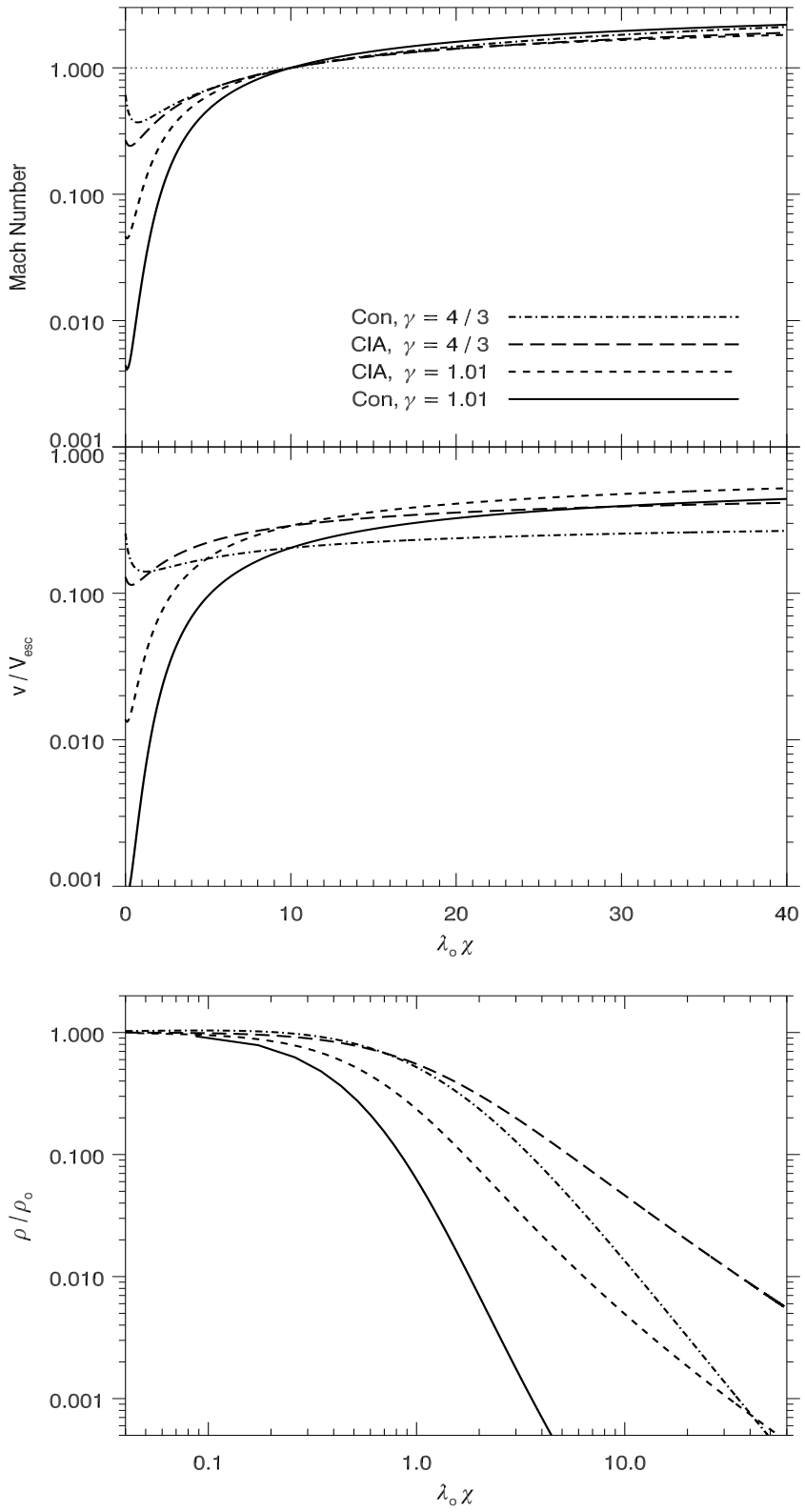

Figure 7.6. Transonic disk wind solutions for the CIA model with $\gamma = 5/3$. Solutions (1) and (2) for either angle have the same set of parameters (γ, λ_o, i); solutions labelled (1) lie on the tail of Figure 7.2. These tail solutions have substantially different properties—see Table 4. The inset plots zoom-in to the region $l_c < r_o$ and show that the density and temperature of the highest velocity solutions actually increase in the region of deceleration (i.e. the gas can be adiabatically compressed).

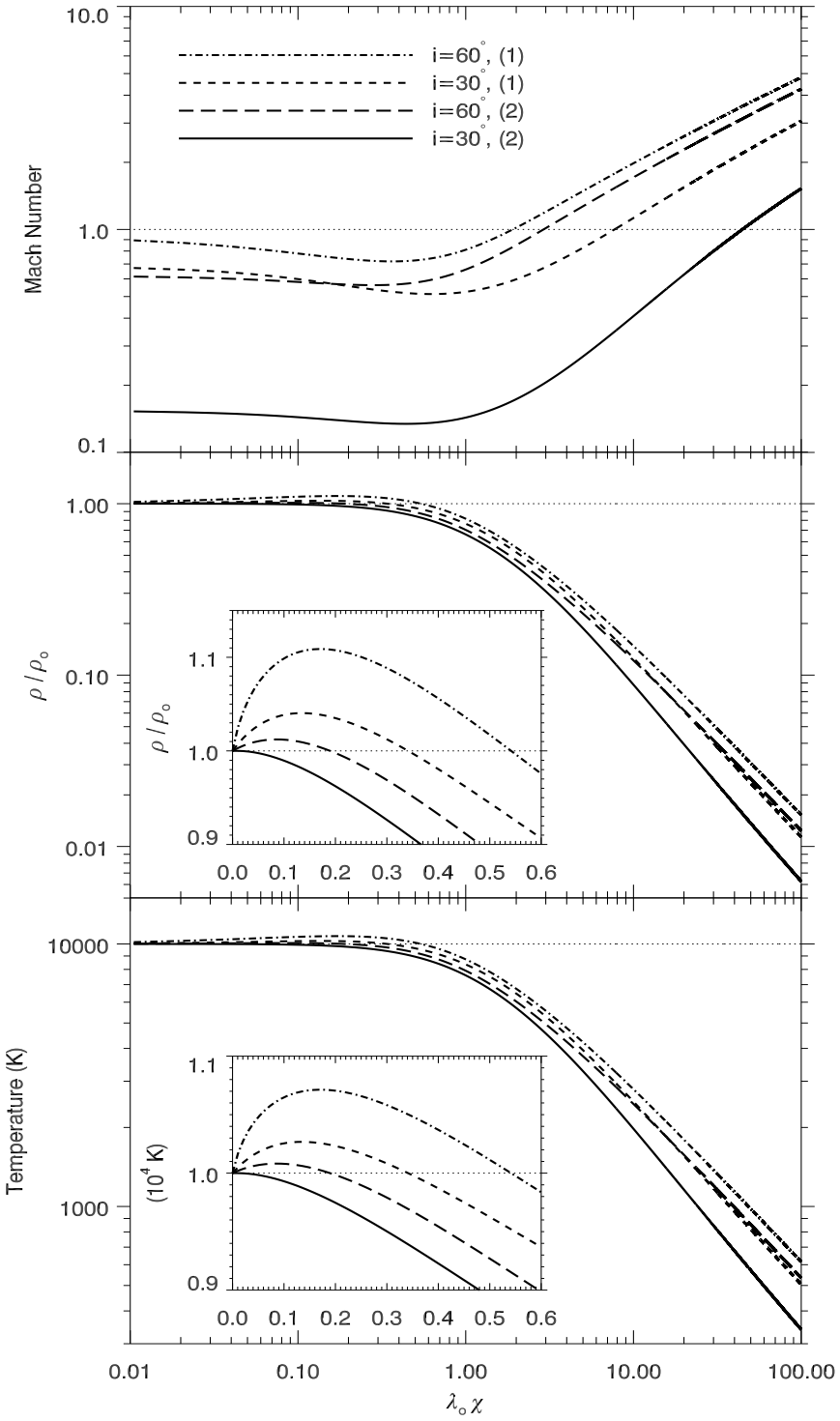

Figure 7.7. Location of critical (sonic) points for the spherically symmetric Parker problem as a function of the HEP in the neighborhood of $\gamma = 3/2$. The vertical, dotted line at $\lambda_o = 2$ separates the enthalpy surplus and enthalpy deficit regimes. Critical points curves in the latter regime (those with $\lambda_o < 2$) have a negative slope (so that higher temperatures lead to more distant sonic points) and correspond to *decelerating* transonic solutions, implying that $v_o > v_\infty$.

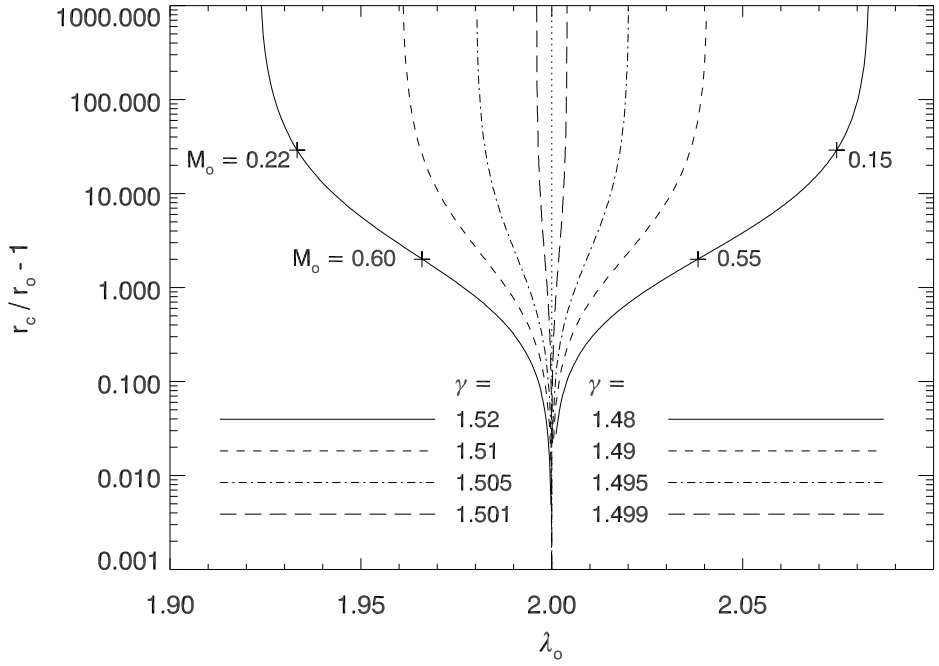

Figure 7.8. Location of critical (sonic) points vs. HEP for the Parker problem with rotation, where the (rigid) rotation rate is $\zeta = 1.0$. This plot is to be compared with Figure 7.7 which has $\gamma_t = 1.5$ and $\zeta = 0$. Here, $\gamma_t = 1.4$ and the enthalpy deficit regime sets in for HEP values to the left of the vertical dotted line at $\lambda_o = 2 + \zeta^2 = 3$, which divides transonic solutions with bulk velocity minimums from those without. Only the bolded sonic points have transonic solutions in the enthalpy deficit regime with $v_o > v_\infty$.

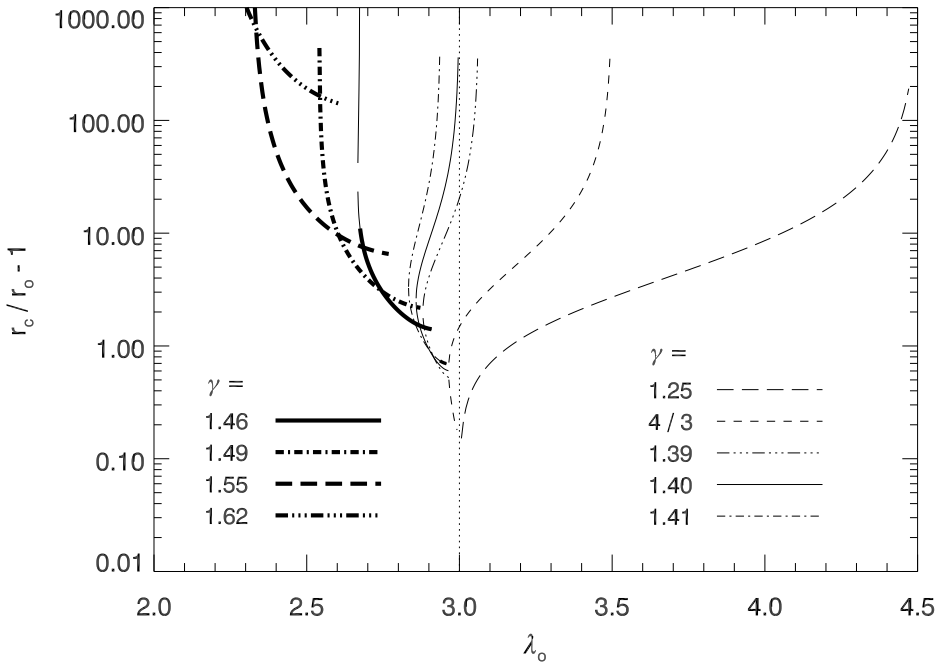

Figure 7.9. Location of critical (sonic) points vs. HEP for $\gamma = 1.46$ for various rotation rates $\zeta = u_\phi/c_o$ ranging from 0 up to 1.5 for the Parker problem with equatorial rotation. The effect of rotation is to shift the enthalpy deficit flow regime to smaller γ, so that this regime (bold curves) is entered by holding γ fixed and increasing ζ. We placed a vertical line at $\lambda_o = 2.36$ to illustrate the tendency toward the upper bound $2 + \zeta^2$. The numbered crosses have the properties tabulated in Table 5 and correspond to the transonic solutions plotted in Figure 7.10.

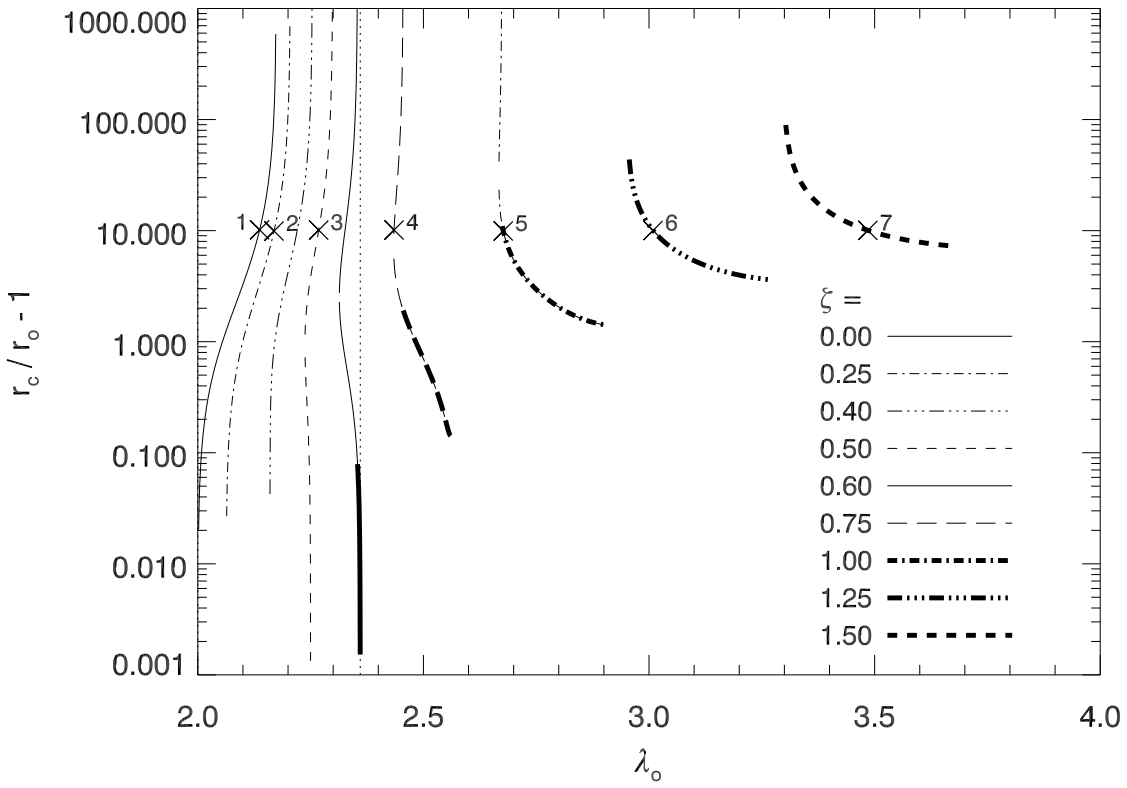

Figure 7.10. Transonic Mach number (top) and bulk velocity (bottom) profiles for the rotating Parker problem with $\gamma = 1.46$. The numbered solutions have the properties listed in Table 5; each solution has a sonic point near $r_c/r_o = 11$. Solutions (5)-(7), bolded, are in the enthalpy deficit regime with $\lambda_o > 1/(\gamma - 1) + \zeta^2/2$ and $v_o > v_\infty$. In contrast to the spherically symmetric Parker problem, bulk velocity profiles are not monotonically decreasing in this regime. The bolded curves also have Mach number minimums, although this is due more to the increased rotation rate, i.e. enthalpy surplus solutions can also display Mach number minimums if $\zeta \gtrsim 1$.

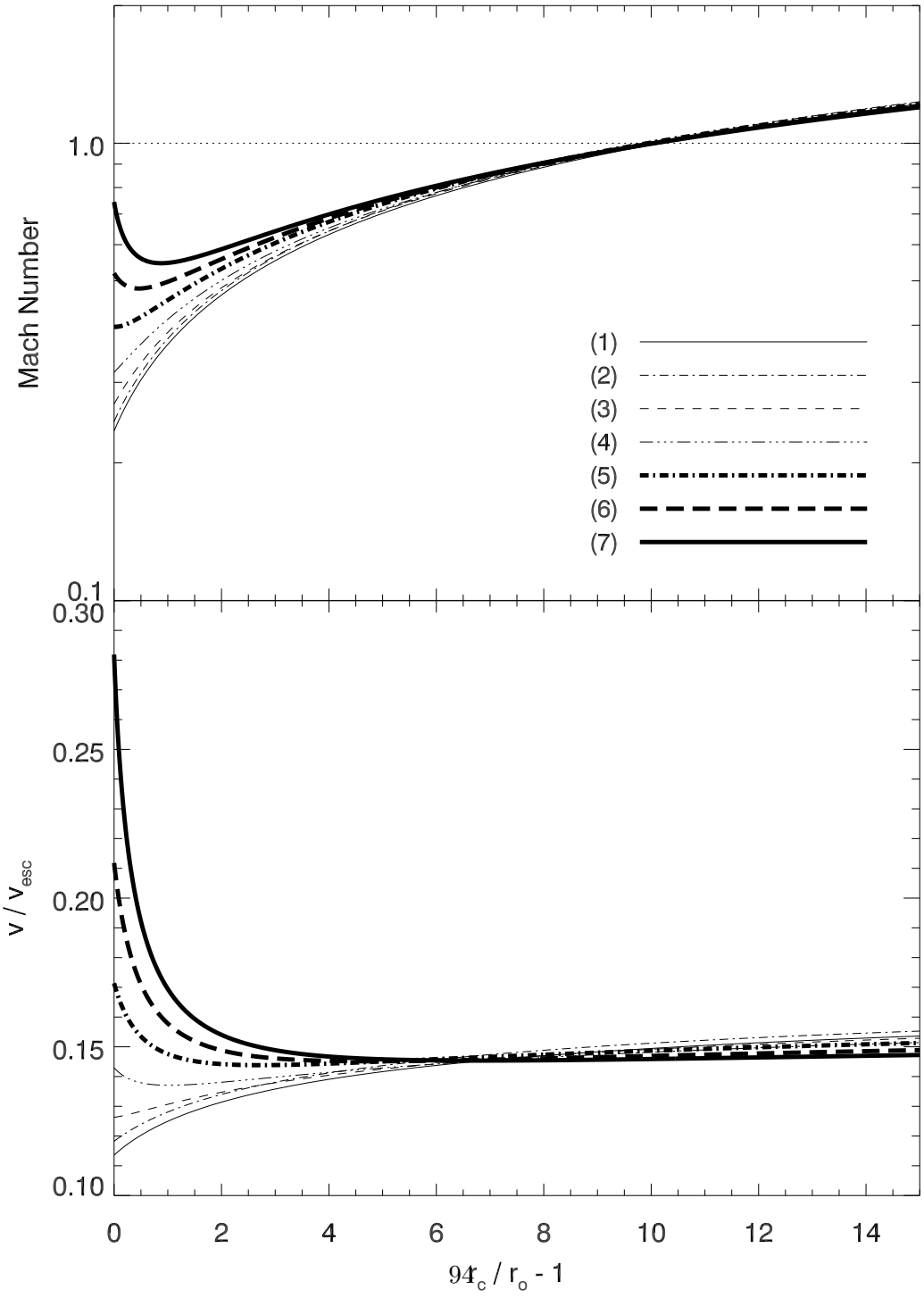

APPENDIX A

FORMULAE FOR THE POLYTROPIC SOLUTION

To facilitate the usage of our solutions for numerical testing purposes, we first sketch the solution procedure. All quantities given in Appendix A follow algebraically from the Mach number, $\mathcal{M} = \sqrt{w}$, which can be determined numerically from the explicit solution, equation (5.45), for $1 < \gamma \leq 5/3$. Since there are multiple values of χ_c satisfying equation (5.42), when solving for w, the rootfinder should separate wind roots, those with $\rho(\chi = 0)/\rho_o = 1$ — according to equation (A.3) — from all other roots (see Appendix D). For every critical point χ_c, there is a unique quantity λ_c given by equation (5.39).

A.1. The Bulk Velocity, Sound Speed, Density, & Internal Energy Profiles

We use as a characteristic velocity, $v_{esc} = \sqrt{2GM_*/r_o}$, in terms of which the HEP is given by $\lambda_o = \mathrm{v}_{esc}^2/2c_o^2$. For disk wind solutions, simply make the substitution $v_{esc} \to \sqrt{2}V_{esc}$, as the appropriate escape velocity for a Keplerian disk is $V_{esc} = \sqrt{GM_*/r_o}$.

The bulk velocity is obtained from the specific kinetic energy $y = \lambda_c(v/v_{esc})^2/2$, which can be found by eliminating s from (5.29) via $y = sw/2$, giving

$$\frac{v}{v_{esc}} = \sqrt{\frac{1}{2\lambda_c}} \left(\Lambda \frac{\mathrm{A}_c}{\mathrm{A}} \right)^{\frac{\gamma-1}{\gamma+1}} \mathcal{M}^{\frac{2}{\gamma+1}}. \tag{A.1}$$

The sound speed is then simply $c_s/v_{esc} = (u/v_{esc})/\mathcal{M}$ by definition, or explicitly from (5.29),

$$\frac{c_s}{v_{esc}} = \sqrt{\frac{1}{2\lambda_c}} \left(\Lambda \frac{\mathrm{A}_c}{\mathrm{A}} \frac{1}{\mathcal{M}} \right)^{\frac{\gamma-1}{\gamma+1}}. \tag{A.2}$$

The above equations reduce to identities in the isothermal $\gamma = 1$ case in which $\lambda_c = \lambda_o$.

The density follows straightforwardly from the polytropic EoS,

$$\frac{\rho}{\rho_o} = \left(\sqrt{2\lambda_o} \frac{c_s}{v_{esc}} \right)^{\frac{2}{\gamma-1}} = \left(\frac{\lambda_o}{\lambda_c} \right)^{\frac{1}{\gamma-1}} \left(\Lambda \frac{\mathrm{A}_c}{\mathrm{A}} \frac{1}{\mathcal{M}} \right)^{\frac{2}{\gamma+1}}, \tag{A.3}$$

where the second equality makes for an interesting comparison with the isothermal result, equation (5.62). Note that $\rho_c/\rho_o = (\lambda_o/\lambda_c)^{1/(\gamma-1)}$. The temperature profile is readily obtained from equation (A.2) but is most simply expressed in terms of the density profile as $T/T_o = (\rho/\rho_o)^{\gamma-1}$.

Finally, the internal energy density E is found from $P = (\gamma-1)E$ combined with $c_s^2 = \gamma P/\rho$:

$$\begin{aligned}\frac{E}{\rho_o v_{esc}^2} &= \frac{1}{\gamma(\gamma-1)}\frac{\rho}{\rho_o}\left(\frac{c_s}{v_{esc}}\right)^2 \\ &= \frac{1}{2\gamma(\gamma-1)}\left(\frac{\lambda_o}{\lambda_c^\gamma}\right)^{\frac{1}{\gamma-1}}\left(\Lambda\frac{\mathrm{A}_c}{\mathrm{A}}\frac{1}{\mathcal{M}}\right)^{\frac{2\gamma}{\gamma+1}}.\end{aligned} \tag{A.4}$$

In terms of the footprint value $E_o \equiv E(\chi = 0)$, the internal energy density is simply

$$\frac{E}{E_o} = \left(\Lambda\frac{\mathrm{A}_o}{\mathrm{A}}\frac{\mathcal{M}_o}{\mathcal{M}}\right)^{\frac{2\gamma}{\gamma+1}}. \tag{A.5}$$

Using equation (A.2), we find that at the critical point, $E_c/E_o = (\lambda_o/\lambda_c)^{\gamma/(\gamma-1)}$.

A.2. The Mass Loss Rate, Initial Velocity, & Terminal Velocity

From equations (5.19) and (5.21) evaluated at the critical point, we find the critical mass flux density

$$\dot{m}_c = \rho_o c_o \frac{\mathrm{A}_c}{A_o}\left(\frac{\lambda_o}{\lambda_c}\right)^{\frac{\gamma+1}{2(\gamma-1)}}. \tag{A.1}$$

Recalling that A_o is a differential flow area, the total mass loss rate is found from $\dot{M} = \int \dot{m} A_o$, where the integral is taken over the wind region on the disk midplane ($A_o = 2\pi r_o dr_o \sin i$) or spherical boundary ($A_o = 2\pi r_o^2 \sin\theta d\theta$). Since $\dot{m} = \rho_o c_o \mathcal{M}_o$, the initial Mach number is $\mathcal{M}_o = (\mathrm{A}_c/\mathrm{A}_o)(\lambda_o/\lambda_c)^{\frac{\gamma+1}{2(\gamma-1)}}$, from which we get the initial velocity in escape speed units ($c_o = v_{esc}/\sqrt{2\lambda_o}$):

$$\frac{v_o}{v_{esc}} = \sqrt{2\lambda_o}\frac{\mathrm{A}_c}{\mathrm{A}_o}\left(\frac{\lambda_o}{\lambda_c}\right)^{\frac{\gamma+1}{2(\gamma-1)}}. \tag{A.2}$$

Equations (A.1) and (A.2) both apply to $\gamma = 1$ when casted in terms of the density using $\rho_c/\rho_o = (\lambda_o/\lambda_c)^{1/(\gamma-1)}$. The terminal velocity is found by evaluating equation (5.22) at infinity, where both the effective potential and pressure (and hence s) vanish, giving

$$\frac{v_\infty}{v_{esc}} = \sqrt{\frac{e_c}{\lambda_c}}. \tag{A.3}$$

APPENDIX B

THE BONDI PROBLEM

It is instructive to apply our dimensionless formulation to the classic Bondi problem, in which the boundary conditions are evaluated at infinity. As mentioned at the beginning of §5.4 , $r_g \to r_B = GM/c_\infty^2$ in that limit. With $\hat{r} = r/r_B$, the potential is simply $U = -1/\hat{r}$ (and so $g = 1/\hat{r}^2$), and the critical point must obey equation (5.39), giving

$$\hat{r}_c = \frac{1}{2}\frac{\lambda_c}{\lambda_o}. \tag{B.1}$$

In light of equation (B.1), the potential at the critical point can be written as $U_c = -2\lambda_o/\lambda_c$. Inserting this into equation (5.35) gives

$$e_c = \frac{1}{2}\left(\frac{5-3\gamma}{\gamma-1}\right). \tag{B.2}$$

Equations (B.1) and (B.2) are the critical point conditions and are the same as those of the classic Parker problem.

Determining an explicit expression for the location of the critical point requires knowing both the critical point constant, e_c, and the Bernoulli constant, B_o. We can then eliminate λ_c/λ_o from equation (B.1) by recalling that $\lambda_c/\lambda_o = e_c/(B_o/c_o^2)$. Equivalently, λ_c/λ_o can be found directly be evaluating the dimensionless Bernoulli function, equation (5.22), at infinity; we require $y_\infty = U_\infty = 0$, and so

$$\frac{\lambda_c}{\lambda_o} = \frac{5-3\gamma}{2}. \tag{B.3}$$

Since $\lambda_c/\lambda_o = c_\infty^2/c_s(r_c)^2$, equation (B.3) gives a pre-determined relationship between the sound speed at the critical point and the sound speed at the boundary, a situation unique to the Bondi problem. It is a consequence of letting $w_\infty = 0$ and is contrary to wind problems in which w_o is nonzero and tied to the location of the critical point. With equation (B.3)

substituted into equation (B.1), we have $\hat{r}_c = (5-3\gamma)/4$, which in physical units is the well known result

$$r_c = \frac{GM}{c_\infty^2}\frac{5-3\gamma}{4}. \tag{B.4}$$

The Bondi accretion rate is recovered from equation (A.1), which in terms of the critical differential mass-loss rate reads

$$\frac{d\dot{M}_c}{\rho_\infty c_\infty} = \mathrm{A}_c \left(\frac{\lambda_o}{\lambda_c}\right)^{\frac{\gamma+1}{2(\gamma-1)}}. \tag{B.5}$$

With $A_c = 2\pi \hat{r}_c^2\, r_B^2 \sin\theta d\theta$, we obtain after substituting in equations (B.1) and (B.3),

$$\frac{d\dot{M}_c}{2\pi r_B^2 \sin\theta d\theta \rho_\infty c_\infty} = \frac{1}{4}\left(\frac{5-3\gamma}{2}\right)^{-\left(\frac{5-3\gamma}{2(\gamma-1)}\right)}. \tag{B.6}$$

For the isothermal ($\gamma = 1$) case, $\hat{r}_c = 1/2$ and so the Bondi rate is given by equation (5.52) as $\Gamma_B = (2\pi r_B^2 \sin\theta d\theta/A_o)e^{3/2}/4$. With $d\dot{M}_c = \rho_o c_o A_o \Gamma_B$, we see that there is no issue with calculating $\dot{M}$ despite $A_o \to \infty$ because there is no actual dependence on the area at the boundary. In other words, we formally have $\Gamma_B = 0$ in the Bondi problem, as it is simply the initial Mach number of the flow (since $d\dot{M}_c = \rho_\infty c_\infty A_\infty \mathcal{M}_\infty$, which is still valid at infinity because the product $A_\infty \mathcal{M}_\infty$ is finite).

The isothermal Mach number profile is, from equation (5.53),

$$\mathcal{M}(\hat{r}) = \sqrt{-W\left[-(\Lambda e^{3/2}/4)^2\left(\frac{\exp[-1/\hat{r}]}{\hat{r}^2}\right)^2\right]}, \tag{B.7}$$

and the corresponding density distribution is

$$\frac{\rho(\hat{r})}{\rho_o} = \frac{\Lambda e^{3/2}/4}{\hat{r}^2 \mathcal{M}(\hat{r})}. \tag{B.8}$$

The X-type solution topology for various values of Λ can readily be explored by plotting equations (B.7) and (B.8).

APPENDIX C

THE CONTINUITY EQUATION

Here we derive the continuity equation appropriate for any axially-symmetric streamline geometry consisting of straight streamlines in the (x, z)-plane. See Fukue (1990) for the appropriate generalization when streamlines possess curvature. In stellar wind equations with spherical symmetry, the continuity equation is usually stated as

$$\dot{M} = 4\pi r^2 \rho(r) v(r). \tag{C.1}$$

The task is to arrive at the appropriate differential area function $A(l)$ that yields the area between streamlines for the disk wind geometry of Figure 4.1. The continuity equation then takes the form

$$d\dot{M} = \rho(l) v(l) A(l). \tag{C.2}$$

We begin with the steady state continuity equation in its coordinate-free, differential form,

$$\boldsymbol{\nabla} \cdot \mathbf{j} = 0, \tag{C.3}$$

where $\mathbf{j} \equiv \rho \mathbf{v}$. Hence by the divergence theorem,

$$\int_V \boldsymbol{\nabla} \cdot \mathbf{j} \, dV = \oint_S \mathbf{j} \cdot \hat{n} \, dS, \tag{C.4}$$

the area occupied by streamlines pointing along $\mathbf{j}$ that cross a surface S with surface normal $\hat{n}$ is equivalently obtained from

$$\oint_S \mathbf{j} \cdot \hat{n} \, dS = 0. \tag{C.5}$$

The spherically symmetric case ($\mathbf{j} \cdot \hat{n} = j(r)$) is easily treated by considering the flow passing through two small solid angles $d\Omega_1$ and $d\Omega_2$ at two different radii $r_2 > r_1$. The surface integral must vanish at both r_1 and r_2 separately, so

$$j(r_1) r_1^2 d\Omega_1 = j(r_2) r_2^2 d\Omega_2. \tag{C.6}$$

Since these radii are arbitrary, each side must equal a constant, $d\dot{M}$, so that at any radius,

$$d\dot{M} = \rho(r)v(r)r^2 d\Omega. \tag{C.7}$$

To capture the entire flow area giving $\dot{M}$, we recover equation (C.1) by integrating over all solid angles at constant r.

Generalizing to the area contained between two wind cones at some height along the z-axis, we now work in cylindrical coordinates in which $\hat{n} = \hat{z}$, $\mathbf{j}(l) \cdot \hat{z} = j(l)\cos(\pi/2 - i) = j(l)\sin i$, and $dS = x dx d\phi$. Evaluating the surface integral in equation (C.5) on a circular slice at some arbitrary height z_1 between two wind cones $x_2 > x_1$ gives

$$d\dot{M} = \int_{l=const} \mathbf{j}(l) \cdot \hat{n}\, dS = j(l)\sin i \left(\pi x^2\right)\Big|_{x_1}^{x_2}. \tag{C.8}$$

From Figure 4.1, we see that the integration limits are from $x_1 = r_o + l\cos i$ to $x_2 = x_1 + dr_o + dr_i$, where the dr_o step sweeps out the increase in area from moving further out along the disk, while dr_i tracks the area swept out from streamline divergence alone. The latter can be related to di by projecting the arc length distance $l\, di$ onto the bold horizontal line:

$$dr_i = -\frac{l di}{\sin i}. \tag{C.9}$$

The negative sign accounts for the decrease in the angle i farther out along the midplane, as we take di to be positive. After some algebra we arrive at

$$A(l) = 2\pi dr_o(r_o + l\cos i)\sin i \left[1 - \frac{l(di/dr_o)}{\sin i}\right]. \tag{C.10}$$

This formula for the differential area traversed by the flow between two straight neighboring streamlines with an arbitrary amount of streamline divergence was obtained by Feldmeier & Shlosman (1999)—see their equation [19].[12]

[12]Note that this is only half the flow area needed to account for a biconical wind and hence to compute the actual mass loss rate.

APPENDIX D

A SECOND CLASS OF ALWAYS PRESENT CRITICAL POINTS

In the spherically symmetric Parker problem, two relationships between the location of the critical point and the initial Mach number can be obtained. The first is equivalent to equation [6] in Keppens & Goedbloed (1999), whose quoted solutions we used to verify our numerical results. It follows from the singularity condition, equation (5.39), taken together with equation (5.41), the combined polytropic/continuity relation. Again calling $\hat{r} = r/r_g$, the effective gravitational force is simply $g = 1/\hat{r}^2$, and $a = \hat{r}^2$, as in the Bondi problem. Subsituting $\lambda_o/\lambda_c = 1/2\hat{r}_c$ into equation (5.41) gives, since $\mathrm{A}_o = f^2 = \lambda_o^{-2}$,

$$\mathcal{M}_o = 2^{-\frac{1}{2}\frac{\gamma+1}{\gamma-1}} \lambda_o^2 \hat{r}_c^{-\frac{5-3\gamma}{2(\gamma-1)}}. \tag{D.1}$$

A second relation between $\hat{r}_c$ and $\mathcal{M}_o$ is found from equation (7.5):

$$\hat{r}_c = \frac{(5-3\gamma)/4}{(\gamma-1)\left[\left(\frac{1}{\gamma-1} - \lambda_o\right) + \mathcal{M}_o^2/2\right]}. \tag{D.2}$$

As a first indication that these equations, when combined, possess multiple critical points, consider the special case $\gamma = 3/2$. Equations (D.1) and (D.2) reveal that

$$\hat{r}_c = \frac{1}{8}\left(\frac{\lambda_o}{2} + 1\right)\left[\left(\frac{\lambda_o}{2}\right)^2 + 1\right]. \tag{D.3}$$

Substituting this back into equation (D.2), we arrive at

$$\mathcal{M}_o = \frac{4(\lambda_o/2)^4}{(\lambda_o/2+1)\left[(\lambda_o/2)^2 + 1\right]}. \tag{D.4}$$

For $\lambda_o = 2$, the only viable HEP value (see Figure 7.7), we immediately see that $\hat{r}_c \equiv r_c/(\lambda_o r_o) = 1/2$, that is, $r_c/r_o = 1$ and $\mathcal{M}_o = 1$. There are thus no transonic wind solutions for $\gamma = 3/2$. Values of $\lambda_o > 2$ do, however, yield the locations of the second class of critical points addressed in this appendix.

The combined equations (D.1) and (D.2), and more generally our critical point equation for disk winds, are numerically seen to *always* possess a second root besides the one leading to a transonic wind solution for all adiabatic indices $1 < \gamma < 5/3$. We do find mention of these roots in the original published account implementing a polytrope (Parker, 1960). Parker's analysis is insightful, using only Descartes' rule of signs, so we reproduce it in our notation. For $\gamma < 3/2$, equations (D.1) and (D.2) can be manipulated to read

$$2\left(\frac{1}{\gamma-1}-\lambda_o\right)\hat{r}_c^{\frac{5-3\gamma}{\gamma-1}} - e_c\hat{r}_c^{\frac{2(3-2\gamma)}{\gamma-1}} + \frac{\lambda_o^4}{2^{\frac{\gamma+1}{\gamma-1}}} = 0. \tag{D.5}$$

From the HEP bound for $\gamma < 3/2$, we see that the first coefficient is always positive and so there are two sign changes, meaning there are always two critical points.[13] For $\gamma > 3/2$, the exponent of the second term in equation (D.5) is negative, so the appropriate equation is now

$$2\left(\frac{1}{\gamma-1}-\lambda_o\right)\hat{r}_c + \frac{\lambda_o^4}{2^{\frac{\gamma+1}{\gamma-1}}}\hat{r}_c^{\frac{2(2\gamma-3)}{\gamma-1}} - e_c = 0. \tag{D.6}$$

In this case, the factor $2(2\gamma-3)/(\gamma-1)$ is never an integer in the range $3/2 < \gamma < 5/3$, so this line of analysis will not work.

As will become clear in the next section, this second class of critical points is required to exist by a mathematical symmetry argument. Because these are genuine critical points, they come complete with an associated family of solutions (depending on the value of Λ), including X-type inflow and outflow transonic solutions. In total, therefore, there are four transonic Mach number profiles, two with $\mathcal{M}_o < 1$ and two with $\mathcal{M}_o > 1$. Only one of the $\mathcal{M}_o < 1$ solutions is a sought after wind solution satisfying $\rho(\chi = 0)/\rho_o = 1$. Hence, it is not enough to simply solve for the transonic Mach number and velocity profiles; the corresponding density profiles must be included to correctly solve the problem.

[13] Of course, Descartes rule only applies to polynomials, so this analysis applies to the infinite number of γ in the range $1 < \gamma < 3/2$ that lead to integer exponents for the two $\hat{r}_c$ terms.

D.1. Properties of the 'Inflow' Solutions

The nature of the second root to the critical point equation is easily accounted for mathematically. The X-type behavior of the solution topology shows that transonic solutions always come in pairs. Referring to the notation of our explicit solution, for every outflow solution with $w << 1$ at small χ extending to $w >> 1$ at large χ, there is an accompanying inflow solution with the opposite behavior. What has been un-emphasized is that the corresponding density profiles do not both satisfy $\rho(\chi = 0)/\rho_o = 1$; only the outflow solution does. Owing to the mathematical equivalence of the wind and accretion equations, why should the density boundary condition preferentially be satisfied by the outflow solution alone? In this view, there must be second critical point such that $\rho(\chi = 0)/\rho_o = 1$ for the curve with $w >> 1$ at $\chi = 0$. The resulting transonic solution has two interpretations, one of them unphysical and the other physically acceptable but very unrealistic. The latter case corresponds to a second outflow solution, in which the flow starts out highly supersonic and reaches a subsonic terminal velocity. The former possibility is that of a transonic *inflow* solution obeying *inner* boundary conditions. This is clearly physically unacceptable because transonic flows are insensitive to conditions downstream of the critical point. The Bondi problem is not to be solved by enforcing a particular density of the flow just outside the central object! Nevertheless, we choose to interpret these points as inflow solutions for the sake of classification and comparison. With that choice, subsonic flow resides at χ *more distant* than the inflow critical point.

To illustrate the behavior of these inflow roots, we limit our attention to the spherically symmetric Parker problem. In Figure D.1 we plot loci of critical points — all the roots, r_c/r_o, of the combined equations (D.1) and (D.2) — vs. HEP for various values of the adiabatic index. Critical points for winds, i.e. those that satisfy $\rho(\chi = 0)/\rho_o = 1$, are

plotted in bold, while the inflow roots are unbolded. Wind solutions can traverse the sonic point very close to the star if the temperature is high enough but must become sonic within $r_c = 400r_o$ or no solutions exist, as evidenced by the termination of the bold lines at $1/(\gamma - 1)$. On the other hand, the inflow lines do not terminate, meaning that the sonic point can reside well past $1000r_o$, as in the Bondi problem, because the flow is subsonic beyond that. A low HEP for inflow solutions is interpreted as establishing a large back pressure which can prevent the flow from becoming sonic until it is very close to the star. The inflow roots tend to the wind roots as $\gamma \to 1$ and degenerate into one root in the strictly isothermal case in which the critical points are all located at $r_c/r_o = \lambda_o/2$. (Our symmetry argument does not apply for $\gamma = 1$ because the logarithmic enthalpy term makes the wind and accretion equations distinguishable and only the solution with $\mathcal{M}_o < 1$ satisfies $\rho(\chi = 0)/\rho_o = 1$.) Finally, notice that there is no regime change around $\gamma = 3/2$ for the inflow roots, and for $\gamma = 3/2$, $\hat{r}_c$ vs. HEP and $\mathcal{M}_o$ vs. HEP are a priori known and given by equations (D.3) and (D.4), respectively.

As a closing comment on this inflow critical point discussion, we note that this second class of critical points will also arise in a generalized Bondi problem (in which the outer boundary is not taken to be infinity and the gas does not start from rest, in order to satisfy the polytropic EoS). There will again be four transonic solutions to choose from, and only one inflow solution will satisfy the outer boundary condition $\rho(\chi = \chi_{outer}) = \rho_o$. This outer boundary condition will also be satisfied by a transonic outflow solution. Analogous to our case above, it seems reasonable to simply reject the outflow solution on the grounds that it is unphysical, as the flow cannot be aware of the conditions upstream of the sonic point. Nevertheless, it would be interesting to investigate the time-dependent problem, as these unphysical solutions may manifest themselves as transient phenomena. They may even be

a further indication that inflow and outflow solutions are intimately coupled in such a way that the starting conditions of an accretion flow can lead to the subsequent onset of a wind (e.g., Blandford & Begelman 1998).

Figure D.1. Location of all critical (sonic) points vs. HEP for the spherically symmetric Parker problem. Bold curves denote the locus of critical points leading to wind solutions, i.e. solutions that satisfy the density boundary condition $\rho(r = r_o) = \rho_o$. Unbolded curves do not satisfy this boundary condition and must be rejected. All plots in the main text display only wind critical points.

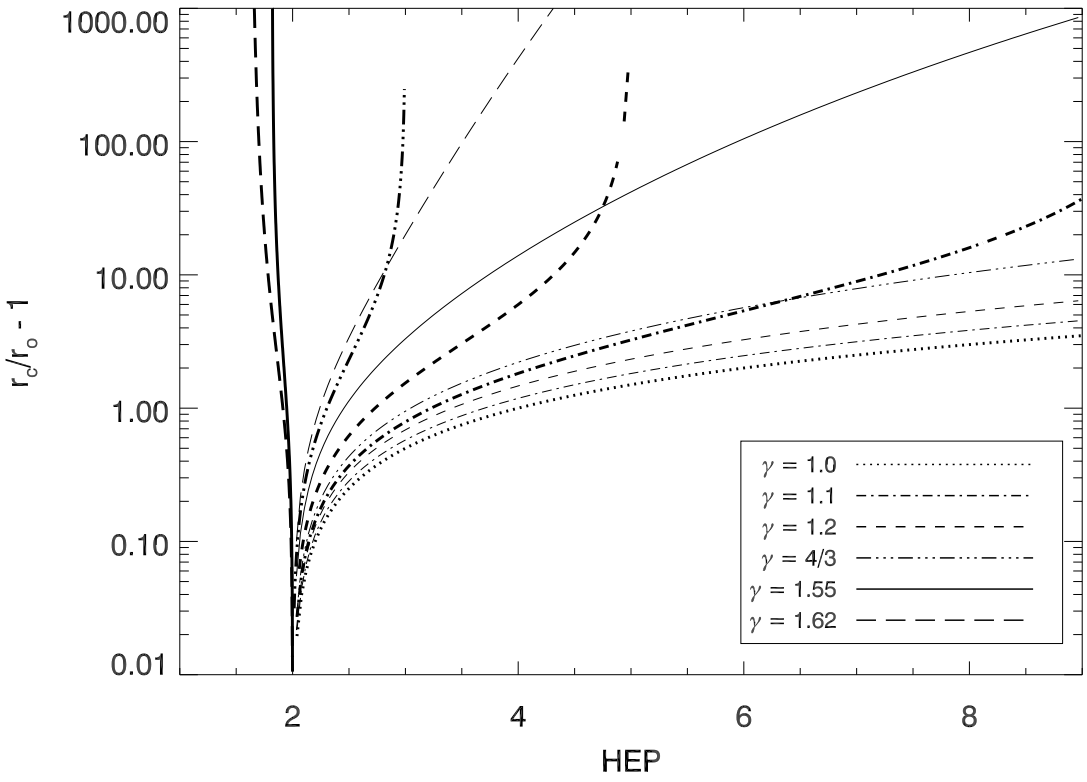

BIBLIOGRAPHY

[1] F. C. Adams, D. Hollenbach, G. Laughlin, and U. Gorti. Photoevaporation of Circumstellar Disks Due to External Far-Ultraviolet Radiation in Stellar Aggregates. , 611:360–379, August 2004.

[2] R. D. Alexander, C. J. Clarke, and J. E. Pringle. Photoevaporation of protoplanetary discs - I. Hydrodynamic models. , 369:216–228, June 2006.

[3] P. J. Armitage. Dynamics of Protoplanetary Disks. , 49:195–236, September 2011.

[4] J. M. Bardeen and B. K. Berger. A model for winds from galactic disks. , 221:105–113, April 1978.

[5] M. C. Begelman, C. F. McKee, and G. A. Shields. Compton heated winds and coronae above accretion disks. I Dynamics. , 271:70–88, August 1983.

[6] D. Biskamp. *Magnetohydrodynamic Turbulence*. September 2003.

[7] R. D. Blandford and M. C. Begelman. On the fate of gas accreting at a low rate on to a black hole. , 303:L1–L5, February 1999.

[8] H. Bondi. On spherically symmetrical accretion. , 112:195, 1952.

[9] J. C. Brandt. *Introduction to the solar wind*. 1970.

[10] R. L. Carovillano and J. H. King. On the Solutions of Parker's Hydrodynamic Theory of Solar and Stellar Winds. , 141:526, February 1965.

[11] J. I. Castor, D. C. Abbott, and R. I. Klein. Radiation-driven winds in Of stars. , 195:157–174, January 1975.

[12] S. K. Chakrabarti. *Theory of transonic astrophysical flows*. 1990.

[13] J. W. Chamberlain. Interplanetary Gas. III. a Hydrodynamic Model of the Corona. , 133:675, March 1961.

[14] J. W. Chamberlain. Planetary coronae and atmospheric evaporation. , 11:901, August 1963.

[15] S. Chapman and H. Zirin. Notes on the Solar Corona and the Terrestrial Ionosphere. *Smithsonian Contributions to Astrophysics*, 2:1, 1957.

[16] O. Cohen, I. V. Sokolov, I. I. Roussev, C. N. Arge, W. B. Manchester, T. I. Gombosi, R. A. Frazin, H. Park, M. D. Butala, F. Kamalabadi, and M. Velli. A Semiempirical Magnetohydrodynamical Model of the Solar Wind. , 654:L163–L166, January 2007.

[17] F. A. Cordova and K. O. Mason. High-velocity winds in close binaries with accretion disks. II - The view along the plane of the disk. , 290:671–682, March 1985.

[18] T. E. Cravens, editor. *Physics of solar system plasmas /Thomas E. Cravens. Cambridge : Cambridge*, 1997.

[19] E. Dahlberg. On the Stellar-Wind Equations. , 140:268, July 1964.

[20] J. Drew and F. Verbunt. Investigation of a wind model for cataclysmic variable ultraviolet resonance line emission. , 213:191–213, March 1985.

[21] J. E. Drew. Inclination and orbital-phase-dependent resonance line-profile calculations applied to cataclysmic variable winds. , 224:595–632, February 1987.

[22] B. Ercolano, C. J. Clarke, and J. J. Drake. X-Ray Irradiated Protoplanetary Disk Atmospheres. II. Predictions from Models in Hydrostatic Equilibrium. , 699:1639–1649, July 2009.

[23] A. Feldmeier and I. Shlosman. Dynamics of Line-driven Winds from Disks in Cataclysmic Variables. I. Solution Topology and Wind Geometry. , 526:344–356, November 1999.

[24] A. S. Font, I. G. McCarthy, D. Johnstone, and D. R. Ballantyne. Photoevaporation of Circumstellar Disks around Young Stars. , 607:890–903, June 2004.

[25] J. Fukue. Hydrodynamical winds from a geometrically thin disk. , 41:123–132, 1989.

[26] J. Fukue and R. Okada. Hydrodynamical winds from an accretion disk. , 42:249–267, April 1990.

[27] A. García Muñoz. Physical and chemical aeronomy of HD 209458b. , 55:1426–1455, July 2007.

[28] U. Gorti and D. Hollenbach. Line Emission from Gas in Optically Thick Dust Disks around Young Stars. , 683:287–303, August 2008.

[29] U. Gorti and D. Hollenbach. Photoevaporation of Circumstellar Disks By Far-Ultraviolet, Extreme-Ultraviolet and X-Ray Radiation from the Central Star. , 690:1539–1552, January 2009.

[30] V. P. Grinin and L. V. Tambovtseva. Disk wind in the radiation of young intermediate-mass stars. *Astronomy Reports*, 55:704–717, August 2011.

[31] S. H. Gross. The atmospheres of Titan and the Galilean satellites. *Journal of Atmospheric Sciences*, 31:1413–1420, July 1974.

[32] D. Hollenbach and F. C. Adams. Dispersal of Disks Around Young Stars: Constraints on Kuiper Belt Formation. In L. Caroff, L. J. Moon, D. Backman, & E. Praton, editor, *Debris Disks and the Formation of Planets*, volume 324 of *Astronomical Society of the Pacific Conference Series*, page 168, December 2004.

[33] D. Hollenbach, D. Johnstone, S. Lizano, and F. Shu. Photoevaporation of disks around massive stars and application to ultracompact H II regions. , 428:654–669, June 1994.

[34] D. J. Hollenbach, H. W. Yorke, and D. Johnstone. Disk Dispersal around Young Stars. *Protostars and Planets IV*, page 401, May 2000.

[35] T. E. Holzer and W. I. Axford. The Theory of Stellar Winds and Related Flows. , 8:31, 1970.

[36] D. M. Hunten. The Escape of Light Gases from Planetary Atmospheres. *Journal of Atmospheric Sciences*, 30:1481–1494, November 1973.

[37] D. M. Hunten. Thermal and nonthermal escape mechanisms for terrestrial bodies. , 30:773–783, August 1982.

[38] D. M. Hunten. Kuiper Prize Lecture - Escape of atmospheres, ancient and modern. , 85:1–20, May 1990.

[39] D. Johnstone, D. Hollenbach, and J. Bally. Photoevaporation of Disks and Clumps by Nearby Massive Stars: Application to Disk Destruction in the Orion Nebula. , 499:758, May 1998.

[40] J. R. Jokipii, C. P. Sonett, and M. S. Giampapa, editors. *Cosmic winds and the heliosphere.*, 1997.

[41] J. F. Kasting and J. B. Pollack. Loss of water from Venus. I - Hydrodynamic escape of hydrogen. , 53:479–508, March 1983.

[42] R. Keppens and J. P. Goedbloed. Numerical simulations of stellar winds: polytropic models. , 343:251–260, March 1999.

[43] C. Knigge, J. A. Woods, and J. E. Drew. The application of Monte Carlo methods to the synthesis of spectral line profiles arising from accretion disc winds. , 273:225–248, March 1995.

[44] A. Königl and R. Salmeron. *The Effects of Large-Scale Magnetic Fields on Disk Formation and Evolution*, pages 283–352. May 2011.

[45] R. P. Kraft. Studies of Stellar Rotation. V. The Dependence of Rotation on Age among Solar-Type Stars. , 150:551, November 1967.

[46] J. H. Krolik, C. F. McKee, and C. B. Tarter. Two-phase models of quasar emission line regions. , 249:422–442, October 1981.

[47] R. Kurosawa, M. M. Romanova, and T. J. Harries. Multidimensional models of hydrogen and helium emission line profiles for classical T Tauri Stars: method, tests and examples. *ArXiv e-prints*, February 2011.

[48] H. J. G. L. M. Lamers and J. P. Cassinelli. *Introduction to Stellar Winds*. June 1999.

[49] E. Leer and T. E. Holzer. Constraints on the solar coronal temperature in regions of open magnetic field. , 63:143–156, August 1979.

[50] S. Luketic, D. Proga, T. R. Kallman, J. C. Raymond, and J. M. Miller. On the Properties of Thermal Disk Winds in X-ray Transient Sources: A Case Study of GRO J1655-40. , 719:515–522, August 2010.

[51] C. W. Mauche and J. C. Raymond. IUE observations of the dwarf nova HL Canis Majoris and the winds of cataclysmic variables. , 323:690–713, December 1987.

[52] B. D. Metzger, T. A. Thompson, and E. Quataert. On the Conditions for Neutron-rich Gamma-Ray Burst Outflows. , 676:1130–1150, April 2008.

[53] R. A. Murray-Clay. *Consequences of planetary migration: Kuiper belt dynamics and atmospheric escape from hot Jupiters*. PhD thesis, University of California, Berkeley, 2008.

[54] U. M. Noebauer, K. S. Long, S. A. Sim, and C. Knigge. The Geometry and Ionization Structure of the Wind in the Eclipsing Nova-like Variables RW Tri and UX UMa. , 719:1932–1945, August 2010.

[55] L. Ofman. Wave Modeling of the Solar Wind. *Living Reviews in Solar Physics*, 7:4, October 2010.

[56] E. C. Ostriker, C. F. McKee, and R. I. Klein. Isothermal, Compton-heated coronae above accretion disks. , 377:593–611, August 1991.

[57] E. N. Parker. Dynamics of the Interplanetary Gas and Magnetic Fields. , 128:664, November 1958.

[58] E. N. Parker. The Hydrodynamic Theory of Solar Corpuscular Radiation and Stellar Winds. , 132:821, November 1960.

[59] E. N. Parker. Dynamical Theory of the Solar Wind. , 4:666–708, September 1965.

[60] W. H. Press, S. A. Teukolsky, W. T. Vetterling, and B. P. Flannery. *Numerical recipes in C. The art of scientific computing*. 1992.

[61] D. Proga. Theory of Winds in AGNs. In L. C. Ho & J.-W. Wang, editor, *The Central Engine of Active Galactic Nuclei*, volume 373 of *Astronomical Society of the Pacific Conference Series*, page 267, October 2007.

[62] D. Proga and T. R. Kallman. On the Role of the Ultraviolet and X-Ray Radiation in Driving a Disk Wind in X-Ray Binaries. , 565:455–470, January 2002.

[63] I. I. Roussev, T. I. Gombosi, I. V. Sokolov, M. Velli, W. Manchester, IV, D. L. DeZeeuw, P. Liewer, G. Tóth, and J. Luhmann. A Three-dimensional Model of the Solar Wind Incorporating Solar Magnetogram Observations. , 595:L57–L61, September 2003.

[64] S. Seager. *Exoplanets*. 2010.

[65] I. Shlosman and P. Vitello. Winds from accretion disks - Ultraviolet line formation in cataclysmic variables. , 409:372–386, May 1993.

[66] F. H. Shu, D. Johnstone, and D. Hollenbach. Photoevaporation of the solar nebula and the formation of the giant planets. , 106:92, November 1993.

[67] S. A. Sim, J. E. Drew, and K. S. Long. Two-dimensional Monte Carlo simulations of HI line formation in massive young stellar object disc winds. , 363:615–627, October 2005.

[68] S. A. Sim, K. S. Long, L. Miller, and T. J. Turner. Multidimensional modelling of X-ray spectra for AGN accretion disc outflows. , 388:611–624, August 2008.

[69] M. A. Skinner and E. C. Ostriker. The Athena Astrophysical Magnetohydrodynamics Code in Cylindrical Geometry. , 188:290–311, May 2010.

[70] J. M. Stone and D. Proga. Anisotropic Winds from Close-In Extrasolar Planets. , 694:205–213, March 2009.

[71] F. Takahara, R. Rosner, and M. Kusunose. Winds from hot accretion disks. , 346:122–125, November 1989.

[72] F. Tian, O. B. Toon, A. A. Pavlov, and H. De Sterck. Transonic Hydrodynamic Escape of Hydrogen from Extrasolar Planetary Atmospheres. , 621:1049–1060, March 2005.

[73] K. Tsinganos. The acceleration of the nonspherically symmetric solar wind and the solar probe. *Advances in Space Research*, 17:65–74, 1996.

[74] S. R. Valluri, D. J. Jeffrey, and R. M. Corless. Tutorial/Article didactique: Some applications of the Lambert W function to physics. *Canadian Journal of Physics*, 78:823, September 2000.

[75] A. J. Watson, T. M. Donahue, and J. C. G. Walker. The dynamics of a rapidly escaping atmosphere - Applications to the evolution of earth and Venus. , 48:150–166, November 1981.

[76] E. J. Weber and L. Davis, Jr. The Angular Momentum of the Solar Wind. , 148:217–227, April 1967.

[77] D. T. Woods, R. I. Klein, J. I. Castor, C. F. McKee, and J. B. Bell. X-Ray–heated Coronae and Winds from Accretion Disks: Time-dependent Two-dimensional Hydrodynamics with Adaptive Mesh Refinement. , 461:767, April 1996.

[78] R. V. Yelle. Aeronomy of extra-solar giant planets at small orbital distances. , 170:167–179, July 2004.

[79] V. N. Zirakashvili and H. J. Völk. Simple Model of the Outflow from Starburst Galaxies: Application to Radio Observations. , 636:140–148, January 2006.

VITA

Graduate College
University of Nevada, Las Vegas

Timothy R. Waters

Degrees:

Bachelor of Arts, May 2006
Occidental College

Master of Science in Applied Mathematics, May 2009
University of Nevada Las Vegas

Thesis Title:

Parker Winds Revisited: An Extension to Disk Winds

Thesis Examination Committee:

Chairperson, Daniel Proga, Ph.D.
Committee Member, Bing Zhang, Ph.D.
Committee Member, Steven Lepp, Ph.D.
Graduate Faculty Representative, Balakrishnan Naduvalath, Ph.D.

Honors & Awards:

Nevada NASA Space Grant Consortium Fellowship, Spring - Fall 2011
UNLV Travel Grant to attend an international conference, Spring 2011
Secretary/Treasurer, Southern Nevada AAPT Section, Spring 2011-Present
2010 NASA Student Ambassador
Inducted to Sigma Pi Sigma Physics Honor Society, Spring 2006
W.M. Keck Foundation Endowed Scholarship, Spring 2006
Faculty Search Committee Student Member, Occidental Physics Dept, 2005
President's Scholarship, Occidental College, Fall 2002 - Spring 2006

Publications:

Waters & Proga 2012, Parker Winds Revisited: An Extension to Disc Winds, (Submitted to MNRAS)